UNIVERSITÀ DEGLI STUDI DI CATANIA

DIPARTIMENTO DI FISICA E ASTRONOMIA

NATIONAL PhD IN NUCLEAR PHYSICS

GABRIELE GAETANO TARANTO

SELECTING MICROSCOPIC EQUATIONS OF STATE OF NUCLEAR
MATTER FOR THE STUDY OF NEUTRON STARS

PH.D. THESIS

PH.D. COORDINATOR:
CHIAR.MO PROF. F. RIGGI

TUTORS:
CHIAR.MI PROF. G.F. BURGIO
PROF. V. GRECO

CICLO XXVIII 2012/2015

Contents

Contents

"Amare è desiderare profondamente il proprio desiderio"
"Nella vita tutto fa rima" , *Gabriele Taranto*

"To love is to desire deeply our own desire"
"Everything in life rhymes" , *Gabriele Taranto*

To my Family and Valentina....

Abstract

I developed my PhD thesis in the aerea of astronuclear theory, an inter-disciplinary field where many aspects of nuclear physics, particle physics and astrophysics converge. The research carried out is the study of the equation of state of nuclear matter and its implications for the structure of neutron stars. Neutron stars are compact objects produced in the gravitational collapse of very massive stars just after they explode as supernova, and are characterized by central density extremely high, up to one order of magnitude greater than the nuclear saturation density ($10^{14} gr/cm^3$). Therefore the knowledge of the equation of state (EoS) of nuclear matter at high density is critical for the understanding of stellar structure.

During these 3 years, I derived an equation of state for nuclear matter using the many-body microscopic theory by Brueckner-Bethe-Goldstone. The term "microscopic" comes from the fact that the only ingredient required as "input" is the nucleon-nucleon interaction, which in the case of nucleons is known from scattering experiments. The in-clusion of nucleonic three-body forces turns out crucial, so that the EoS not only gives the correct values of density and binding energies at the saturation point, but also the correct compressibility and symme-try energy, which all turn out to be compatible with values extracted from phenomenology. The theoretical approach is widely discussed in the Chapter 3. I have systematically explored the different nucleon-

nucleon interactions and three body forces (both phenomenological and microscopic ones). With the EoS obtained, I solved the equations of hydrostatic equilibrium of the star, known as Tolman - Oppenheimer - Volkoff equations, and I calculated the stellar configurations for the equilibrium for several EoSs. The calculated maximum masses of neutron stars are equal approximately to 2 solar masses, and radii ranging from 12 to 14 km, according to the observational data recently obtained from satellites in X-ray and Gamma of new generation (Chandra, XMM Newton and Integral). The obtained results were published in a Physical Review C [1] and in a proceeding [6]. The results are shown in Chapter 4.

This work has been further extended to the calculation of the effective masses of nucleons, always within the Brueckner theory. This calculation is crucial for the study of neutron star cooling, where one of the main ingredients is the neutrino emissivity, which depends largely on the effective masses of nucleons. I have systematically explored the effective masses with different two- and three-body interactions, and several values of matter asymmetry. This work was published in Phys. Rev, C [2]. Afterwards, the effective masses obtained from the calculation were included in the cooling codes, which are publicly available, along with the stellar cooling gaps of superfluidity, calculated in the same theoretical approach. The results obtained have shown for the first time the important role of the Urca processes in stellar cooling, giving rise to a high flux of neutrinos, and superfluidity in channels 1S0 and 3PF2 of proton and neutron respectively. It is thus explained the cooling of Cassiopeia A, a supernova remnant whose thermal emission has been monitored for many years, and the analysis of which is compatible with the idea that the stellar core is in a superfluid state. The work was published in Monthly Notices of the Royal Astronomical Society (MNRAS) [4] and is discussed in Chapter 5.

During my PhD second year, I started a collaboration with Prof. M. Alford (University of Saint Louis, Missouri, USA) about the transition to quark matter inside neutron stars. In fact, as neutron stars are characterized by values of central density up to about 8-10 times the saturation value, in stellar core the transition from the hadronic confined phase, to a deconfined quark phase could take place, giving rise to the so-called hybrid stars. The correct determination of the mass and radius for the same neutron star could give access to the equation of state for the quark matter, since the mass - radius relationship in this case is different from the one of ordinary stars. Since it is not possible to perform lattice QCD calculations at zero temperature and finite density, various models are used for describing quark matter. I focused on the FCM (Field Correlator Method) model and I applied it to the stellar matter by analyzing the dependence on the parameters, and establishing the limits using an EoS parametrized for quark matter and proposed recently by M. Alford. The work was recently published in Phys. Rev. D [3] and results are shown in Chapter 6.

Finally in Chapter 7 I draw the conclusions and the outlooks.

List of Papers

[1] G. Taranto, M. Baldo, and G. F. Burgio, Selecting microscopic equations of state, Phys. Rev. C 87, 045803 (2013).

[2] M. Baldo, G. F. Burgio, H., J. Schulze, and G. Taranto, Nucleon effective masses within the Brueckner-Hartree-Fock theory: Impact on stellar neutrino emission, Phys. Rev. C 89, 048801 (2014).

[3] M. G. Alford, G. F. Burgio, S. Han, G. Taranto and D. Zappala', Constraining and applying a generic high-density equation of state, Phys. Rev. D 92, 083002 (2015).

[4] G. Taranto, G. F. Burgio, and H.J. Schulze, Cassiopeia A and direct Urca cooling, in press in Monthly Notices of the Royal Astronomical Society, ARXIV:1511.04243

[5] G. F. Burgio, H. Chen, H.J. Schulze, and G. Taranto, Constraints on the quark matter equation of state from astrophysical observations, PoS Confinement X (2013) 255.

[6] G. Taranto, M. Baldo, and G. F. Burgio, Constraints on modern microscopic equations of state, to be published on Journal of Physics : Conference Series, October 2015.

Chapter 1

Introduction

Contents

1.1   Neutron Stars

The first one to talk about this kind of object was Lev Landau in March 1931 [1]. Landau improvised the concept of 'unheimliche sterne' namely "weird stars" discussing with Bohr and Rosenfeld about his paper written in Zurich in February 1931 but not published until February 1932 namely just after the discovery of the neutron by Chadwick. In his paper [2] Landau mentioned the possible existence of dense stars which look like one giant nucleus; this can be regarded as an early theoretical prediction or anticipation of neutron stars, prior to the discovery of the neutron!

Nowadays, we know that neutron stars are extremely compact stellar objects produced in the cores of massive stars that at the end of their evolution as supernovae explode and collapse gravitationally. The birth of these stars by supernova explosions was first suggested by Baade and Zwicky in 1934. The first theoretical calculation [3] was performed by Tolman, Oppenheimer and Volkoff in 1939 and Wheeler in 1966. These strange objects can be considered the heaviest of heavy ions, with $A \approx 10^{57}$ baryons; the matter contained is the most dense of the universe, with an average density which is comparable to the density of nuclear matter which is $\rho_0 \approx 0.17 \; baryons/fm^3 \approx 2.8 \cdot 10^{14} g/cm^3$. Therefore, the determination of the equation of state for dense matter is essential for calculating the properties of neutron stars. The EoS determines the properties such as the range of masses, the relationship mass-radius, the thickness of the crust, the period of rotation, the cooling rate and much more. The same EoS is also crucial in the calculation of the energy released during the explosion of a supernova.

Neutron stars are associated with two classes of astrophysical galactic objects. The first class, pulsars, are generally considered to be rotating neutron stars. Bell and Hewish were the first to discover a neutron

Figure 1.1: Jocelyn Bell at the time of the discovery.

star in 1967 as a radio pulsar. They nicknamed the signal $LGM - 1$ for "Little Green Men" (a playful name for intelligent beings of extraterrestrial origin) because of the extreme regularity of the pulse. For this discovery only Hewish (who was the advisor of J. Bell) was awarded with the Nobel Prize and for this decision there were some protests in the scientific community. Someone ironically said that she received the "No-Bell" prize [4].

The first radio binary pulsar, $PSR\,1913 + 16$, was discovered by Hulse and Taylor in 1975. Measuring the spiral, they were able to determine all the parameters such as the masses, orbital periods and periods derivatives, orbital distance and inclination. The total number of pulsars discovered exceeds the thousands and the number is growing.

The second class of astrophysical objects associated with neutron

stars are the compact sources of $X - rays$, some of which are neutron stars in binary orbits closed with ordinary stars. With the X-ray detectors on board of satellites since 1971 they have found more than 200 X-ray pulsars and for about 60 the orbital period was determined. The X-ray pulsars are believed to be neutron stars accreting by the respective companions. Measures of masses and radii of neutron stars can be a unique window to the behavior of matter at densities that can be found in atomic nuclei. Regarding the mass, in Fig. 1.2 we show the current systematic for the measured neutron star masses obtained for binary systems, where the the largest ones are 1.97 ± 0.01 [5] and 2.01 ± 0.01 [6]. From that we can deduce that soft EoSs must be excluded by data observation.
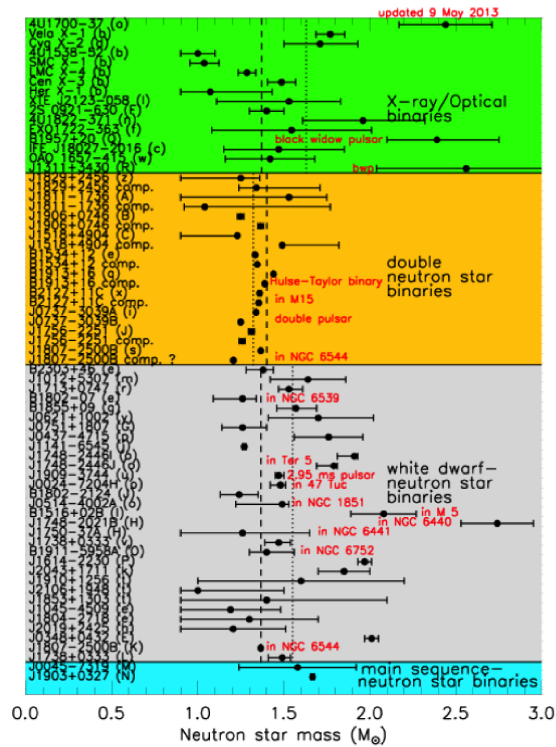

Figure 1.2: Systematic for the masses. Courtesy by J. Lattimer.
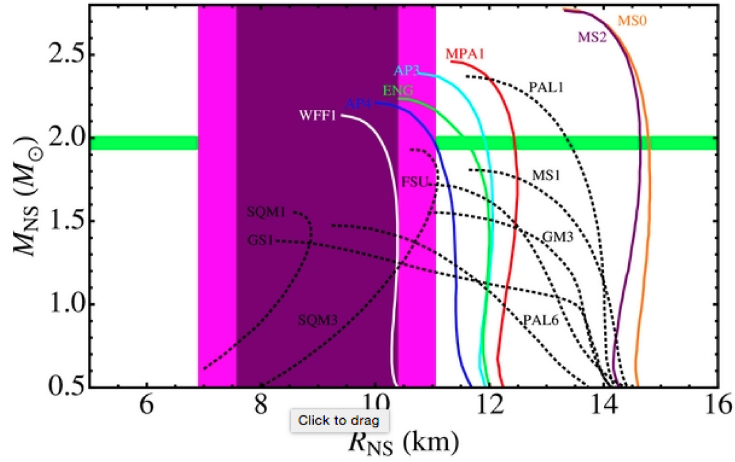
Figure 1.3: Figure showing the constraint on the EoS imposed by the radius measurement obtained in [7]. The dark and light shaded areas show the 90%−confidence and 99%−confidence constraints of the radius neutron star measurement, respectively. The mass measurement of PSR J1614-2230 is shown as the horizontal band (Demorest et al. 2010). "Normal matter" EoSs are the colored solid lines. Other types of EoSs, such as the hybrid or quark-matter EoSs are include for comparison with dashed lines.

As far as the radii are concerning, the measurement of 10 Km at a distance of at least $10^{15} Km$ is a daunting experimental problem. Therefore direct measurements of radii for neutron stars do not exist. However the observational data combined with special theoretical assumptions give some information. The authors of [7] claim that recent observations of NSs have shown evidence that cold ultra dense matter—present in the core of neutron stars—is best described by "normal matter" equations of state (EoSs). Such EoSs predict that the radii of NSs, R_{NS}, are quasi-constant (within measurement errors, of $\approx 10\%$) for astrophysically relevant masses ($M_{NS} > 0.5 M_\odot$). In [7] this theoretical prediction is adopted as an assumption, and one constrains a single R_{NS} value from five quiescent low-mass X-ray binaries ($qLMXB$) targets with available high signal-to-noise X-ray spectro-

scopic data. In Fig. 1.3 are presented the results that are in agreement with a $R_{NS} = 9.1^{+1.3}_{-1.5} Km$ (90 % of confidence).

In this sense the investigation of the neutron star radius is essential for constraining the EoS and for this reason the launch of new satellites like NICER (Neutron star Interior Composition Explorer), a new exploration mission scheduled by NASA in 2016 [8], can be the only way for carrying on the research. Moreover, this kind of mission could be an improvement for the XNAV (X-ray pulsar-based NAVigation and timing) namely a system similar to GPS, based on the fact that periodic X-ray signals emitted from pulsars are used to determine the location of a spacecraft in deep space with an uncertainty of about 5 km.

1.2   The physics of Neutron Stars

The physics of compact objects such as neutron stars provides an intriguing interaction between nuclear processes and astrophysical observables. Neutron stars are far from those conditions possible on the ground because they have a large range of densities ranging from the stellar surface to the inner core. Clearly, the degrees of freedom are not the same in the surface region, where the density is much smaller than the saturation point of nuclear matter, and in the center of the star, where the density is so high that the models based solely on nucleon-nucleon interaction are questionable.

These features are shown in Fig 1.4. Under the atmosphere, compressed by gravity less than 1 cm in height, there is an outer crust, with a typical thickness of about 0.3 Km, composed, except that in the first tens of meters, of a lattice of bare nuclei immersed in a sea of degenerate electrons as in a normal metal. The material on the outside of the crust should be mainly ^{56}Fe, the latest product of the thermonuclear burning. With the increase of the depth, the Fermi energy of the

electrons increases, and for $\rho > 8 \cdot 10^6 \ g/cm^3$ electrons of the Fermi sea begin to be captured and converted by nuclei with protons into neutrons from the reaction $e + p \rightarrow n + \nu_e$ (neutrinos produced escape from the star). The matter becomes richer of neutrons and regrouped in a sequence of neutron-rich nuclei: for the first ^{56}Fe, ^{62}Ni and ^{64}Ni; then the nuclei with neutron shell $N = 50$ closed, ^{84}Se, ^{82}Ge, ^{80}Zn, ^{78}Ni and ^{76}Fe; followed by a sequence with $N = 82$, ^{124}Mo, ^{122}Zr, ^{120}Sr up to ^{118}Kr at a density $\rho_{drip} \approx 4 \cdot 10^{11} g/cm^3 = 2 \cdot 10^{-4} fm^{-3}$.
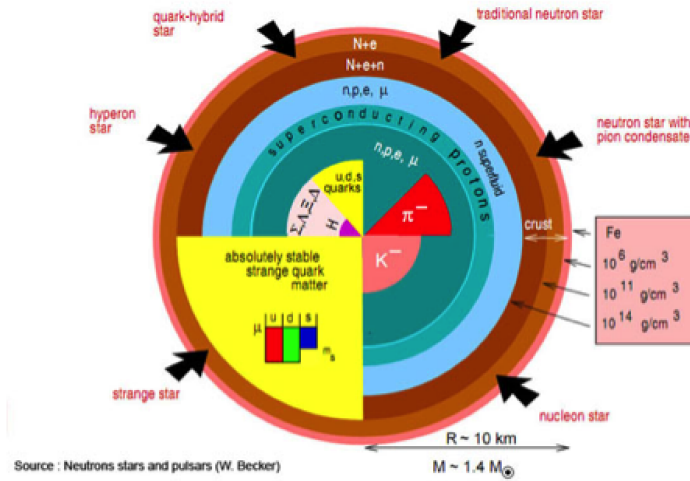
Figure 1.4: Section of a Neutron Star.

Beyond this point of "neutron drip", the material becomes so rich in neutrons that it becomes possible the state of continous neutrons, and the solid matter becomes permeated by a sea of free neutrons in addition to the sea of free electrons. This is the structure of the deep crust. The Pauli blocking of the electrons in the final state prevents nuclei in the deep crust, although unstable in the laboratories, from decaying with beta processes. The peculiar nuclei behavior results from a competition between the surface and the Coulombian energy, plus the shell structure. Beyond the drip point of neutrons, protons remain

localized in the shells with $Z = 40$ *or* 50. Then, at density about $\rho_0/3$, the Coulomb force makes unstable spherical nuclei, as in the fission. Finally, at density of about $\rho_0/2$, the matter dissolves in a uniform fluid composed mainly of neutrons, plus protons, electrons and some muon.

At higher densities, typically $2-3$ times the density of nuclear saturation, it can take place an interesting phase transition in a phase with only nucleonic degrees of freedom. In fact, several species of particles may appear due to the rapid increase of the chemical potential with the baryon density. Among these new particles there are the strange baryons, namely hyperons Λ, Σ and Ξ. Other species in the stellar matter may appear, like the Δ isobar along with kaons and pions condensates. Moreover at very high densities, as we will see in Chapter 6, is to envisage a phase transition of nuclear matter in a quark-gluon plasma (QGP).

1.3   TOV Equations

The theoretical description of a neutron star is governed by the conditions imposed by the theory of general relativity. The starting point for this study is how to determine the curvature tensor of Einstein $G_{\mu\nu}$ for a massive star:

$$G_{\mu\nu} = 8\pi G T_{\mu\nu}(\rho, P(\rho)) \tag{1.1}$$

Where G is the gravitational constant. A necessary ingredient to solve this equation is the energy-momentum tensor $T_{\mu\nu}$. We approximate the density tensor for the matter of the neutron star with a perfect fluid, i.e., a not viscous medium with total energy density ρ. In this case, the problem of finding the hydrostatic equilibrium is simplified considerably and for a configuration of the star as a symmetric static sphere, the above equation reduces to the more familiar Tolman-Oppenheimer-

Volkoff that for the pressure P and the mass m is given by

$$\frac{dP}{dr} = -\frac{Gm\rho}{\rho^2}\left(1 + \frac{P}{\rho c^2}\right)\left(1 + \frac{4\pi P r^3}{mc^2}\right)\left(1 - \frac{2Gm}{c^2 r}\right)^{-1}$$

$$\frac{dm}{dr} = 4\pi r^2 \rho \tag{1.2}$$

Where $m(r)$ is the mass contained in a sphere of radius r. The second equation describes the mass balance; the apparent Newtonian form is illusory since the space-time is curved. These equations can be integrated by an EoS as $p = p(\rho)$ and thus form a closed system to solve for $p(r), \rho(r)$ and $m(r)$. The equations are integrated from the center of the star with the following boundary conditions: $P(0) = P_c$ and $m(0) = 0$. Also, inside the star, $P > 0$ and $dP/dt < 0$. The radius of the star R is determined by the condition $P(R) = 0$. Outside of the star, i.e. for $r > R$, we have $P = 0$ and $\rho = 0$, for which the equation is obtained for $m(r > R) = MG = constant$. This amount is called "total gravitational mass of the star" and determines the total energy contained in the star itself from $E = MGc^2$. To build a model for neutron stars it is necessary to solve the TOV equations complemented by an EoS for nuclear stellar matter. Therefore, the equation of state is an essential input to the calculations for the neutron star structure.

1.4 The problem of the equation of state

For a successful theory of supernovae the first request is a good equation of state for every matter density, both below and above the saturation density. Specifically the equation of state for the pressure as a function of density and entropy is the most important requirement for a numerical calculation. In ordinary matter, Coulomb interactions among particles play an important role in providing pressure. In the

cores of stars, the pressure rises to the point where the situation be-
comes quite more different. To a reasonable approximation a compact
star like white dwarf consists of a mixture of protons, neutrons and
electrons. The pressure is provided by the quantum mechanical degen-
eracy associated with the electrons and for this reason I will start by
calculating the pressure supplied by a collection of fermions, neglect-
ing any possible interactions among them. Therefore we take a simple
model for the particles like the Fermi gas. We consider a collection of
N fermions with mass m_F confined to a cube of side L. In a standard
quantum mechanical way, we can picture these fermions as existing as
waves inside the box, with each particle having a different wavelength,
so that the volume of k-space occupied by each particle is $(2\pi L^3)/3$. It
follows that

$$N = \int_0^{k_f} \frac{4\pi k^2}{\frac{1}{2}(\frac{2\pi}{L})^3} dk, \tag{1.3}$$

where k_f is the wave number of the most energetic fermion, usually
called fermi wave number. This gives the fermion number per unit of
volume

$$n = \frac{N}{L^3} = \frac{k_f^3}{3\pi^2}. \tag{1.4}$$

If ϵ denotes the energy per unit volume, E_{total} the total energy of the
N fermions and $E_{particle}$ the energy per particle:

$$E_{total} = \int_0^{k_f} E_{particle} \frac{4\pi k^2}{\frac{1}{2}(\frac{2\pi}{L})^3} dk, \tag{1.5}$$

and so

$$\epsilon = \frac{1}{\pi^2} \int_0^{k_f} E_{particle} k^2 dk, \tag{1.6}$$

The particle energy is given by the special relativistic formula:

$$E_{particle}^2 = \hbar^2 k^2 c^2 + m^2 c^4, \tag{1.7}$$

where the momentum p has been written as $p = \hbar k$. I will now consider
two extreme cases: non-relativistic particles for low density and highly

relativistic particles for high density. In both cases it is possible to compute the energy density by making use of the thermodynamical relation

$$P = \rho\frac{\partial\epsilon}{\partial\rho} - \epsilon, \qquad (1.8)$$

where P is the pressure. By considering these two extremes, we might gain some insight into the different possible barotropic equations of state $P = P(\rho)$ for compact objects. In white dwarfs, the pressure is supplied mainly by degenerate electrons, while most of the mass is supplied by baryons (protons and neutrons). So, we will distinguish between these particles, giving them masses m_f and m_b, and will define μ as the number of baryons per fermion, probably close to two for white dwarfs. It then follows that the number of fermions per unit volume is related to the mass density by

$$n_f = \frac{\rho}{\mu m_b}. \qquad (1.9)$$

These considerations are valid in the case of non-interacting particles. If we add the interaction between the particles, things change dramatically and this is just what happens in the case of neutron stars. I will discuss this problem in the Chapter 3.

1.4.1 My Thesis Work

In this thesis I tested different microscopic EoS's with several constraints [9]. A convergent effort of experimental and theoretical nuclear physics has been developing along several years to determine or to constrain the Equation of State (EoS) of nuclear matter. Two main areas of research have provided relevant hints in this direction. The experimental data on heavy ion collisions have been systematically analyzed on the basis of detailed simulations, in order to constrain not only the density dependence of the EoS, but also its isospin dependence.

Excellent reviews on this subject can be found in the literature. On the other hand, the analysis of astrophysical observational data, noticeably on compact objects, are of great relevance for the study of the nuclear EoS. The results in this field of research can be considered complementary to the ones that can be obtained within the heavy ion research activity, because nuclear matter is involved in different physical conditions. In Neutron Stars (NS) nuclear matter is present in beta equilibrium from very low density to several times saturation density, and it is therefore extremely asymmetric, much more than nuclei in laboratory. Despite the different physical situations, an accurate microscopic theory of nuclear matter is expected to be able to explain correctly the data obtained in both physical realms. Another more phenomenological approach is based on the Energy Density Fuctional (EDF) method, in particular the Skyrme forces scheme. In this approach a phenomenological force or EDF includes a certain set of parameters that are fixed by fitting the binding energy of nuclei throughout the mass table. Some of these forces are adjusted also to microscopic nuclear matter EoS. Recently, an ample set of Skyrme forces, that have been presented in the literature, has been analyzed and confronted with the available constraints on the nuclear EoS obtained from heavy ion reactions and astrophysical objects. The few Skyrme forces that passed these tests have been then used to predict the binding energy of a wide set of nuclei, and none seems to perform satisfactorily well in this case. These results show clearly that it is not at all trivial to satisfy the constraints coming from astrophysical and heavy ion data as it was already found in [10]. Furthermore, if the nuclear mass data are included, it seems very difficult to reproduce all the data sets. It looks that the phenomenological forces are not flexible enough to this purpose. In this thesis I test the predictions of different microscopic many-body approaches with respect to the constraints coming from experiments and phenomenology.

In Chapter 4 I will show these results.

One important tool of analysis is the temperature-vs.-age cooling diagram, in which currently a few observed NS are located. NS cooling is over a vast domain of time (10^{-10}–10^5 yr) dominated by neutrino emission due to several microscopic processes. The theoretical analysis of these reactions requires the knowledge of the elementary matrix elements, the relevant beta-stable nuclear equation of state (EOS), and, most important, the superfluid properties of the stellar matter, i.e., the gaps and critical temperatures in the different pairing channels.

Even assuming (without proper justification) the absence of exotic components like hyperons and/or quark matter, the great variety of required input information under extreme conditions, that is theoretically not well under or out of control, renders the task of providing reliable and quantitative predictions currently extremely difficult.

The thesis is also focused on the problem of the theoretical determination of this important input information and reports nucleon effective masses in dense nuclear matter obtained within the Brueckner-Hartree-Fock (BHF) theoretical many-body approach. I studied the dependence on the underlying basic two-nucleon and three-nucleon interactions and provide useful parametrizations of the numerical results and some estimates of the related in-medium modification of the various neutrino emission rates in NS matter [11].

After the study of the effective masses I focused on the cooling of neutron stars related with observational data using superconductive and superfluid gaps [12]. Recently this activity has been spurred by the observation of very rapid cooling of the supernova remnant Cas A, of current age 335 years and surface temperature $T \approx 2 \times 10^6$ K, for which different analyses deduce a temperature decline of about 2 to 5 percent during the last ten years. Mass and radius of this object are not directly observed, but in recent works optimal values $M = 1.62\,\mathrm{M}_\odot$,

$R \approx 10.2\,km$ [13] or a range $M = (1.1 - 1.7)\,\mathrm{M}_\odot$, $R \approx (11.4 - 12.6)\,km$ [14] are reported, dependent on the assumed EOS.

Two major theoretical scenarios have been proposed to explain this observation: one is to assume a fine-tuned small neutron 3PF2 (n3P2) gap, $T_c \approx (5 - 9) \times 10^8\,\mathrm{K} \sim \mathcal{O}(0.1\,\mathrm{MeV})$ that generates strong cooling at the right moment due to the superfluid neutron pair breaking and formation (PBF) mechanism; the other one is based on a strongly reduced thermal conductivity of the stellar matter that delays the heat propagation from the core to the crust to a time compatible with the age of Cas A. Both explanations have in common that they exclude the possibility of large n3P2 gaps; in the first case because the corresponding critical temperature of the PBF process has to match the current internal temperature of Cas A; in the second case because such a gap would block too strongly the modified Urca (MU) cooling of the star and therefore lead to a too high temperature of Cas A.

Some alternative scenarios have also been brought forward. Amongst them, it was suggested in that the fast cooling regime observed in Cas A can be explained if the Joule heating produced by dissipation of the small-scale magnetic field in the crust is taken into account.

A common feature of all these cooling scenarios is that they exclude from the beginning the possibility of very fast direct Urca (DU) cooling, although many microscopic nuclear EOS do reach easily the required proton fractions for this process. In this thesis I will employ an EOS that does so. However, The Akmal-Pandharipande-Ravenhall (APR) variational EOS, which is perhaps the most frequently used EOS for cooling simulations (in spite of the fact that it does not reproduce the empirical saturation point of nuclear matter without an ad-hoc correction), features a rather low proton fraction and DU cooling only sets in for very heavy neutron stars, $M \geq 2\,\mathrm{M}_\odot$. Since in any case neither this nor any other EOS can currently be experimentally verified

or falsified at high density, the frequent use of one particular EOS represents an important bias that should not be underestimated.

Another critical point of most current cooling simulations is the fact that EOS and pairing gaps are treated in disjoint and inconsistent manner, i.e., a given EOS is combined with pairing gaps obtained within a different theoretical approach and using different input interactions.

In this thesis I tried to improve on both aspects, i.e., I included the DU cooling process predicted by our microscopic nuclear EOS [9], and I used compatible nuclear pairing gaps obtained with exactly the same nuclear (in-medium) interaction. Furthermore, I also employed recent results for nucleon effective masses obtained in the same approach with the same interactions, which affect the microscopic cooling reactions. Results will be shown in Chapter 5.

Finally, in Chapter 6, I discuss the "constant speed of sound" (CSS) parametrization [15] of the equation of state of high-density matter and its application to the field correlator method (FCM) model of quark matter. In this work Ref [16], performed in collaboration with Prof. M. Alford, I show how observational constraints on the maximum mass and typical radius of neutron stars are expressed as constraints on the CSS parameters. I found that the observation of a $2\,\mathrm{M_\odot}$ star already severely constrains the CSS parameters, and is particularly difficult to accommodate if the squared speed of sound in the high-density phase is assumed to be around $1/3$ or less. I prove that the FCM equation of state can be accurately represented by the CSS parametrization, which assumes a sharp transition to a high-density phase with density-independent speed of sound. I display the mapping between the FCM and CSS parameters, and I show that FCM only allows equations of state in a restricted subspace of the CSS parameters.

Lastly in Chapter 7 I show the conclusions.

Chapter 2

Supernova Explosion and Proto Neutron Stars

Although the discovery of the first supernova in modern times is attributed to Tycho Brahe, who observed this event on the evening of November 11th 1572, some astronomers preceded his observation by few days and among them it is worthwhile to mention the sicilian abbot Francesco Maurolico [17]. In any case this observation shaked the worldview that the cosmos, e.g., the sphere of the stars, everything beyond the orbit of Saturn, was unchanging and eternal as Aristotle, the great Greek philosopher, had claimed. Numerous questions arose about the nature of this so called Nova Stella. Was it something close to the earth, was it a peculiar comet? As the star faded in the months after its discovery and became invisible in 1574, leaving the world in awe and shocked, Brahe proved that the new star was something in the supra-lunar world, in the realm of the aether which was apparently not as unchangeable and eternal as Aristotle had proposed. A new era had begun, in which the state of the universe became more and more a scientific question rather than one of philosophy or religion.

At the beginning of the 20th century, pioneering work was done by Emden and Eddington (who formulated the equations of the stellar
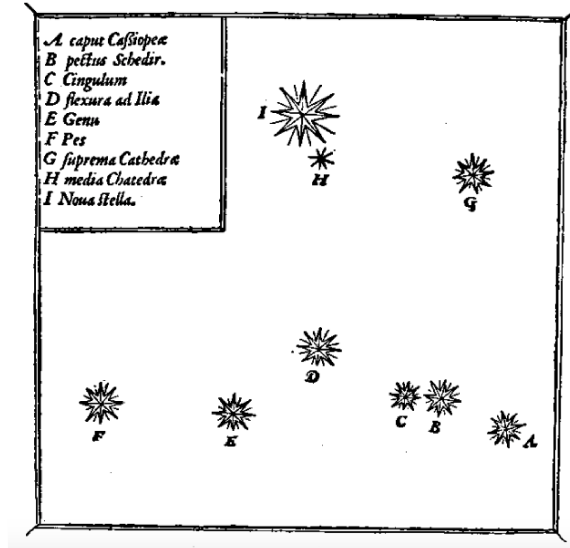
Figure 2.1: The Nova Stella (new star) in Cassiopeia (marked with I) as observed by Tycho Brahe in 1572. Figure obtained from Pannekoek (1951).

structure) and Schwarzschild (theory of radiation). Although it was already known that nuclear reactions played an important role in stellar evolution, George Gamow was the first in 1929 to propose the idea that the main source of energy of stars has to be hydrogen fusion. After this breakthrough, it still took about ten years before Hans Bethe and Carl von Weizsacker in 1938 worked out the theory of thermonuclear fusion, including the so important proton-proton chain and CNO cycle. A whole new field opened, where stellar evolution and nuclear physics were coming together, and which is still very active.

We know that all stars begin their life from a cloud of gas that starts contracting under its own gravity. Due to this contraction, the temperature and the density at the center rise. This process can continue until the conditions are suitable for the ignition of hydrogen in the center. A new star is born! The fusion of hydrogen into helium produces a lot of energy, maintaining a pressure gradient that makes

the star stable against gravity. The temperature and density inside the star remain almost constant until this energy source is exhausted. This phase is called the main sequence and takes about 80% of the lifetime of the star. When hydrogen as energy source is exhausted, the star starts contracting again. If the conditions become favorable to ignite helium, the whole cycle starts again. After helium core burning, the evolution of low, intermediate and massive stars becomes significantly different. Massive stars are defined as stars that experience a collapse of the iron core. The minimum mass for massive stars lies around 10 $M_\odot$. The evolution of massive stars proceeds through all major and advanced burning stages, e.g., hydrogen, helium, carbon, neon, oxygen, and silicon, which progressively takes shorter amounts of time. Once silicon burning is completed and an iron core is formed, instabilities develop, resulting eventually in a collapse of the core and an explosion of the star. At the time of explosion the star possesses a complex shell structure, and a shock wave travels through these shells and heats the material, resulting in various nucleosynthesis processes, producing $\approx 1/2$ of the heavy elements up to Uranium. Low mass stars develop, after hydrogen and helium core burning, an electron-degenerate carbon oxygen core which is too cool to ignite carbon burning. After core helium burning, the convective envelope moves down and penetrates in the helium layer until it reaches the boundary of the core. At this time, a double shell structure develops: the center of the star is formed by a contracting degenerate carbon oxygen core, which is surrounded by both helium and hydrogen burning shells. This structure is unstable and helium shell results in thermal pulses that are characteristic for asymptotic giant branch (AGB) stars. During this thermally pulsing AGB (TPAGB) phase, the star has a high mass loss rate, which removes the entire envelope in a short time, leaving a naked carbon oxygen core which evolves into a white dwarf.

When a massive star dies, the following dynamics of supernova explosion is mainly determined by the neutrino [3]; in fact, when a star consumes all its fuel, the forces opposed to the gravitational collapse stop and the stellar core is compressed by gravity so strongly that, in less than a second, the core reaches extreme conditions of temperature and density, namely the so-called "protostar". A large quantity of neutrinos remains momentarily trapped and thereafter, is emitted carrying away a large fraction of energy released in the collapse. The following explosion splashes away the external stellar layers leaving at the center a very dense and small object. The massive stars begin their life, like all stars with the gravitational contraction of a cloud of hydrogen. The compression increases the density, the internal pressure and the temperature of the gas. As soon as the pressure is sufficient to counteract the gravity, the star stops shrinking. If for some reason the internal pressure exceeds the gravitational force, the star expands. The pressure then decreases, and the expansion will stop when the pressure is again equal to gravity. As long as the internal pressure and gravity are balanced, the star do not expands nor contracts but will maintain the state of hydrostatic equilibrium. However a star is also hot with a temperature in the core of millions of Kelvin degrees. Heat and power range from the core to the envelope and are emitted from the surface; the star shines. The temperature and density in the core are therefore not sufficient to trigger the fusion of hydrogen in to helium, at a temperature of about 5 keV, namely

$$H + H \rightarrow D + e^+ + \nu_e \qquad (2.1)$$

This reaction is characterized by a Q of about 0.42 MeV. Its cross section is small, not only because of the Coulombian barrier to cross but also because it is a weak process. Since the combustion of hydrogen releases a large amount of energy, it is sufficient a very low rate of

fusion and hydrogen reserves last long. For a cloud of about 20 $M_\odot$, these reactions last for about 7 million years. As soon as one forms the deuterium there is the reaction

$$H + D \rightarrow {}^3He + \gamma \tag{2.2}$$

So at the end of the cycle, the nuclei of ${}^3He$ interact according to the reaction:

$${}^3He + {}^3He \rightarrow {}^4He + H + H \tag{2.3}$$
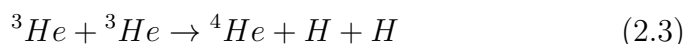
At the end of this chain of reactions, for 4 protons consumed one has a helium nucleus, and it is released energy in the order of 26.7 MeV. When helium becomes abundant compared to hydrogen, the energy generated by the fusion of hydrogen becomes insufficient to compensate the loss of energy via radiation (photons and neutrinos). The balance is broken and the star begins to contract until the core temperature is high enough to burn helium for producing carbon. It produces new energy and restore balance. The star will still contain hydrogen, which now surrounds a burning core of helium. As soon the helium ends, the fusion stops and the star contracts whereas the temperature increases, until it becomes possible the fusion of the carbon and so on, up to produce increasingly heavier elements like neon oxygen and silicon. The star develops a structure similar to onion. As the elements become more and more heavy, the energy produced in the individual reactions decreases so the rate of burning fuel must increase, in order to release enough energy to sustain the pressure of the core. Although a heavy star (about $25\,M_\odot$) burns hydrogen and helium for millions of years, it will burn carbon for about 600 years and oxygen for only 6 months. The combustion of silicon lasts only one day. The silicon burns to become iron but once formed the iron, the process of energetic release for thermonuclear fusion stops. In fact, iron is the most bound nucleus and every process of fusion or fission absorbs energy rather than release

it. Thus the formation of the iron is the beginning of the end of massive stars. As this energy is released, the pressure of the core drops and rapidly loses support, imploding, because gravity does collapse under its own weight. The core has a temperature of about 0.7 MeV, density about $3 \cdot 10^9$ g/cm^3 and a mass of about 1.4 $M_\odot$. The collapse occurs in less than one second. Since the density of the core increases, the Fermi momentum of electrons increases rapidly. The energy of degeneration increases with the density and the superdense core exceeds 2.25 MeV necessary to a free electron to convert a free proton in a neutron:

$$p + e^- \rightarrow n + \nu_e \tag{2.4}$$

This process, called neutronization, produces an electron neutrino that takes away energy. Through this mechanism, the pressure of the electrons decreases and the collapse accelerates. The collapse could continue indefinitely if did not form the degenerate gas of nucleons. In fact, at the high density of the core, the nucleons produce an elevated pressure and as soon as the density exceeds 10^{14} g/cm^3, the nucleons are "compressed" together; at this point nuclear forces become important because they are repulsive at small distances. These provide other pressure in addition to that one from degeneration. Then the internal pressure begins to increase dramatically and once the central density exceeds $3 \cdot 10^{14} g/cm^3$, the pressure becomes so high that the iron core becomes incompressible. The collapse suddenly stops. At this point, something of special happens; like a supercompress rubbery ball is released suddenly returning on equilibrium, the inner core expands violently. It is what is called "core bounce"; a layer of dense matter is projected outwardly to approximately 10000 km/sec and a wave of shock begins to open a passage through the material which is still falling to about 60000 km/sec. The wave of shock quickly loses energy and the rapid expansion stops. So, as a result of the rebound of

the core, one forms a layer of relatively static dense and warm matter less dense than the inner core but more dense than the outer material that continues to fall. This layer becomes thicker than the other falling material. The central part of this dense layer, which has a radius of about 40 km and includes the inner core, plays a crucial role in the formation of the supernova, and is called "protostar". This has a mass of about 1.2 $M_\odot$ and consists of electrons, neutrinos and nuclear matter. After approximately 10 seconds, it cools and condenses to become the well known neutron star as the final product of the explosion. But the problem today is to understand what happens physically in postbounce. The problem is understand how to pass from an implosion to an explosion. It seems that the crucial role is played by the neutrinos. In fact, the neutronization of the core produces neutrinos. Although the interactions of these particles with matter are extremely weak with cross sections typically of the order of $10^{-44} cm^2$, they play a fundamental role in the evolution of the postbounce. The importance of the neutrinos had already been understood by Colgate and White when they proposed the first model of supernova explosion in 1966. In this model, the neutrinos produced by electron capture leave the core without further interaction. This is possible because the rates of the reactions

$$\nu_e + n \to p + e^- \quad , \quad \nu_e + e^- \to \nu_e + e^- \tag{2.5}$$
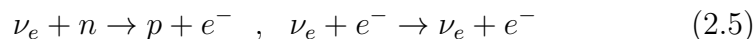
are very low at the densities typical of the core and this is due to the Pauli blocking of the electrons in the final state. However, neutrinos can interact with matter out of the core where the density is low. So they can transfer momentum to the stellar layers and produce an explosion outside of the envelope that leads to the formation of a neutron star. The model Colgate and White had been well accepted for several years until Dan Friedman re-examined in 1974 in light of Standard Model. In fact, at that time, Standard Model had received a spectac-

ular confirmation with the discovery of neutral currents, mediated by Z_0 boson. Friedman pointed out that the neutral currents can give rise to new types of reactions as

$$\nu_e + p \rightarrow \nu_e + p \ \ , \ \ \nu_e + n \rightarrow \nu_e + n \tag{2.6}$$

The rates of these reactions are similar to those of reactions induced by charged currents but are not low for density values typical of the core since there are no electrons in the final state. Moreover, Friedman pointed out that the cross sections in the case of neutral currents can increase dramatically thanks to the possibility of having coherent scattering from nuclei (which does not exist for charged currents mediated by the exchange of $W^{\pm}$). The corresponding cross section is A^2 times the elementary cross section, where A is the number of nucleons involved. This factor combined with the high-density can produce a tiny mean free path for neutrinos. Neutrinos are so trapped in density greater than about $10^{11} \ g/cm^3$ so they are not able to transfer their momentum to the outer shell. How then is it possible to understand the explosion and the formation of the neutron star? The situation changed dramatically on the night of February 23th, 1987 when a bright supernova exploded in the Large Magellanic Cloud, 160000 light years away from Earth, the brightest supernova after that one observed by Kepler in 1604 and was named $SN1987A$. It was observed in the southern hemisphere observatory in Las Campanas (Chile) and was so bright that it could be observed with the naked eye. The progenitor was a blue giant about 20$M_\odot$. Supernova $SN1987A$ is the only one from which it was possible to observe neutrinos. Two underground detectors, Kamiokande II and IMB in Japan in Ohio, recorded two flashes of 12 and 8 electronic antineutrinos on a time interval of 10 seconds. The low number of events did not permit a detailed modeling of $SN1987A$ but provided qualitative estimates of what had happened. The detected

signal confirms the description of a hot protostar which forms and cools thanks to the neutrino emission and is entirely consistent with current theories of the core collapse. The energies of the neutrinos correspond to the initial temperature of the protostar while the duration of the lightning is in line with the cooling time of 10 seconds, calculated for this type of objects. The energy spectrum of the neutrinos allowed an estimate of the total energy radiated during the supernova that is consistent with the creation of a 1.4 $M_\odot$ neutron star with radius within 15 Km. At the same time, the analysis of the emission spectra showed that the envelope ejected was quite mixed, i.e. iron contained in the outer layers of helium and hydrogen, indicating that a certain mixing had occurred over large distances. The mixing was explained, regardless of Epstein (Los Alamos) and Bethe, from convective instability arising while the shock wave propagates away from the core to the surface of the star long after the explosion occurred. A protoneutron star (PNS) is formed after the explosion of a supernova and it remains in a transient state between both neutron star and black hole for tens of seconds. Initially, the PNS is optically dense of neutrinos, i.e. they are temporarily trapped inside the star. The next evolution of the PNS is dominated by the diffusion of neutrinos, which affects primarily on deleptonization and then on cooling. After a time much greater, the emission of photons competes with the emission of neutrinos in the cooling process of the star. Two new effects should be considered talking to PNS. The first one concerns the thermal effects which affect the production of entropy, with values of some units for baryon, and temperatures above $30 - 40\ MeV$. The second one, the fact that neutrinos are trapped in the star, which means that the chemical potential of neutrinos is not null. This alters the chemical balance and changes its composition. Both effects can lead to observable consequences in the signals of neutrinos from a supernova and can also play in important

role in determining whether a given supernova ends the process in a cold neutron star or a black hole.

Chapter 3

Theoretical Approaches

Contents

Firstly we can assume that the hadron constituents of matter inside neutron stars are only nucleons. We can use two completely different approaches to describe the strong interaction among nucleons. One is normally called microscopic approach and the other is the phenomenological approach. In microscopic approach the starting point is the nucleon-nucleon interaction as described by the so-called realistic interaction potentials such as Argonne, Bonn, Nijmegen, Paris, Urbana. The theoretical basis for building these realistic potentials is the theory of the exchange of mesons of the nuclear force. In this scheme the nucleons, mesons and resonances as π, ρ and ω are incorporated in one single potential. The various parameters in the potential are then adjusted to reproduce the experimental data for the two-body problem (the properties of deuterium and the phase shift of nucleons). Then one can solve the problem using the many-body EoS. The various methods to solve the many-body problem and the limitations of the microscopic calculation of EoS will be discussed later. In the phenomenological approach, the starting point is the dependence of the interaction with the density. The parameters that appear in this phenomenological interaction are adjusted to reproduce the properties of nuclei and the empirical properties of nuclear matter. The most popular of this type of interaction is the Skyrme interaction. The EoS can be deduced from the effective interaction in a very simple way and it is possible to derive analytical expressions for many thermodynamic quantities. The phenomenological approach is obviously less fundamental than the microscopic one but nevertheless has a number of advantages. First of all the simplicity of calculation to obtain the EoS compared to the complicated calculation of many bodies which requires the microscopic approach. In addition, the phenomenological EoS can be easily extrapolated in regions far from the area where the parameters have been set. However, as we shall see later, the behavior of dense and asym-

metric nuclear matter is closely related to quantity as the symmetry energy, density, impulse and asymmetry of single particles like neutrons and protons. All these quantities are very poorly constrained by experimental data. Therefore, a simple extrapolation to the extreme conditions of high density and asymmetry between neutrons and protons is not fully trusted, or at least can be quite arbitrary. In fact, one could be introduced phenomenological models of $EoSs$ that reproduce also the saturation properties of symmetric nuclear matter and finite nuclei but which are very different in the region of high density and high asymmetry. The determination of the microscopic EoS can be very helpful to clarify these ambiguities. However, any realistic EoS must meet the following basic requirements:

a) It must reproduce the empirical point of saturation for symmetric nuclear matter (SNM) and the energy per nucleon at the saturation point, namely

$$n_0 = 0.17 \pm 0.01 \ nucleons \cdot fm^{-3}, E_0/A = -16 \pm 1 \ MeV \qquad (3.1)$$

b). It must give an energy of symmetry at the saturation point compatible with the nuclear phenomenology

$$E_{sym} = 30 \pm 2 \ MeV \qquad (3.2)$$

c) The compressibility K_0 of Symmetric Nuclear Matter (SNM) at the saturation point must be compatible with experimental data

$$K_0 = 220 \pm 30 \ MeV \qquad (3.3)$$

d) Both for pure neutronic matter and symmetric matter, the speed of sound must not exceed the speed of light (condition of causality), namely

$$s/c = \left(\frac{dP}{d\epsilon}\right)^{1/2} \leq 1. \qquad (3.4)$$

In this thesis I will concentrate on the microscopic approaches [9], the only input being a realistic free nucleon-nucleon (NN) interaction with parameters fitted to NN scattering phase shifts in different partial wave channels, and to properties of the deuteron. In the following I discuss the non-relativistic Brueckner-Hartree-Fock (BHF) method, its relativistic counterpart, the Dirac-Brueckner $-$ Hartree-Fock (DBHF) approximation and the Variational method. There are also other models (which are not the subject of this thesis) such as the Phenomenological models with many free parameters to be fitted to experimental NN data, the Boson-Exchange models based on the field-theoretical and dispersion-relations methods, the QCD models based on the fundamental quarks and gluons degrees of freedom, and the models based on EFT (Effective Field Theory) [18] by using the chiral symmetry of QCD. Once the interaction between two nucleons is established, one can try to solve the many-body problem for the nuclear matter [19]. However, it is not obvious that the nuclear Hamiltonian includes only two-body forces. Since we know that the nucleon is not an elementary particle, we can expect that the interaction in a system of nucleons is not fully additive, namely that it is not simply the sum of the interactions between pairs of nucleons, but also three or more nucleon forces must be considered. This important issue is discussed in Section 3.7. For the moment we restrict the treatment to the case of two-body forces, which are expected anyhow to be dominant around saturation or slightly above.

3.1 The Brueckner-Bethe-Goldstone expansion

The Brueckner-Bethe-Goldstone (BBG) many-body theory is based on the re-summation of the perturbation expansion of the ground state

energy. The original bare NN interaction is systematically replaced by an effective interaction that describes the in-medium scattering processes. The in-vacuum T-matrix is replaced by the so called G-matrix, that takes into account the effect of the Pauli blocking on the scattered particles and the in-medium potential $U(k)$ felt by each nucleon. The corresponding integral equation for the G-matrix can be written

$$\langle k_1 k_2 | G(\omega) | k_3 k_4 \rangle = \langle k_1 k_2 | v | k_3 k_4 \rangle + \sum_{k_3' k_4'} \langle k_1 k_2 | G(\omega) | k_3' k_4' \rangle \cdot$$

$$\cdot \frac{(1 - \Theta_F(k_3'))(1 - \Theta_F(k_4'))}{\omega - e_{k_3'} + e_{k_4'}} \langle k_3' k_4' | G(\omega) | k_3 k_4 \rangle \qquad (3.5)$$

where the two factors $1 - \Theta_F(k)$ force the intermediate momenta to be above the Fermi momentum ("particle states"), the single particle energy $e_k = \hbar^2 k^2 / 2m + U(k)$ and the summation includes spin-isospin variables. The G-matrix has not any more the hard core of the original bare NN interaction and is defined even for bare interaction with an infinite hard core. In this way the perturbation expansion is more manageable. The introduction and choice of the single particle potential are essential to make the re-summed expansion convergent. In order to incorporate as much as possible higher order correlations the single particle potential is calculated self-consistently with the G-matrix itself:

$$U(k; \rho) = \sum_{k' \leq k_F} \langle k k' | G(e_{k_1} + e_{k_2}) | k k' \rangle. \qquad (3.6)$$

Here we restrict to indicate the expression of the correlation energy at the so called Brueckner level ("two hole-line" approximation)

$$\Delta E_2 = \frac{1}{2} \sum_{k_1', k_2' < k_F} \langle k_1 k_2 | G(e_{k_1} + e_{k_2}) | k_3 k_4 \rangle_A$$

where

$$|k_1 k_2 \rangle = |k_1 k_2 \rangle - |k_2 k_1 \rangle. \qquad (3.7)$$

At this level of approximation, which mainly includes two-body correlations, one can find that the corresponding ground state wave function Ψ can be written consistently as

$$|\Psi> = e^{\hat{S}_2}|\Phi> \qquad (3.8)$$

where Φ is the unperturbed free particle ground state and $\hat{S}_2$ is the two-particle correlator

$$\hat{S}_2 = \sum_{k_1,k_2,k_1',k_2'} \frac{1}{4} \langle k_1' k_2'|S\dot{}n|k_1 k_2 \rangle \, a^\dagger(k_1')a^\dagger(k_2')a(k_2)a(k_1) \qquad (3.9)$$

where the k''s are hole momenta, i.e. inside the Fermi sphere, and the k''s are particle momenta, i.e. outside the Fermi sphere. The function $\hat{S}_2$ is the so called "defect function". It can be written in term of the G-matrix and it is just the difference between the in-medium interacting and non interacting two-body wave functions.

One of the well known results of all these studies, that lasted for about half a century, is the need of three-body forces (TBF) in order to get the correct saturation point in symmetric nuclear matter. Once the TBF are introduced, the resulting EoS, for symmetric matter and pure neutron matter, is reported in Fig.(3.1) for the two-body interaction Av_{18} (squares). The TBF's produce a shift in energy and in density. This adjustment is obtained by tuning the two parameters contained in the TBF and was performed to get an optimal saturation point (the minimum).

Special attention must be paid to the sub-saturation region of nuclear EoS. At very low-density homogeneous matter must behave as a free Fermi gas, and therefore, as discussed above, the energy per particle must increase with density. To join the region just below saturation, where the energy is a decreasing function of density, a point where the compressibility vanishes must exist. Below this point (lower
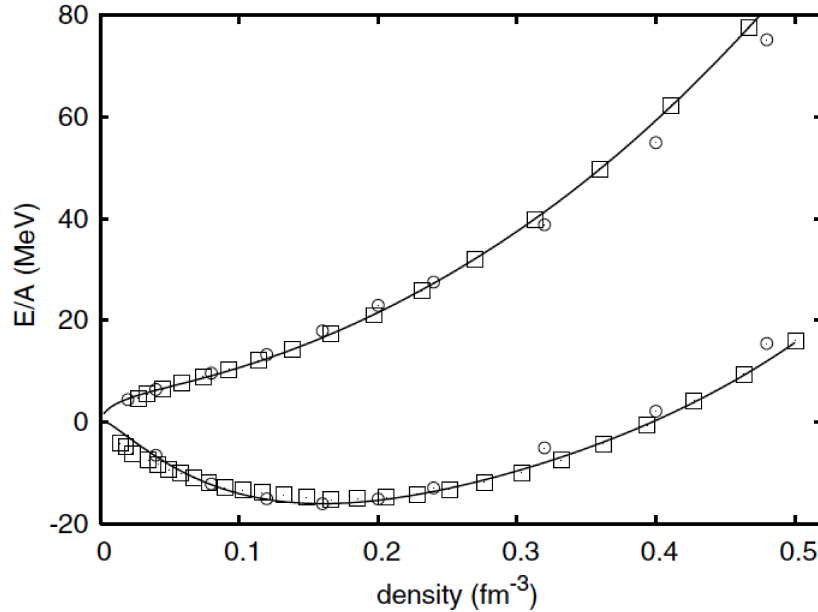
Figure 3.1: Symmetric and pure neutron matter EOS from BHF scheme including TBF (squares). The full lines is a fit to the points.

density) the compressibility is negative, while above it is positive. If the compressibility is negative, nuclear matter is unstable towards cluster formation, that is light nuclei are formed and coexist with the bulk. Of course this transition must be present in any calculated *EoS*, and it is not a peculiarity of the BBG method. The density of the transition point is estimated to be around 2/3 of the saturation density (for symmetric nuclear matter).

3.2 The Variational method

In the variational method [20] one assumes that the ground state wave function Ψ can be written in the form

$$\Psi(r_1, r_2, ...) = \Pi_{i<j} f(r_{ij}) \Phi(r_1, r_2, ...) , \qquad (3.10)$$

where Φ is the unperturbed ground state wave function, properly antisymmetrized, and the product runs over all possible distinct pairs of particles. The correlation factor is here determined by the variational principle, i.e. by imposing that the mean value of the Hamiltonian gets a minimum

$$\frac{\delta}{\delta f} \frac{\langle \Psi | H | \Psi \rangle}{\langle \Psi | \Psi \rangle} = 0 . \tag{3.11}$$

In principle this is a functional equation for the correlation function f, which however can be written explicitly in a closed form only if additional suitable approximations are introduced. The function $f(r_{ij})$ is assumed to converge to 1 at large distance and to go rapidly to zero as $r_{ij} \rightarrow 0$, to take into account the repulsive hard core of the NN interaction. Furthermore, at distance just above the core radius, a possible increase of the correlation function beyond the value 1 is possible.

For nuclear matter it is necessary to introduce a channel dependent correlation factor, which is equivalent to assume that f is actually a two-body operator $\hat{F}_{ij}$. One then assumes that $\hat{F}$ can be expanded in the same spin-isospin, spin-orbit and tensor operators appearing in the NN interaction. Momentum dependent operators, like spin-orbit, are usually treated separately. The product in equation must be then symmetrized since the different terms do not commute anymore.

If the two-body NN interaction is local and central, its mean value is directly related to the pair distribution function $g(\mathbf{r})$

$$< V >= \frac{1}{2}\rho \int d^3 r v(r) g(\mathbf{r}) , \tag{3.12}$$

where

$$g(\mathbf{r_1} - \mathbf{r_2}) = \frac{\int \Pi_{i>2} d^3 r_i |\Psi(r_1, r_2....)|^2}{\int \Pi_i d^3 r_i |\Psi(r_1, r_2....)|^2} . \tag{3.13}$$

The main job in the variational method is to relate the pair distribution function to the correlation factors F. Again, in nuclear matter also the pair distribution function must be considered channel dependent and the relation with the correlation factor becomes more complex. In general this relation cannot be worked out exactly, and one has to rely on some suitable expansion. Furthermore, three-body or higher correlation functions must in general be introduced, which will depend on three or more particle coordinates and describe higher order correlations in the medium. Many excellent review papers exist in the literature on the variational method and its extensive use for the determination of nuclear matter EoS Ref [21, 20]. The best known and most used variational nuclear matter EoS is the one calculated by Akmal, Pandharipande and Ravenhall Ref [22]. In their paper the authors showed calculations using the Argonne V_{18} NN interaction Ref [23], with boost corrections to the two-nucleon interaction, which give the leading relativistic effect of order $(v/c)^2$. This latter EoS will be tested in this thesis.

3.3 The Relativistic approach

The relativistic framework is the one on which the nuclear EoS should be ultimately based. The best relativistic treatment developed so far is the Dirac-Brueckner (DBHF) approach [9]. The DBHF method can be developed in analogy with the non-relativistic case, i.e. the nucleon inside the nuclear medium is viewed as a dressed particle in consequence of its two-body interaction with the surrounding nucleons. The two-body correlations are described by introducing the in-medium relativistic G-matrix. The DBHF scheme can be formulated as a self-consistent problem between the single particle self-energy Σ and the G-matrix.

Schematically, the equations can be written

$$G \; = \; V + i \int VQggG \tag{3.14}$$

$$\Sigma \; = \; -i \int_F (Tr[gG] - gG) \tag{3.15}$$

where Q is the Pauli operator which projects the intermediate two particle momenta outside the Fermi sphere, as in the BBG G-matrix equation, and g is the single particle Green's function, which fulfills the Dyson equation

$$g = g_0 + g_0 \Sigma g \tag{3.16}$$

where g_0 is the (relativistic) single particle Green's function for a free gas of nucleons, and Σ is the nucleon self-energy which expresses the influence of the surrounding nucleons. The self-energy can be expanded in the covariant form

$$\Sigma(k, k_F) = \Sigma_s(k, k_F) - \gamma_0 \Sigma_0(k, k_F) + \boldsymbol{\gamma} \cdot \mathbf{k} \Sigma_v \tag{3.17}$$

where γ_μ are the Dirac gamma matrices, and the coefficients of the expansion are scalar functions, which in general depend on the modulus $|\mathbf{k}|$ of the three-momentum and on the energy k_0. The free single particle eigenstates, which determine the spectral representation of the free Green's function, are solutions of the Dirac equation

$$[\; \gamma_\mu k^\mu \; - \; M \;] \, u(k) \; = \; 0 \tag{3.18}$$

where u is the Dirac spinor at four-momentum k. For the full single particle Green's function g the corresponding eigenstates satisfy

$$[\; \gamma_\mu k^\mu \; - \; M \; + \; \Sigma \;] \, u(k)^* \; = \; 0 \tag{3.19}$$

Inserting the above general expression for Σ after a little manipulation one gets

$$[\; \gamma_\mu k^{\mu *} \; - \; M^* \;] u(k)^* \; = \; 0 \tag{3.20}$$

with

$$k^{0*} = \frac{k^0 + \Sigma_0}{1 + \Sigma_v} \quad ; \quad k^{i*} = k^i \quad ; \quad M^* = \frac{M + \Sigma_s}{1 + \Sigma_v} \qquad (3.21)$$

This is the Dirac equation for a single particle in the medium, and the corresponding solution is the spinor

$$u^*(\mathbf{k}, s) = \sqrt{\frac{E_\mathbf{k}^* + M^*}{2M^*}} \left(\begin{array}{c} 1 \\ \frac{\boldsymbol{\sigma} \cdot \mathbf{k}}{E_\mathbf{k}^* + M^*} \end{array} \right) \chi_s \quad ; \quad E_\mathbf{k}^* = \sqrt{\mathbf{k}^2 + M^{*2}} \quad . \quad (3.22)$$

In line with the Brueckner scheme, within the BBG expansion, in the self-energy of equation only the contribution of the single particle Green's function pole is considered. Furthermore, negative energy states are neglected and one gets the usual self–consistent condition between self–energy and scattering G–matrix.

In any case, the medium effect on the spinor of equation is to replace the vacuum value of the nucleon mass and three–momentum with the in–medium values of equation. This means that the in-medium Dirac spinor is "rotated" with respect to the corresponding one in vacuum, and a positive (particle) energy state in the medium has some non–zero component on the negative (anti–particle) energy state in vacuum. In terms of vacuum single nucleon states, the nuclear medium produces automatically anti–nucleon states which contribute to the self–energy and to the total energy of the system. It has been shown that this relativistic effect is equivalent to the introduction of well defined TBF's at the non–relativistic level. These TBF's turn out to be repulsive, and consequently produce a saturating effect. Actually, including in BHF only these particular TBF's, one gets results close to DBHF calculations. Generally speaking, the DBHF gives in general a better saturation point than BHF, and the corresponding EoS turns out to be stiffer above saturation than the one calculated from the BHF + TBF method.

In the relativistic context the only NN potentials which have been developed are the ones of one boson exchange (OBE) type. In the results shown in this thesis the Bonn A potential is used.

3.4   Two-Nucleon Systems

Nucleon-Nucleon interaction is always divided into three parts as follows:

a) The long-range (LR from now on) part ($r \geq 2fm$). In most models, it is considered as One-Pion-Exchange Potential ($OPEP$) and is added to the other parts of the potential as a tail. In a simple form in r-space, it reads

$$V_{OPEP}^{(1)}(r) = \frac{g_{pi}^2}{3}(\vec{\tau}_1 \cdot \vec{\tau}_2)\left[\frac{e^{(-\mu r)}}{r}(\vec{\sigma}_1 \cdot \vec{\sigma}_2) + \left(1 + \frac{3}{\mu r} + \frac{3}{(\mu r)^3}\right)\frac{e^{-\mu r}}{r}S_{12}\right]$$

$$(3.23)$$

where $\mu = 1$, $r_0 = \frac{\hbar}{m_{pi}c}$ and $S_{12} = 3(\vec{\sigma}_1 \cdot \hat{r})(\vec{\sigma}_2 \cdot \hat{r}) - (\vec{\sigma}_1 \cdot \vec{\sigma}_2)$ is the usual tensor operator; and g_{pi} is the coupling constant, which is obtained from the experiments with mesons (meson-nucleon scattering). This potential has earned some improvements such as considering the difference between the neutral and charged pions and that it is different for pp, nn, np interactions besides the clear forms raised from some new models of NN interaction.

b) The intermediate/medium (MR from now on)$-$range part ($1fm \leq r \leq 2fm$). It comes from the various single-meson exchanges and mainly from the scalar-meson exchanges (two pions and heavier mesons).

c) The short-range (SR from now on) part ($r \leq 1fm$). It is always given by exchanges of the vector bosons (heavier mesons and multi-pion exchanges) as well as the QCD effects. In some of the potential forms, various Feynman diagrams, dependent on the considered exchanges, in each of the three mentioned parts, are used. A general scheme for NN
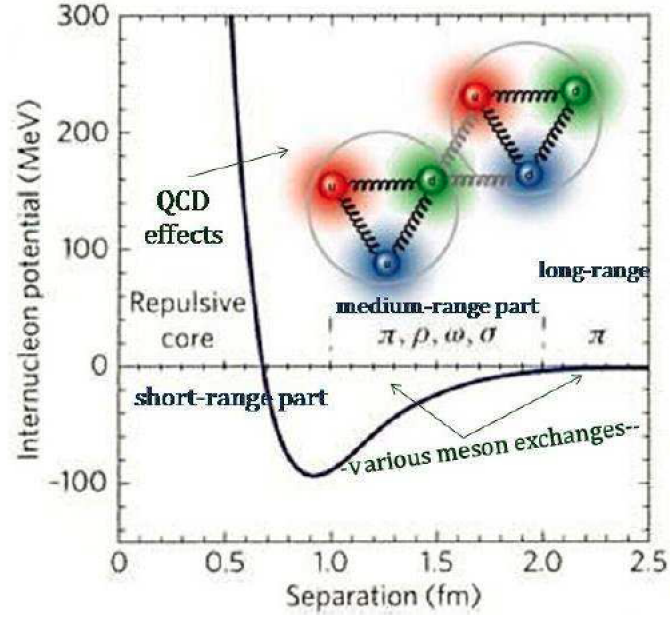
Figure 3.2: A general scheme for nucleon-nucleon potential

potential is shown in Fig. 3.2. One way to study the nuclear two-body interactions is using a two-nucleon system such as deuteron (the $2H$ nuclei). Detailed studies need a general system of two-nucleon which is, in turn, framed through scattering a nucleon from another nucleon. Nevertheless, deuteron is still fundamental to understand some basic properties of NN interaction. Deuteron is the exclusive loosely bound-state of two-nucleon system. From the symmetry considerations, $3S1$ and $3D1$ are its states. Its nonzero electric quadrupole-moment,

$$Q = \frac{\sqrt{2}}{10} \int_0^{+\infty} uwr^2 dr - \frac{1}{20} \int_0^{+\infty} w^2 r^2 dr, \qquad (3.24)$$

confirms the presence of D-state and leads to introduce the tensor force. As a partial way to measure the quality of a potential, one may insert the wave functions for the S-state ($u(r)$) and the D-state ($w(r)$), gained from a special potential, into the last equation and then compares the

results with the experimental values.

3.5   Argonne V_{18} Potential

The $Argonne V_{18}$ (AV18) [23] potential is an updated version of the nonrelativistic Argonne potential ($Argonne V_{14}$) that fits both np data and pp data, as well as low-energy nn data scattering parameters and deuteron properties. The potential was directly fit to the Nijmegen NN scattering database, which contains 1787 pp and 2514 np data in the range $0 - 350\ MeV$, and has an excellent χ^2 per datum of 1.09. The strong interaction part of the potential is projected into an operator format with 18 terms: a charge-independent part [24] with 14 operator components (as in the older $Argonne V_{14}$)

$$1, \sigma_i \cdot \sigma_j, S_{ij}, L \cdot S, L_2, L_2 \sigma_i \cdot \sigma_j, (L \cdot S)^2,$$

$$\tau_i \cdot \tau_j, (\sigma_i \cdot \sigma_j), S_{ij}\tau_i \cdot \tau_j, L \cdot S(\tau_i \cdot \tau_j), L_2(\tau_i \cdot \tau_j), L_2(\sigma_i \cdot \sigma_j)(\tau_i \cdot \tau_j), (L \cdot S)^2(\tau_i \cdot \tau_j),$$
$$\tag{3.25}$$

where

$$S_{ij} = 3(\vec{\sigma_i} \cdot \hat{r_{ij}})(\vec{\sigma_j} \cdot \hat{r_{ij}}) - \vec{\sigma_i} \cdot \vec{\sigma_j}. \tag{3.26}$$

The first eight operators are the standard ones required to fit singlet and triplet S- and P-wave data. The four L operators provide for differences between S and D waves, and P and F waves. The $(L \cdot S)^2$ operators provide an independent way of splitting triplet states with different J values. These 14 operators provide sufficient freedom to characterize the 14 singlet and triplet S, P, D, and F states. Then we have a charge-independence breaking part that has three charge-dependent operators

$$T_{ij}, (\sigma_i \cdot \sigma_j)T_{ij}, S_{ij}T_{ij} \tag{3.27}$$

where $T_{ij} = 3\tau_{zi}\tau_{zj} - \tau_i \cdot \tau_j$ is the isotensor operator, defined analogous

to the S_{ij} operator; and one charge-asymmetric operator

$$\tau_{zi} + \tau_{zj} \tag{3.28}$$

The potential includes also a complete electromagnetic potential, containing Coulomb, Darwin-Foldy, vacuum polarization, and magnetic moment terms with finite-size effects. Matrix elements of the NN interaction can be specified either in particle-particle (pp) coupling or in particle-hole (ph) coupling. Both of the matrix elements completely specify the interaction, and either set can be calculated from the other set. The $Argonne V_{18}$ potential has the following general form:

$$V = V_{EM} + V_N + V_\pi + V_R, \tag{3.29}$$

where V_π is for an LR OPEP, V_R is for MR and SR parts (called the Remaining part), and V_{EM} is for electromagnetic (EM) part. The EM part, in turn, reads

$$V_{EM} = V_{C1}(r) + V_{C2}(r) + V_{DF}(r) + V_{VP}(r) + V_{MM}(r) \tag{3.30}$$

where the terms with the indices $C1, C2, DF, VP$ and MM stand for one-photon, two-photon, Darwin-Foldy, vacuum-polarization and magnetic $-$ moment interactions. In these interactions, some short-range terms and the effects due to finite size of nucleon are also included. The terms of V_{C2}, V_{DF}, V_{VP} are used just for pp scattering while the other terms have its own forms for each three scattering cases; and for nn scattering, just V_{MM} is used. The various EM potentials are given through some combinations of the following functions, with masses, coupling constants, coefficients and other constants determined from other sources or from experimental data.

3.6 Bonn Potentials

The Bonn-group [25] has used the field-theoretical methods to deal with NN interaction problem. In the first version, in 1987, they presented

a comprehensive NN potential by including various meson-exchanges which are important below the pion-production threshold. To do so, the mesons of π, ω, δ as $OBE's$ (One Boson Exchange) and $\rho, 2\pi$ (as the direct exchange and $\Delta_{(1232)}$ - (isobar excitation) as TPE's (Two Pion Exchange) as well as a special combination of $\pi\rho$ were considered. There were also $3\pi, 4\pi$ exchanges that did not have significant contributions. Indeed, the OBE contributions provided good descriptions of high l phase shifts while the TPE's with $\pi\rho$ combination provided good descriptions of low l phase shifts. So, in general, the exchanges of π and ω together with ρ and 2π provided good descriptions of the LR and MR (high l's) parts while for good describing the SR part (low l's), including the $\pi\rho$ combination next to 2π exchange was required. We should also mention that the δ meson was needed to provide a consistent description of $S - wave$ phase shifts, and that including the crossed-box diagrams in the two-boson-exchanges (TBE's) (Two Boson Exchange) made another fitting quality of the potential. This Full-Bonn (Bonn87 or Bonn-A) potential is originally written in p-space and is energy dependent that makes its applications in nuclear calculations problematic. To resolve some of the problems, a parameterization of the potential in terms of $OBE's$ in both p-space and r-space is given, which is always called Bonn-B (or Bonn89) potential.

The Bonn Charge-Dependent (CD-Bonn) NN potential [23] is an improved and updated version of the previous Bonn-A and Bonn-B potentials. It is based on the OBE contributions of π, ρ, ω mesons next to two scalar-isoscalar mesons of σ_1, σ_2, where the latter simulates the roles of $2\pi + \pi\omega$ exchanges. The resultant potential is energy-independent and produces the results of Full-Bonn potential. Although CSB (Charge Symmetry Breaking) in the potentials is mainly due to the difference between the proton and neutron masses (the nucleon mass splitting), in CD-Bonn potential an equivalent contribution is due to

TBE (mainly 2π and $\pi\rho$ exchange) diagrams. On the other hand, CIB (Charge Independent Breaking) is mainly due to the difference between the neutral and charged−pion masses (the pion mass splitting) from OPE diagram, while in $CD - Bonn$ potential an almost equivalent contribution (about 50%) is due to TBE and $\pi\gamma$ diagrams for $l > 0$ (or with the predictions of Full-Bonn model due to 2π as well as 3π and 4π exchange diagrams). To see CIB in the potential, we first note that although the OPE amplitudes in the potential are nonlocal, but in the local/static approximation and after a Fourier transformation, the local $OPEP$ in r-space reads

$$V_{OPEP}^{(4)}(m_{pi}) = \frac{g_{pi}^2}{12} \left(\frac{m_{pi}}{2M^2}\right) \left[\left(\frac{e^{-\mu r}}{r} - \frac{4\pi}{\mu^2}\delta^3(\vec{r})\right)(\vec{\sigma}_1 \cdot \vec{\sigma}_2) \right.$$
$$\left. + \left(1 + \frac{3}{\mu r} + \frac{3}{(\mu r)^3}\right)\frac{e^{-\mu r}}{r}S_{12}\right] \quad (3.31)$$

where $\mu = \frac{m_\pi c}{\hbar}$. Now, because of the pion mass splitting (as the main CIB factor), we have

$$V_{OPEP}^{pp} = V_{OPEP}^{(4)}(m_{\pi_0}),$$
$$V_{OPEP}^{np} = -V_{OPEP}^{(4)}(m_{\pi_0}) \pm 2V_{OPEP}^{(4)}(m_{\pi_\pm}), \quad (3.32)$$

where in the second relation, $+$ $(-)$ is for $T = 1$ $(T = 0)$. We see that because of the pion mass differences, the np $OPEP$ with $T = 1$ is weaker than that of pp, leading to CIB. It is also notable that the Δ-isobar states and multi-meson exchanges in Full-Bonn (Bonn-A) potential caused the energy dependence which was in turn problematic in applying the potentials to direct nuclear calculations.

So, in CD-Bonn potential (also in $Bonn-B$ potential) this problem is avoided by using just OBE contributions. The three potentials of pp, np, nn are not independent but they are related by CSB and CIB. Each of them is first fitted to the related Nijmegen phase shifts. The base phase shifts are a sum of the Nijmegen-group ones up to 1992,

used also in $Argonne V_{18}$ potential, besides the published data after-1992-date and before-2000-date. So, CD-Bonn potential fitted 2932 pp data below $T_{lab} = 350 \ MeV$ available in 2000 with $\chi^2/N_{data} = 1.01$ and the corresponding 3058 np data with $\chi^2/N_{data} = 1.02$.

3.7   Three Body Forces

It is commonly known that non-relativistic calculations, based on purely two-body interactions, fail to reproduce the correct saturation point of symmetric nuclear matter. One of the well known results of several studies, that lasted for about half a century, is the need of introducing three-body forces (TBF's). In our approach the TBF is reduced to a density dependent two-body force by averaging over the position of the third particle, assuming that the probability of having two particles at a given distance is reduced according to the two-body correlation function.

In this work we will illustrate results for two different approaches to the TBF's, i.e. a phenomenological and a microscopic one. The phenomenological approach is based on the so-called Urbana model, which consists of an attractive term due to two-pion exchange with excitation of an intermediate Δ resonance, and a repulsive phenomenological central term. We introduced the same Urbana three-nucleon model within the BHF approach. Those TBF's produce a shift of about $+1$ MeV in energy and -0.01fm^{-3} in density. This adjustment is obtained by tuning the two parameters contained in the TBF's, and was performed to get an optimal saturation point (the minimum).

The connection between two-body and three-body forces within the meson-nucleon theory of nuclear interaction is extensively discussed and developed in Section 3.7.2. At present the theoretical status of microscopically derived TBF's is still quite rudimentary, however a

tentative approach has been proposed using the same meson-exchange parameters as the underlying NN potential.

3.7.1 Phenomenological Three Body Forces

The standard NN interaction [26] models are based, in a more or less direct way, to the meson-nucleon field theory, where the nucleon is considered an unstructured point-like particle. The $Argonne V_{18}$ and the set of Bonn potentials fall in this category. In the one–boson exchange potential ($OBEP$) model one further assumes that no meson-meson interaction is present, and each meson is exchanged in a different interval of time from the others. However, the nucleon is a structured particle, it is a bound state of three quarks with a gluon-mediated interaction, according to Quantum Chromodynamics (QCD). The absorption and emission of mesons can be accompanied by a modification of the nucleon structure in the intermediate states, even in the case of NN scattering processes, in which only nucleonic degrees of freedom are present asymptotically. A way of describing such processes is to introduce the possibility that the nucleon can be excited ("polarized") to other states or resonances. The latter can be the known resonances observed in meson-nucleon scattering. At low enough energy the dominant resonance is the Δ_{33}, which is the lowest in mass. One can then construct NN interaction potentials which explicitly includes these processes, and try to fit again the NN scattering data and deuteron properties. Since the nucleon excitation is a virtual process, i.e. no Δ_{33} is present on shell in the nuclear matter ground state, also in many-body calculations what matters is the effective NN interaction, namely the amplitude for the elementary processes in which both the initial and final states correspond to two nucleons only. This effective interaction is necessarily different for two free nucleons and for two nucleons in the nuclear medium, since the Pauli blocking and the
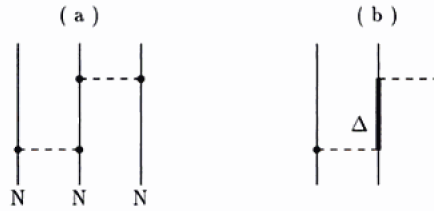
Figure 3.3: The iteration of a two-body force (a). The simplest process involving the Δ resonance (b), which can generate three-body forces.

shifts of the single particle energies affect the intermediate states. This introduces a medium dependence of the NN interaction which is absent in the case of ordinary NN potential without explicit resonances degrees of freedom. This is the simplest in-medium effect due to the non-elementary nature of the nucleons.

If the internal nucleon state can be distorted by the presence of another nucleon, the interaction between two nucleons is surely altered by the presence of a third one. This effect produces clearly a definite three-body force, which is absent if the nucleons are considered unstructured. The simplest of such processes depicted in Fig.3.3(b). Such a process can be interpreted in different but equivalent ways. One way is to view the pion (meson) coming from the first nucleon to polarize the second one, which therefore interacts with a third one as Δ_{33} resonance, surely in a different way than if it had remained a nucleon, like in Fig.3.3(a). The process of Fig.3.3(a) is not indeed a three-nucleon force, but just a repetition of a two-nucleon force. The introduction of a three-nucleon interaction is a consequence of viewing processes like the one of Fig.3.3(b) as an effective interaction among three nucleons, which eventually will be medium-dependent. If the resonance degrees of freedom are explicitly considered, i.e. treated on the same footing as the nucleon ones, than also Fig.3.3(b) corresponds to a repetition of a two-body interaction, and the three-nucleon interaction processes
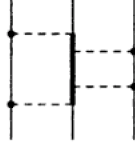
Figure 3.4: A process which is expected to contribute a repulsive three-nucleon force.

are automatically included. A simpler approach has been followed by Urbana group. The main effect of TNF can be schematized by one attractive and one repulsive term, as representative of the whole set of three-nucleon processes.

In particular, the process of Fig.3.4 is repulsive. Actually, once the usual static approximation is made for the nucleons and the resonances, the structure of the different three-body forces turns out to be quite similar. Since the strengths of the different vertex appearing in these diagrams cannot be considered fairly well known, one can treat the strenghts of the two representative terms as free parameters to be fitted to some known physical quantities. The schematic form of the two terms is suggested by their full theoretical expression. More explicitly, the TNF is written as

$$V_{ijk} = V_{ijk}^{2\pi} + V_{ijk}^{R}. \tag{3.33}$$

The two-pion exchange contribution is a cycling sum over the nucleon indices i, j, k of products of anticommutator $\{,\}$ and commutator $[,]$ terms

$$V_{ijk}^{2\pi} = A \sum_{cyc} (\{X_{ij}, X_{jk}\}\{\tau_i \cdot \tau_j, \tau_j \cdot \tau_k\}$$
$$+ \frac{1}{4}[X_{ij}, X_{jk}][\tau_i \cdot \tau_j, \tau_j \cdot \tau_k]), \tag{3.34}$$

where

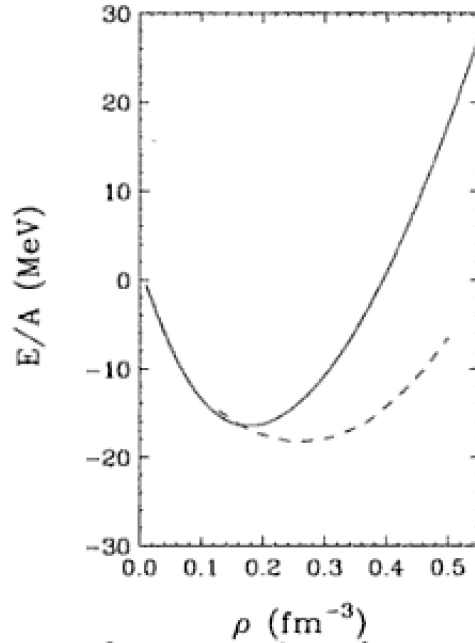$$X_{ij} = Y(r_{ij})\sigma_i \cdot \sigma_j + T(r_{ij})S_{ij} \tag{3.35}$$

Figure 3.5: Saturation curve for symmetric nuclear matter in the Brueckner approximation without (dashed curve) and with (full line) three-body forces.

is the one-pion exchange operator, σ and τ are the Pauli spin and isospin operators, and $S_{ij} = 3[(\sigma_i \cdot r_{ij})[(\sigma_j \cdot r_{ij}) - \sigma_i \sigma_j]$ is the tensor operator. $Y(r)$ and $T(r)$ are the Yukawa and tensor functions, respectively, associated to the one-pion exchange, as in the two-body potential. The repulsive part is taken as

$$V_{ijk} = U \sum_{cyc} T^2(r_{ij}) T^2(r_{jk}). \tag{3.36}$$

The strengths $A(< 0)$ and $U(> 0)$ can be fitted to reproduce the ground state energy of both three nuclon systems (triton and ^{3}He), and the empirical nuclear matter saturation point. Once the fit has been done, the full EOS in a wide density range is obtained. One such a fit, within the Brueckner approximation, is reported in Fig 3.5. Of course, the

higher density region, needed e.g. in neutron star studies, is obtained by extrapolating the TBF from the saturation density region, where they are actually adjusted. This EOS can therefore be inaccurate at the higher densities. The contribution to the EOS of the TNF of Eqs.(3.34) and (3.36) in this Brueckner scheme is treated in an approximate way. Then the lowest order contribution, in the number of hole lines, can be obtained by averaging over the position of one of the particles. In this way one gets an effective two-body interaction, which is of course density dependent. This effective interaction can then be inserted in the usual Brueckner scheme.

3.7.2   Microscopic Three-Body Force

The most extensive study of three-nucleon forces (TNF) has been pursued by Grangè and collaborators [26]. Fig.3.6 indicates some of the processes which can give rise to TNF. Fig.3.6 is a generalization of the process of Fig.3.3(b), where other nucleon resonances (e.g. the Roper resonance) can appear as intermediate virtual excitation and other exchanged mesons can be present. Fig.3.6(b) includes possible non-linear meson-nucleon coupling, as demanded by the chiral symmetry limit. Fig.3.6(c) is the simplest one which includes meson-meson interaction. Other processes of this type are of course possible, which involve other meson-meson couplings, and they should be included in a complete treatment of TNF. Fig.3.6(d) describes the effect of the virtual excitation of a nucleon-antinucleon pair, and it is therefore somehow of different nature from the others. It gives an important (repulsive) contribution and it has been shown to describe the relativistic effect on the EOS to first order in the ratio U/m between the single particle potential and the nucleon rest mass. The σ meson, appearing in some of the diagrams, is a hypothetical scalar meson, believed to be responsible for the intermediate attraction in the two-nucleon interaction. One should
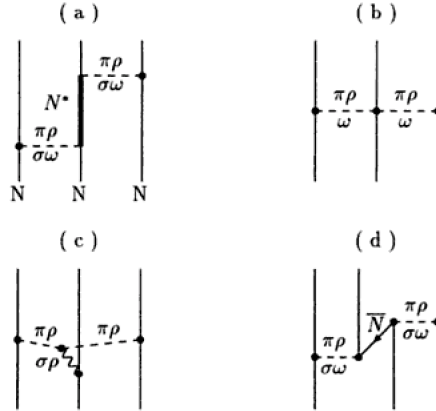
Figure 3.6: Some processes which can contribute to three-nucleon forces.

therefore be careful to be at least consistent between the treatments of the two-nucleon and three-nucleon forces.

The microscopic three-body force adopted in the present calculation is constructed from the meson-exchange current approach.

In the present understanding of the microscopic structure of nuclei, the NN potential originates from the exchange of mesons. In the OBEP approximation, π, ρ, σ and ω mesons are considered. Once the NN potential is determined, i.e. once the meson-nucleon couplings, form factors and meson masses are fixed, many body forces are uniquely fixed as well. The first candidate to 3BF is the well known Fujita-Miyazawa contribution involving a Δ resonance in the intermediate state with 2π exchange.

More recent studies have been concentrated on the general structure of the 2π-3BF within the framework of chiral perturbation theory. While these studies are important in order to settle the 2π-3BF on first principles according to the symmetry properties of QCD, they cannot yet be extended to quantitative investigations of nuclear matter at densities between one to three times normal nuclear matter den-

sity. In this domain indeed, the momenta of the exchanged mesons can be large, and the contribution of heavy mesons (σ and ω) are dominating over the 2π-3BF. More complicated processes could contribute to the 3BF including other nucleonic excitations, but one may expect that the lowest energy excitations, i.e. the isobar $\Delta(1232)$ resonance and the Roper $N^*(1440)$, play the major role in the density domain here considered. The necessary coupling constants σNN^* and ωNN^* are calculated within the relativistic color dielectric model. The form factors at these vertices are also calculated in this model. Note that because of the orthogonality of the radial wave function of the N and N^*, these form factors cannot have the usual dipole parametrization. They are parametrized as follows:

$$F_{MNN^*}(\vec{k}^2) = \frac{\Lambda^2 + \alpha\vec{k}^2}{\Lambda^2 - \alpha m^2}\left(\frac{\Lambda^2 - m^2}{\Lambda^2 + \vec{k}^2}\right)^2 \tag{3.37}$$

Once the dynamical origin of the NN potential is determined from one boson exchange (OBE) mechanisms, all the parameters needed to determine the 3BF are extracted from the NN potential itself. In the case this NN potential is directly parametrized in terms of OBE potentials, like the Bonn potentials, these parameters are given directly from the fit to NN observables, or NN phase shifts. Instead, in the case it is given in terms of a purely numerical parametrization, like the Paris potential or the AV_{18} potential for instance, one has to extract the equivalent OBE parameters by a direct comparison between various spin-isospin potential in the OBE form and in the parametrized form. This procedure was used in order to extract meson exchange parameters from the Paris potential. The π and ρ exchange parameters were determined from the $S = 1$ tensor potential (keeping some of the parameters, like masses and coupling constants, to their physical values), while σ and ω exchange were determined from the central and spin-orbit potentials. In the present calculations, the parameters of the

3BF have been redetermined from the OBE potential model to fulfill the self-consistency with the adopted two-body interaction AV_{18}. It is found that for the σ and ω exchange, the parameters derived from the AV_{18} force remain the same as those given for the Paris potential. While for the π and ρ exchange, the parameters have to be slightly adjusted in order to fit reasonably both the tensor part and the spin-spin part of the AV_{18} potential. As for the σ-meson mass, the value of 540 MeV is still adopted, which has been checked to satisfactorily reproduce the AV_{18} interaction from OBE potential. Varying of the σ-meson mass from 540 MeV to 600 MeV does not change significantly the self-consistency with AV_{18}, so it is also an interesting point to investigate the effect of the σ-meson mass on the nuclear matter EOS.

The effect of the 3BF is included in the self-consistent Brueckner procedure where an effective two-body interaction is constructed without solving the full three-body problem. Starting from the 3BF interaction one defines the effective 2BF as

$$< \vec{r}_1 \vec{r}_2 |V_3| \vec{r}_1' \vec{r}_2' >= \frac{1}{4} Tr \sum_n \int \mathrm{d}\vec{r}_3 \mathrm{d}\vec{r}_3' \phi_n^*(\vec{r}_3')(1 - \eta(r_{13}'))(1 - \eta(r_{23}'))$$

$$\times W_3(\vec{r}_1', \vec{r}_2' \vec{r}_3'|\vec{r}_1 \vec{r}_2 \vec{r}_3)\phi_n(r_3)(1 - \eta(r_{13}))(1 - \eta(r_{23})) \qquad (3.38)$$

where the trace is taken with respect to spin and isospin of the third nucleon. This is nothing else than the average of the three-body force over the wave function of the third particle taking into account via the defect function $\eta(r)$ the correlations between this particle and the two others. The dependence on the defect function entails a selfconsistent determination of the effective 2BF along with the $G-matrix$ and auxiliary potential in that one must recalculate the effective 2BF at each iterative step and then add it to the bare 2BF for the next loop. The $\eta(r)$ is actually the defect function averaged over spin and momenta in the Fermi sea and it incorporates, for the sake of simplicity, only

the most important partial l-wave components the $^1S_0$ and $^3S_1$ partial waves. Corrections due to higher angular momenta in the defect function are expected to be sizeable at high density.

Chapter 4

Results

Contents

4.1 Symmetric Nuclear Matter

In this Section we will focus on a (fairly) good *EoS* for symmetric nuclear matter, that is, when the protons and neutrons have the same number of states, $n_P = n_N$. The total number of states is given by $n = n_N + n_P$. We need to relate the first three nuclear ingredients, n_0, B_E (Binding Energy) and K_0, with the energy density of symmetric nuclear matter, $\epsilon_{(n)}$. The nuclear density is given by $n = n(k_F)$. The energy density also include the nuclear potential, $V(n)$, that will be modeled. The average energy per nucleon, $E/N - m_N$, for the symmetric nuclear matter is a function of n, and has a minimum at $n = n_0$, corresponding to a $B_E = -16 \, MeV$. This minimum is when

$$\frac{d}{dn}\left(\frac{E(n)}{N}\right) = \frac{d}{dn}\left(\frac{\epsilon(n)}{n}\right) = 0, \; for \; n = n_0 \qquad (4.1)$$

This is a limitation for the parameters of $V(n)$. Another, of course, will be given from the binding energy

$$\frac{E}{N} - m_N = BE \; , \; for \; n = n_0 \qquad (4.2)$$

The positive curvature at the end of this valley is linked to the nuclear compressibility for which

$$K(n) = 9\frac{dp(n)}{dn} = 9\left[n^2\frac{d^2}{dn^2}\frac{E(n)}{N} + 2n\frac{d}{dn}\frac{E(n)}{N}\right] \qquad (4.3)$$

at $n = n_0$ this quantity is equal to K_0.

4.2 Asymmetric and β-stable matter

In order to study the structure of neutron stars, we have to calculate the composition and the EOS of cold, neutrino-free, catalyzed matter. We require that the neutron star contains charge neutral matter consisting

of neutrons, protons, and leptons (e^-, μ^-) in beta equilibrium, and compute the EOS for charge neutral and beta-stable matter in the following standard way [27, 28]. The Brueckner calculation yields the energy density of lepton/baryon matter as a function of the different partial densities,

$$\epsilon(\rho_n, \rho_p, \rho_e, \rho_\mu) = (\rho_n m_n + \rho_p m_p) + (\rho_n + \rho_p)\frac{E}{A}(\rho_n, \rho_p)$$

$$+\rho_\mu m_\mu + \frac{1}{2m_\mu}\frac{(3\pi^2 \rho_\mu)^{5/3}}{5\pi^2} + \frac{(3\pi^2 \rho_e)^{4/3}}{4\pi^2} \tag{4.4}$$

where we have used ultrarelativistic and nonrelativistic approximations for the energy densities of electrons and muons, respectively. In practice, it is sufficient to compute only the binding energy of symmetric nuclear matter and pure neutron matter, since within the BHF approach it has been verified that a parabolic approximation for the binding energy of nuclear matter with arbitrary proton fraction $x = \rho_p/\rho$, $\rho = \rho_n + \rho_p$, is well fulfilled,

$$\frac{E}{A}(\rho, x) \approx \frac{E}{A}(\rho, x = 0.5) + (1 - 2x)^2 E_{\text{sym}}(\rho)\,, \tag{4.5}$$

where the symmetry energy E_{sym} can be expressed in terms of the difference of the energy per particle between pure neutron ($x = 0$) and symmetric ($x = 0.5$) matter:

$$E_{\text{sym}}(\rho) = -\frac{1}{4}\frac{\partial(E/A)}{\partial x}(\rho, 0) \approx \frac{E}{A}(\rho, 0) - \frac{E}{A}(\rho, 0.5)\,. \tag{4.6}$$

Knowing the energy density the various chemical potentials (of the species $i = n, p, e, \mu$) can be computed straightforwardly,

$$\mu_i = \frac{\partial\epsilon}{\partial\rho_i}\,, \tag{4.7}$$

and the equations for beta-equilibrium,

$$\mu_i = b_i \mu_n - q_i \mu_e\,, \tag{4.8}$$

(b_i and q_i denoting baryon number and charge of species i) and charge neutrality,

$$\sum_i \rho_i q_i = 0 \,. \tag{4.9}$$

This allows to determine the equilibrium composition $\rho_i(\rho)$ at given baryon density ρ and finally the EOS,

$$P(\rho) = \rho^2 \frac{d}{d\rho} \frac{\epsilon(\rho_i(\rho))}{\rho} = \rho \frac{d\epsilon}{d\rho} - \epsilon = \rho \mu_n - \epsilon \,. \tag{4.10}$$

4.3 Heavy ions phenomenology

In the last two decades intensive studies of heavy ion reactions at energies ranging from few tens to several hundreds MeV/A have been performed. The main goal has been the extraction from the data of the gross properties of the nuclear EoS. It can be expected that in heavy ion collisions at large enough energy nuclear matter is compressed and that, at the same time, the two partners of the collisions produce flows of matter. In principle the dynamics of the collisions should be connected with the properties of the nuclear medium EoS and its viscosity. In the so called "multifragmentation" regime, after the collision numerous nucleons and fragments of different sizes are emitted, and the transverse flow, which is strongly affected by the matter compression during the collision, can be measured. Based on numerical simulations, in [29] a phenomenological range of densities was proposed where any reasonable EoS for symmetric nuclear matter should pass through in the pressure vs. density plane. The plot is reproduced in Fig.4.1.

The green dashed box represents the results of the numerical simulations of the experimental data discussed in [29], and the brown filled region represents the experimental data on kaons production, [30]. We notice that the EoS calculated with the BHF and the variational methods including UVIX three-body forces look in agreement with the data
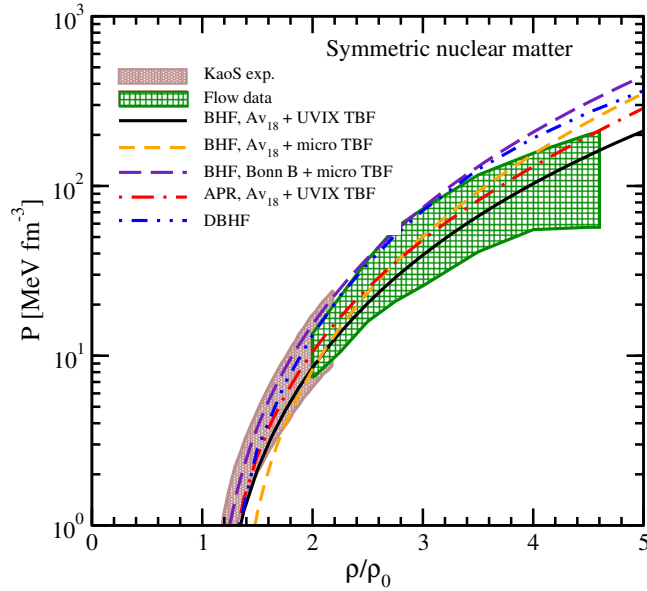
Figure 4.1: Pressure as a function of baryon density for symmetric nuclear matter. See text for details.

in the full density range. On the other hand, the BHF EoS obtained using microscopic TBF's are only marginally compatible with the experimental data, as well as the DBHF EoS, showing that they are too repulsive already at density $\rho \geq 3\rho_0$ if the Bonn potentials are used. Though, it has to be stressed that all EoS are compatible with the data around the saturation density, i.e. their incompressibility is as soft as required by the data. However, the values of the incompressibility do not characterize completely the EoS, since it is density dependent, but in any case the analysis indicates that the EoS at low density must be soft.

A further constraint on the EoS is given by the symmetry energy which has been extensively studied both from the theoretical and experimental point of view in [31]. The symmetry energy is displayed in Fig.4.2 as a function of the nucleon density. The purple region is the result of a recent analysis performed by P. Danielewicz on the isobaric

analog states (IAS) in nuclei [32]. This stems from the charge independence of nuclear interactions, i.e. strong interactions among nucleons in the same state do not depend on whether the nucleons are protons or neutrons. Therefore the energy difference between the ground state of a nucleus with $N > Z$ and the isobaric analogs of the ground states of neighboring isobars are given by the symmetry energy, and the Coulomb contributions to the binding energy can be determined using the IAS. Many such states have been identified, and by fitting the available data on the IAS, Danielewicz and Lee obtained the constraint shown as a purple region in Fig.4.2. We observe that all EoS give results in very good agreement with the experimental data, except the ones of BHF with microscopic TBF at densities below the saturation density. In Fig.4.3 we display the slope L as a function of the symmetry energy at saturation density. Several experimental data are displayed. The blue band represents experimental data from HIC, obtained from the neutron and proton spectra from central collisions for ^{124}Sn$+^{124}$Sn and ^{112}Sn$+^{112}$Sn reactions at 50 MeV/A [33]. At the same incident energy, isospin diffusion was investigated. We remind that isospin diffusion in HIC depends on the different N/Z asymmetry of the involved projectiles and targets, hence it is used to probe the symmetry energy [34, 35]. The full red circle shows the results from isospin diffusion observables measured for collisions at a lower beam energy of 35 MeV per nucleon [36]. Transverse collective flows of hydrogen and helium isotopes as well as intermediate mass fragments with $Z < 9$ have also been measured at incident energy of 35 MeV/A in ^{70}Zn$+^{70}$Zn , ^{64}Zn$+^{64}$Zn, ^{64}Ni$+^{64}$Ni reactions and compared to transport calculations. The analysis yielded values denoted by the full squares [37].

The box labelled by FRDM (finite-range droplet model) represents a refinement of the droplet model [38], and includes microscopic "shell" effects and the extra binding associated with $N = Z$ nuclei. The FRDM
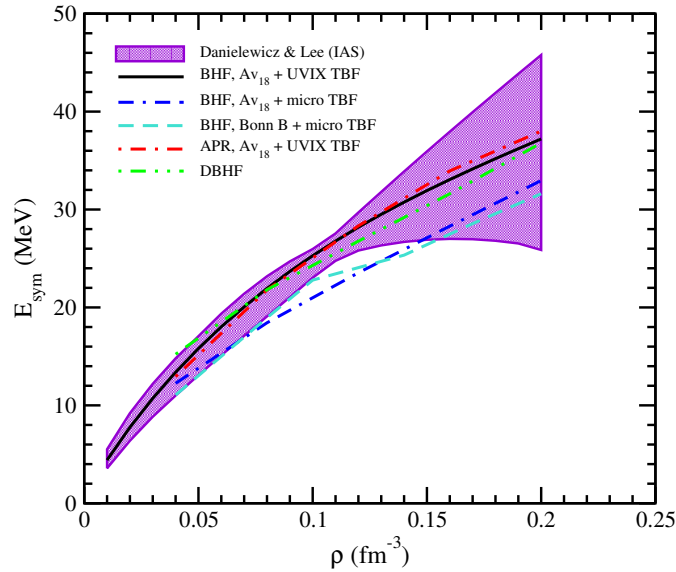
Figure 4.2: The symmetry energy is displayed as a function of the nucleon density. The purple zone represents the recent data by P. Danielewicz [32], whereas the different curves are the results of the microscopic many-body methods.

reproduces nuclear binding energies of known nuclei within 0.1%, and allows determination of both $S_0 = 32.5 \pm 0.5$ MeV and $L = 70 \pm 15$ MeV.

In Fig.4.3 the other boxes represent experimental data obtained from measurements of the neutron skin thickness. In light nuclei with $N \approx Z$, the neutrons and protons have similar density distributions. With increasing the neutron number N, the radius of the neutron density distribution becomes larger than that of the protons, reflecting the pressure of the symmetry energy. The measurement of the neutron skin thickness is made on the stable nucleus ^{208}Pb, which has a closed neutron shell with $N = 126$ and a closed proton shell with $Z = 82$, hence it is very asymmetric and the neutron skin is very thick. The possibility of measurements of the neutron radius in ^{208}Pb by the experiment PREX at Jefferson Laboratory has been widely discussed in [39, 40].
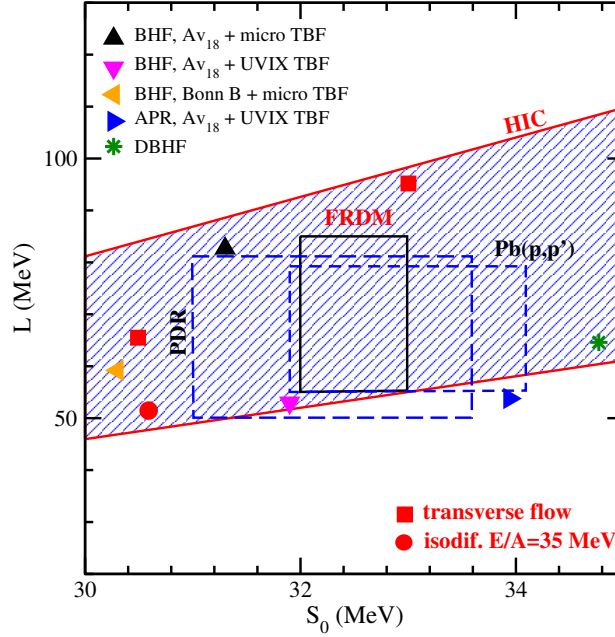
Figure 4.3: The derivative of the symmetry energy L is shown as a function of the symmetry energy at saturation S_0. See text for details.

The experiment $PREX$ should extract the value of the neutron radius in ^{208}Pb from parity-violating electron scattering. However, the experimental signature is very small, and the extracted thickness has a large statistical uncertainty. In the next few years, a second experimental run for PREX could reduce this large uncertainty [41].

Recent experimental data obtained by Zenihiro et al. [42] on the neutron skin thickness of ^{208}Pb deduced a value $\delta R_{np} = 0.211^{+0.054}_{-0.063}$ fm. From the experiments constraints on the symmetry energy were derived, and these are plotted in Fig.4.3 as the short-dashed blue rectangular box labelled Pb$(\vec{p}, \vec{p})$.

Last, we mention the experimental data on the Pygmy Dipole Resonance (PDR) in very neutron-rich nuclei such as ^{68}Ni and ^{132}Sn, which peaks at excitation energies well below the Giant Dipole Resonance (GDR), and exhausts about 5% of the energy-weighted sum rule [43].
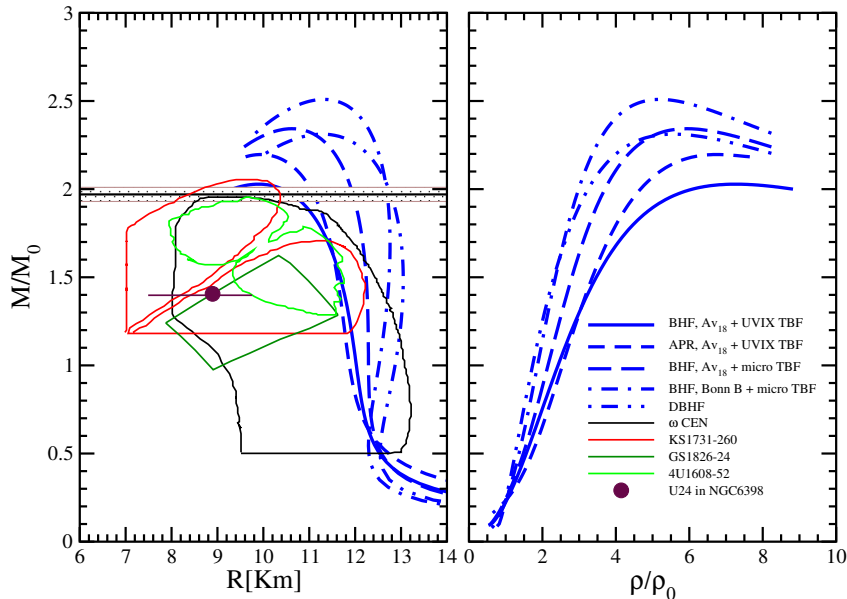
Figure 4.4: The mass-radius (left panel) and the mass-central density (right panel) relations are plotted for the EoS's discussed. Boxes are boundaries extracted from observations.

In many models it has been found that this percentage is linearly dependent on the slope L of the symmetry energy. Carbone et al [44] extracted a value of $L = 64.8 \pm 15.7$ MeV, and $S_0 = 32.2 \pm 1.3$ MeV using various models which connect L with the neutron skin thickness. Those constraints are shown as a long-dashed rectangle in Fig.4.3 with the label PDR.

The predictions of the different EoS are also reported in Fig.4.3 as full symbols. They are distributed within a large region and they span a wide interval in the values of the parameter L. However, the various phenomenological data are at best marginally compatible, and it is difficult to put well definite constraints on the EoS. Tentatively, from these data one can restrict the possible values of the symmetry energy at saturation in a limited interval, approximately $30 < S_0 < 35$ MeV, where all the considered EoS are actually falling.
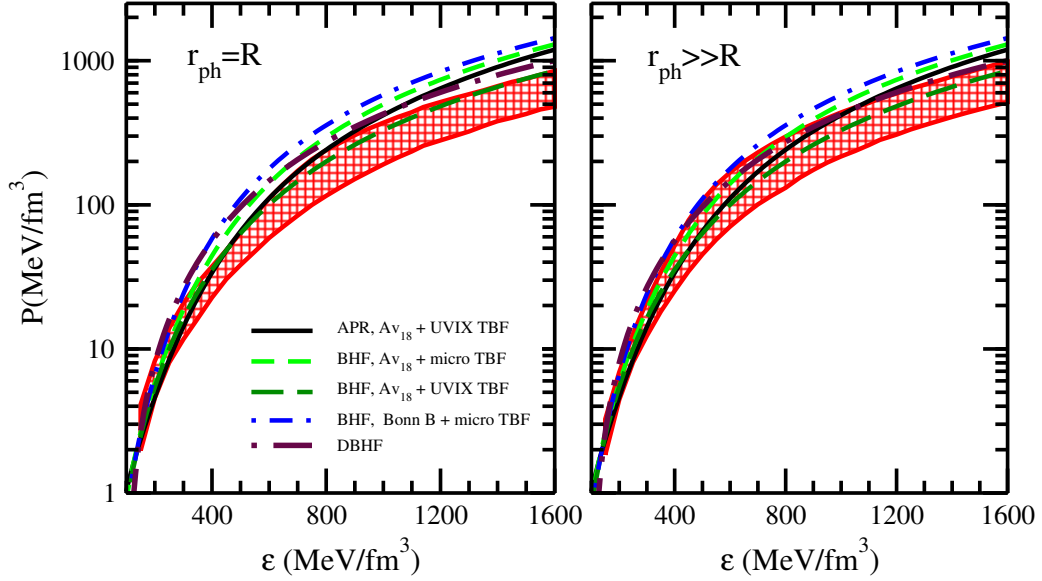
Figure 4.5: Pressure as a function of the mass-energy density in neutron star matter. See text for details.

4.4   Astrophysics

A neutron star is bound by gravity, and it is kept in hydrostatic equilibrium only by the pressure produced by the compressed nuclear matter. It is then apparent that the nuclear matter EoS is the main medium property that is relevant in this case, as can be seen in the celebrated Tolman-Oppenheimer-Volkoff [28] equations, valid for spherically symmetric NS

$$\frac{dP}{dr} = -G\frac{\epsilon m}{r^2}\left(1 + \frac{P}{\epsilon}\right)\left(1 + \frac{4\pi P r^3}{m}\right)\left(1 - \frac{Gm}{r}\right)^{-1},$$

$$\frac{dm}{dr} = 4\pi r^2 \epsilon \tag{4.11}$$

where G is the gravitational constant, P the pressure, ε the energy density, and r the (relativistic) radius coordinate. To close the equations we need the relation between pressure and density, $P = P(\varepsilon)$,

i.e. just the EoS. Integrating these equations one gets the mass and radius of the star for each central density. Typical values are 1-2 solar masses ($M_\odot$) and about 10 Km, respectively. This indicates the extremely high density of the object. It turns out that the mass of the NS has a maximum value as a function of radius (or central density), above which the star is unstable against collapse to a black hole. The value of the maximum mass depends on the nuclear EoS, so that the observation of a mass higher than the maximum one allowed by a given EoS simply rules out that EoS. The considered microscopic EoS's are compatible with the largest mass observed up to now, that is close to 1.97 ± 0.04 $M_\odot$ [5]. This is clearly shown in Fig.4.4, where the mass-radius (left panel) and mass-central density relations (right panel) are plotted for all the considered EoS's as thick lines. It looks unlikely that this value is indeed the largest possible NS mass, and therefore future observational data on NS masses could overcome this limit and strongly constrain the nuclear EoS.

It would be of course desirable to have some phenomenological data also on the radius of NS. In Fig.4.4 a sample of observational data taken from [45] is displayed by closed thin lines for different sources, measured in quiescence and from thermonuclear bursts. It turns out that the current measurements are consistent with radii in the range 8-12 km and disfavor neutron stars with R ∼15 km. Those measurements are consistent with the recent observation of the neutron star in SAX J1748.9-2021, which points to the neutron star radius in the 8-11 km range [46].

Additional tentative constraints on the nuclear EoS were obtained in a recent analysis of the data on six NS based on Bayesian statistical framework [47]. Depending on the hypothesis made on the structure of the NS, the results are slightly different, as shown in Fig.4.5, where the quantity r_{ph} is the photosphere radius. In the left panel r_{ph} is
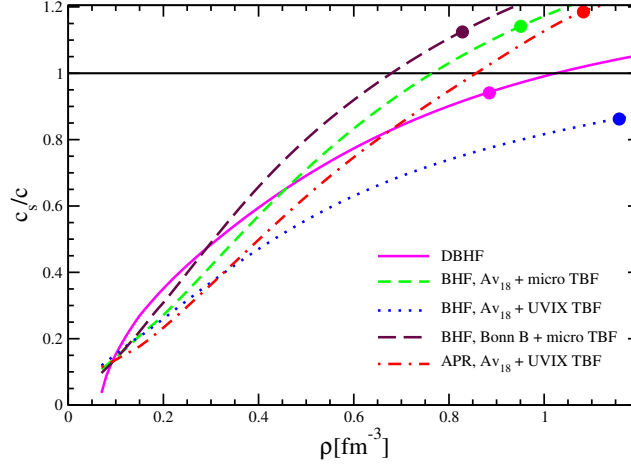
Figure 4.6: The speed of sound is plotted as function of the nucleon density for the EoS's discussed in the text. The dots mark the central density for the maximum mass of a neutron star.

comparable to the neutron star radius R, whereas in the right panel a substantial expansion of the photosphere during an X-ray burst is assumed to occur. The overall allowed region where the EoS's should lie is displayed in Fig.4.5 as bounding boxes, where the theoretical EoS's just discussed are also reported as thick lines. Among the different EoS's, only the one calculated with BHF and phenomenological Urbana model appear to be compatible with the extracted observational constraints over the whole density range. It turns out that other microscopic EoS do not show the same agreement, in particular the EoS with BHF and microscopic TBF and the DBHF EoS look too repulsive at high density. These boundaries obtained from astrophysical data are complementary to the ones obtained from heavy ion reactions, and illustrated in the previous subsection. In fact, in heavy ion collisions the tested matter is essentially symmetric, while in NS the matter is highly asymmetric. Considered together, the two types of constraints probe the density dependence of the symmetry energy.

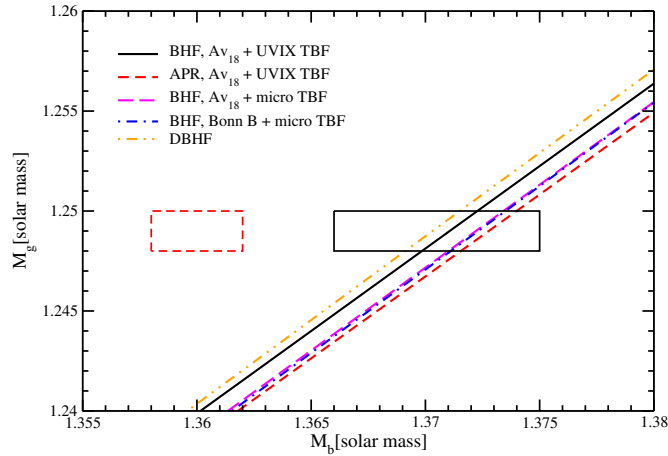In relation to the high density region of the nuclear EoS, an addi-

Figure 4.7: The gravitational mass is plotted as a function of the baryon mass for the EoS's discussed in the text. The boxes indicate the boundaries coming from the simulations.

tional test is on the speed of sound c_S, that is required to be smaller than the speed of light c (causality condition). The speed of sound is directly connected with the incompressibility and the energy density, according to the relativistic expression

$$\frac{c_S}{c} = \sqrt{\frac{dP}{d\epsilon}} \qquad (4.12)$$

As such, it depends on the matter energy density and asymmetry. In Fig.4.6 we plot the speed of sound in units of c as a function of the density of the NS matter, according to each EoS. In the figure the full points on each curve indicate the central density of the calculated NS maximum mass for the given EoS. At large enough density most of the EoS's show a superluminal speed of sound. One finds that also the DBHF EoS shows a superluminal behaviour. This is not completely surprising, since the DBHF approach is actually based on the three-dimensional reduction of the original four-dimensional Bethe-Salpeter equation, and therefore it is not fully relativistic.

A further additional constraint on the neutron star EoS is provided

by the observation of the double pulsar J0737-3039, and the interpretation given by Podsiadlowski, [48]. In fact, the gravitational mass of Pulsar B is very precisely known $M_G = 1.249 \pm 0.001\,M_\odot$, whereas estimates of the baryonic mass depend upon its detailed mode of formation. As modelled by Podsiadlowski et al., if the pulsar B was formed from a white dwarf with an O-Ne-Mg core in an electron-capture supernova, assuming no or negligible loss of baryonic mass during the collapse, the newly born neutron star will have the same baryonic mass as the precollapse core of the progenitor star, i.e. $M_B \simeq 1.366 - 1.375\,M_\odot$. This result is displayed in Fig.4.7 as a black box. Though, taking into account the uncertainty in the EoS and the small mass loss during the collapse, Kitaura et al. [49] made another simulation which gave $M_B = 1.360 \pm 0.002\,M_\odot$, which is shown in Fig.4.7 by the dashed red box. We have calculated for each neutron star matter EoS the relation between the gravitational and baryonic mass, and these are displayed in Fig.4.7 by the straight curves. We notice that the results of all microscopic EoS's agree very well with the result of Podsiadlowski, at variance with the calculations based on the phenomenological Skyrme forces discussed in [50], where agreement was found with the result of Kitaura et al. [49], which assumed small mass loss during the collapse.

Chapter 5

Cooling and Results

Contents

Cooling simulations [51], confronted with soft X-ray, extreme UV, UV and optical observations of the thermal photon flux emitted from the surfaces of neutron stars, provide most valuable information about the physical processes operating in the interior of these objects. The predominant cooling mechanism of hot (temperatures $T \geq 10^{10} K$) newly formed neutron stars is neutrino emission, with an initial cooling time scale of seconds. Neutrino cooling still dominates for at least the first thousand years, and typically for much longer in slow (standard) cooling scenarios. Photon emission eventually overtakes neutrinos when the internal temperature has sufficiently dropped. Being sensitive to the adopted nuclear equation of state (EOS), the stellar mass, the assumed magnetic field strength, superfluidity, meson condensates, and the possible presence of color-superconducting quark matter, theoretical cooling calculations serve as a principal window on the properties of super-dense hadronic matter and neutron star structure. The thermal evolution of neutron stars also yields information about such temperature-sensitive properties as transport coefficients, crust solidification, and internal pulsar heating mechanisms. The basic features of the cooling of a neutron star are easily grasped by simply considering the energy conservation equation for the star. In its Newtonian formulation this equation reads

$$\frac{dE_{th}}{dt} = C_v \frac{dT}{dt} = -L_\nu - L_\gamma + H \qquad (5.1)$$

where E_{th} is the thermal energy content of the star, T its internal temperature, and C_v its total specific heat. The energy sinks are the total neutrino luminosity L_ν and the surface photon luminosity L_γ. The source term H includes all possible "heating mechanisms" which, for instance, convert magnetic or rotational energy into heat. The dominant contributions to C_v come from the core, constituting more than 90% of the total volume, whose constituents are quantum liquids of leptons,

baryons, mesons, and possibly deconfined quarks at the highest densities. When baryons, and quarks, become paired their contribution to C_v is strongly suppressed at temperatures $T \ll T_c$ (T_c being the corresponding critical temperature). The crustal contribution is in principle dominated by the free neutrons of the inner crust but, since these are certainly extensively paired, practically only the nuclear lattice and electrons contribute.

5.1 URCA Processes

As already mentioned in the introduction, neutron stars are born with temperatures in excess of $10^{10}K$. The dominating cooling mechanism of such objects for the first several thousand years after birth is neutrino emission from the interior. The most important effect on stellar cooling is due to the $URCA$ processes. After this time, cooling via photon emission from the star's surface takes over. The process was first discussed by George Gamow and Mário Schenberg while they were visiting a Casino named *Cassino da Urca* in Rio de Janeiro. Schoenberg is reported to have said to Gamow that "the energy disappears in the nucleus of the supernova as quickly as the money disappeared at that roulette table". Moreover in Gamow's South Russian dialect, "urca" can also mean a "robber" [52]. In Tab. 5.1 we summarize the dominant neutrino emitting processes together with their efficiency for neutron star cooling and we now briefly describe the most important ones.

Direct Urca Processes.

The beta decay and electron capture processes among nucleons, $n \rightarrow p + e^- + \bar{\nu}_e$ e and $p + e^- \rightarrow n + \nu_e$, also known as nucleon direct Urca process (or cycle), are only possible in neutron stars if the proton fraction exceeds a critical threshold. Otherwise energy and momentum

can not be conserved simultaneously for these reactions. For a neutron star made up of only neutrons, protons and electrons, the critical proton fraction is around 11%. This follows readily from $\mathbf{k_{F_n}} = \mathbf{k_{F_p}} + \mathbf{k_{F_e}}$ combined with the condition of electric charge neutrality of neutron star matter. The triangle inequality then requires for the magnitudes of the particle momenta $k_{F_n} \leq k_{F_p} + k_{F_e}$, and charge neutrality constrains the particle Fermi momenta according to $k_{F_p} = k_{F_e}$. Substituting $k_{F_p} = k_{F_e}$ into the triangle inequality leads to $k_{F_n} \leq 2k_{F_p}$ so that $n_n \leq 8n_p$ for the number densities of neutrons and protons. Expressed as a fraction of the system's total baryon number density, $n = n_p + n_n$, one thus arrives at $n_p/n < 1/9 \approx 0.11$ as quoted above.

Medium effects and interactions among the particles modify this value only slightly but the presence of muons raise it to about 0.15. Hyperons, which may exist in neutron star matter rather abundantly, produce neutrinos via the direct Urca process $\Sigma^- \rightarrow \Lambda + e^- + \bar{\nu}_e$ with $\Lambda^- + e^- \rightarrow \Sigma^- + \nu_e$ and similar ones involving hyperons and nucleons simultaneously. The cooling driven by the nucleon direct Urca, however, dominates over the energy loss produced by the direct Urca process among hyperons.

Modified Urca Processes. In absence of hyperons or meson condensates, or in case the proton fraction is below threshold, none of the above described Urca processes is possible. In this case, the dominant neutrino emission process is a second order process, variant of the direct Urca process, called modified Urca process, in which a bystander neutron or proton participates to allow momentum conservation (see Table 5.1). Since this modified Urca process involves 5 degenerate fermions, instead of three for the direct Urca and meson Urca processes, its efficiency is reduced, simply by phase space limitation, by a factor of order $(T/T_F)^2$. This reduction, for $T_F \approx 100 MeV$ and $T = 0.1\ MeV = 10^9\ K$, amounts to about 6 order of magnitude (!) and

Name	Process[c]	Emissivity[d] (erg cm^{-3} s^{-1})	
Modified Urca cycle (neutron branch)	$n + n \rightarrow n + p + e^- + \bar{\nu}_e$ $n + p + e^- \rightarrow n + n + \nu_e$	$\sim 2 \times 10^{21} \, R \, T_9^8$	Slow
Modified Urca cycle (proton branch)	$p + n \rightarrow p + p + e^- + \bar{\nu}_e$ $p + p + e^- \rightarrow p + n + \nu_e$	$\sim 10^{21} \, R \, T_9^8$	Slow
Bremsstrahlung	$n + n \rightarrow n + n + \nu + \bar{\nu}$ $n + p \rightarrow n + p + \nu + \bar{\nu}$ $p + p \rightarrow p + p + \nu + \bar{\nu}$	$\sim 10^{19} \, R \, T_9^8$	Slow
Cooper pair formations	$n + n \rightarrow [nn] + \nu + \bar{\nu}$ $p + p \rightarrow [pp] + \nu + \bar{\nu}$	$\sim 5 \times 10^{21} \, R \, T_9^7$ $\sim 5 \times 10^{19} \, R \, T_9^7$	Slow
Direct Urca cycle	$n \rightarrow p + e^- + \bar{\nu}_e$ $p + e^- \rightarrow n + \nu_e$	$\sim 10^{27} \, R \, T_9^6$	Fast
π^- condensate	$n + <\pi^-> \rightarrow n + e^- + \bar{\nu}_e$	$\sim 10^{26} \, R \, T_9^6$	Fast
K^- condensate	$n + <K^-> \rightarrow n + e^- + \bar{\nu}_e$	$\sim 10^{25} \, R \, T_9^6$	Fast

Table 5.1: Dominant neutrino emitting processes in neutron star cores, in absence of hyperonsa and quarks.

an overall temperature dependence T^8 instead of T^6. It is certainly the dominant process for not to high densities in absence of pairing, and is the essence of the old "Standard Cooling Scenario" (namely the scenario where we exclude Direct Urca Process). However, in presence of pairing, neutrino emission by the constant formation of Cooper pairs most probably dominates over the modified Urca process. Since the modified Urca process involves a strong interaction for the momentum exchange between the neutrino emitting nucleon and the bystander one, it is prone to medium corrections which seem to result in a reduction of emissivity. However, softening of the pion mode, which eventually leads to π-condensation, do results in a very strong enhancement of the emissivity when the density approaches n_{cr}^π, and gives a smooth transition from the modified Urca process toward the π-condensate process

through a medium-modified-Urca process ("MMU" process).

5.2 Pairing

Pairing will unavoidably occur in a degenerate Fermi system in case there is any attractive interaction between the particles. In case of the baryons, and quarks, in the neutron star interior there are many candidates for channels of attractive interactions, and the real question is rather what is the critical temperature T_c at which pairing occurs. Calculation of T_c are notoriously difficult and results often highly uncertain. With respect to leptons, there is no obvious attractive interaction which could lead to pairing with a T_c of significant value.

In the case of nucleons, at low Fermi momenta, pairing is predicted to occur in the $^1S_0$ angular momentum state while at larger momenta neutrons are possibly paired in the $^3P_2 - ^3F_2$ state (the mixing being due to the tensor interaction). In the case of the neutron $^1S_0$ pairing, which occurs at densities corresponding to the crust and, possibly, the outermost part of the core, much efforts have been invested in its study and calculations are converging with time when more and more sophisticated many-body models are used. In the case of the proton $^1S_0$ pairing the situation is more delicate since it occurs at densities (in the outer core) where protons are mixed, to a small amount, with neutrons. Predictions for T_c span a much wider range than in the case of the neutron $^1S_0$ gap. Whether or not neutrons pair in the $^3P_2 - ^3F_2$ channel is still uncertain, since even the best available models for the nucleon-nucleon interaction fail to reproduce the measured $^3P_2$ phase shift *in vacuum.*

The enormous impact of pairing on the cooling comes directly from the appearance of the energy gap Δ at the Fermi surface which leads to a suppression of all processes involving single particle excitations of
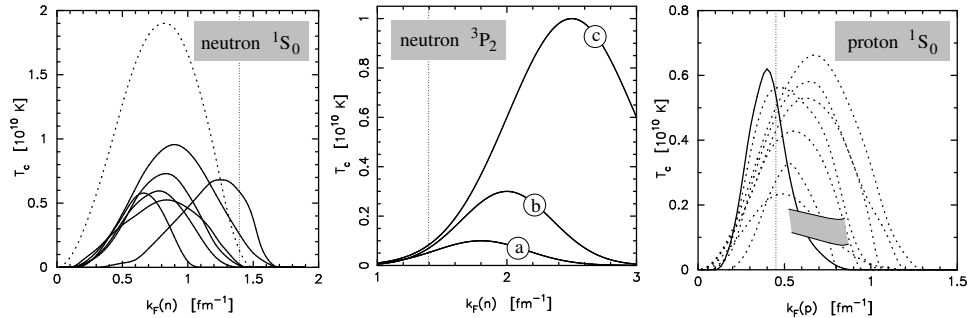
Figure 5.1: Predictions for the nucleon pairing T_c. Left panel: neutron $^1S_0$ pairing; all calculations include medium polarization in some measure except for the dotted curve which illustrates the strong reduction effect of polarization on this gap. Right panel: same for protons; no polarization effects are taken into account except for the continuous curve; the shaded area shows the range of expected T_c's when polarization is taken into account. Central panel: neutron $^3P_2$ pairing, three typical results illustrating the possible range.

the paired species. When $T \ll T_c$ the suppression is of the order of $e^{-\Delta/k_B T}$ and hence dramatic. The suppression depends on the temperature dependence of Δ and the details of the phase space involved in each specific process. In numerical calculations it is introduced as a control function. For the specific heat one has

$$c_v(T) \longrightarrow c_v^{paired}(T) = R_c(T/T_c) \times c_v^{normal}(T), \qquad (5.2)$$

and the control functions have been calculated for both $^1S_0$ and $^3P_2$ pairing. For neutrino processes there is a long family of control functions for all processes which must also consider which of the participating baryons are paired. As for c_v one uses

$$\epsilon_\nu^{paired}(T) = R_\nu(T/T_c) \times \epsilon_\nu^{normal}(T), \qquad (5.3)$$

We plot in Fig. 5.2 several examples of control functions. It is important to notice that the gap Δ is actually a function of the particle momentum, $\Delta = \Delta(k)$. For $^1S_0$ pairing it is isotropic, i.e., $\Delta = \Delta(k)$, but for
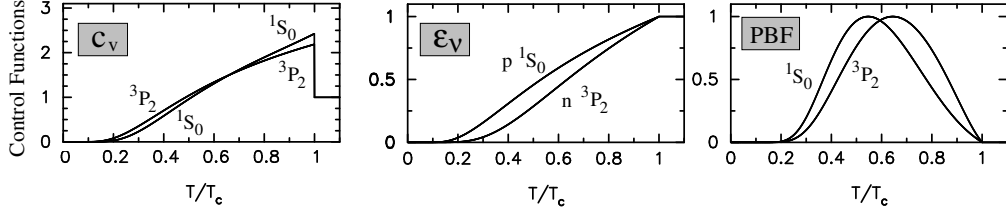
Figure 5.2: Control functions for c_ν, ϵ_ν and the PBF process.

$^3P_2 - {}^3F_2$ pairing the angular dependence of $\Delta(k)$ is complicated. In this latter case many phases, with distinct angular dependences of $\Delta(k)$ are possible and for several of them $\Delta(k)$ has nodes at some points of along some lines on the Fermi surface. The control functions plotted in Figure 5.2 assume nodeless gaps, but in cases of 1D nodes $R \sim (T/T_c)^2$, while for 2D nodes $R \sim T/T_c$, at $T \ll T_c$ instead of a Boltzmann-like suppression.

Cooper Pair Breaking and Formation (PBF) Processes. Besides the above described, and well known, suppressing effects on the specific heat and neutrino emissivities, the onset of pairing also opens new channels for neutrino emission. The superfluid or superconducting condensate is in thermal equilibrium with the single particle ("broken pairs") excitations and there is continuous formation and breaking of Cooper pairs, which are very intense at temperatures slightly below T_c. The formation of a Cooper pair liberates an energy which can be taken away by a ν-$\bar\nu$ pair

$$X + X \longrightarrow [XX] + \nu + \bar\nu \tag{5.4}$$
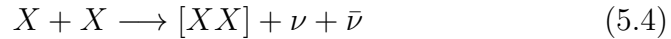
where $[XX]$ denotes a Cooper pair of particles X (X stands for neutrons, protons, hyperons, quarks, etc.). As an example, the emissivity for neutron $^3P_2$ pairing is

$$q_\nu^{n,\,^3P_2} = 8.6 \times 10^{21} \left(\frac{n_b}{n_0}\right)^{1/3} \left(\frac{m_n^*}{m_n}\right) \times \tilde{R}_{^3P_2}(T/T_c) \left(\frac{T}{10^9\ K}\right)^7,$$

where the control function $\tilde{R}$ is plotted in the right panel of Fig. 5.2: the process turns on at $T = T_c$, with an increasing efficiency when T decreases, since the energy of the emitted neutrinos is determined by the gap's size which grows with decreasing temperature just below T_c, and is eventually exponentially suppressed when $T \ll T_c$ as pair breaking is frozen because $k_B T \ll \Delta$. This process can be seen as a bremsstrahlung with a very strong correlation in the final state and referring to Tables 5.1 one sees that it is much more efficient that the simple bremsstrahlung one and it can even dominate over the standard modified Urca process.

5.2.1 The Surface Photon Luminosity and the Envelope

The photon luminosity L_γ is traditionally expressed as

$$L_\gamma = 4\pi R^2 \cdot \sigma_{SB} T_e^4 , \tag{5.5}$$

which *defines* the effective temperature T_e (σ_{SB} being the $Stefan-Boltzmann$ constant and R the stellar radius). The quantities L, R, and T_e are local quantities as measured by an observer at the stellar surface. An external observer "at infinity" will measure these quantities red-shifted, i.e., $L_\infty = e^{2\phi} L_\gamma$, $T_\infty = e^\phi T_e$, and $R_\infty = e^{-\phi} R$, where $e^{2\phi} \equiv g_{00}$ is the time component of the metric and is related to the red-shift z by $e^{-\phi} = 1 + z$, so that

$$L_\infty = 4\pi R_\infty^2 \cdot \sigma_{SB} T_\infty^4 . \tag{5.6}$$

The luminosity L_γ, or L_∞, is the main output of a cooling calculation, and it can equally well be expressed in terms of T_e or T_∞. Numerical simulations calculate the time evolution of the internal temperature $T = T(\rho, t)$ and luminosity $L = L(\rho, t)$ profiles (viewed as functions of the density ρ instead of the radius r) up to an outer boundary ρ_b. This

boundary is chosen such that at this point the diffusive luminosity $L(\rho_b)$ is equal to the photon luminosity at the surface, i.e., $L(\rho_b) \equiv L_\gamma$, and an envelope model is glued as an outer boundary condition. Typically ρ_b is taken as 10^{10} g cm^{-3} and the envelope is thus a thin layer, of the order of a hundred meters thick, which is treated in the plane parallel approximation. Assuming that the thermal relaxation time-scale of the envelope is much shorter than the stellar evolution time-scale, and that neutrino emission in the envelope is negligible, hydrostatic equilibrium and heat transport reduce to ordinary differential equations which, with the appropriate physical input, are easily solved. The result is a surface temperature $T_s \equiv T_e$ for each given $T_b \equiv T(\rho_b)$. It is usually called a $T_b - T_s$ or $T_b - T_e$ relationship. Through Eq. (5.5), this gives us a relationship between $L(\rho_b) \equiv L_\gamma$ and $T(\rho_b)$ which is the outer boundary condition for the cooling code. T_e is actually controlled by a "sensitivity layer", where electrons become partially degenerate and ions are in the liquid phase. At higher densities the highly degenerate electrons are extremely efficient in transporting heat while at lower densities photons take over and are also very efficient. The density at which the sensitivity layer is located increases with increasing T_b. This sensitivity layer is hence a throttle and once heat has passed through it, it can freely flow to the surface and be radiated. The layers at densities below the sensitivity layer have no effect at all on the thermal evolution of the star, since they are unable to alter the heat flow, but the outermost layer, the photosphere, is of course of upmost observational importance since it is there that the energy distribution of the emerging flux, i.e., the observable spectrum, is determined. Gluing an envelope to an interior solution is a standard technique in stellar evolution codes. For neutron stars it has two extra advantages: it relieves us from solving for hydrostatic equilibrium in the interior, since matter there is degenerate, and, most importantly, it allows us to easily include magnetic field

effects. The magnetic field slightly enhances heat transport along it but strongly suppresses it in the perpendicular direction, resulting in a highly non uniform surface temperature. Assuming that magnetic field effects on heat transport are negligible at $\rho > \rho_b$ one keeps spherical symmetry in the interior and thus has a unique T_b at ρ_b. For this given uniform T_b one can piece together a set of envelope calculations for the various field strengths and orientations along the stellar surface, corresponding to the assumed magnetic field structure, and thus obtain a non uniform surface temperature distribution $T_s(\theta, \phi)$, in spherical coordinates (θ, ϕ). The effective temperature is simply obtained by averaging the locally emerging photon flux $F_\gamma(\theta, \phi) \equiv \sigma_{SB} T_s^4(\theta, \phi)$ over the whole stellar surface

$$T_e^4 \equiv \frac{1}{4\pi} \int\int T_s^4(\theta, \phi) \, \sin\theta \, d\theta d\phi \qquad (5.7)$$

Two examples of such temperature distributions are illustrated in Fig.5.3. The overall effect on T_e is nevertheless surprisingly small see the examples in Figure 5.3, and a non-magnetic envelope is actually a rather good approximation. However, the assumption of spherical symmetry at $\rho > \rho_b$ is questionable.

Given that the overall effect of the magnetic field, in the envelope, is not very strong, it turns out that the major uncertainty about the envelope is its chemical composition. The standard neutron star crust is made of cold catalyzed matter, which means ^{56}Fe at low density ($\rho < 10^6$ g cm^{-3}). However real neutron stars may be dirty and have lighter elements at their surface. As was shown in the presence of light elements in the envelope strongly enhances heat transport (e.g., the electron thermal conductivity within liquid ions of charge Z, in the sensitivity layer, is roughly proportional to $1/Z$ and results in a significantly higher T_e, for the same T_b, than in the case of a heavy element envelope. Due to pycnonuclear fusion, light elements are unlikely to be present
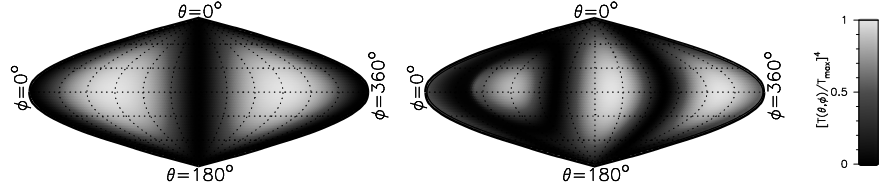
Figure 5.3: Two examples of surface temperature distributions induced by the magnetic field, in an area preserving projection of the neutron star surface (grey shading, shown on the right scale, follows the surface flux instead of the temperature). Left panel assumes a dipolar field, with strength 1.2×10^{12} G at the pole located at $(\theta, \phi) = (90^o, 90^o)$: for a core temperature of 4.05×10^7 K it gives $T_e = 5.43 \times 10^5$ K while the maximum and minimal surface temperatures, at the magnetic poles and along the magnetic equator, respectively, are $T_{max} = 6.70 \times 10^5$ K and $T_{min} = 1.4 \times 10^5$ K. The right panels shows the effect the same dipolar field to which a quadrupolar component has been added: this results in $T_e = 5.31 \times 10^5$ K. This particular latter case allows to reproduce the observed ROSAT X-ray pulse profile of Geminga which shows a single very broad pulse while a purely dipolar field would result in a double pulse profile (assuming the observer is in the direction $\theta \simeq 90^o$ and emission is isotropic blackbody). Finally, in absence of magnetic field, the same internal temperature would result in $T_e = 5.54 \times 10^5$ K.

at densities above 10^9 g cm^{-3}. At very high T_e this density is below the sensitivity layer and light elements have little effect, but for T_e within the observed range ($\sim 10^5 - 10^6$ K) the sensitivity layer is at a sufficiently low density so that it can easily be contaminated with light elements and the $T_b - T_e$ relationship can be significantly altered. However, if only a small amount of light elements is present at the surface their effect will only be felt a low T_e. In Fig. 5.4 is shown the $T_b - T_e$ relationships for various amounts of light elements and also, for comparison, the case of a magnetized envelope with a 10^{11} G dipolar magnetic field.
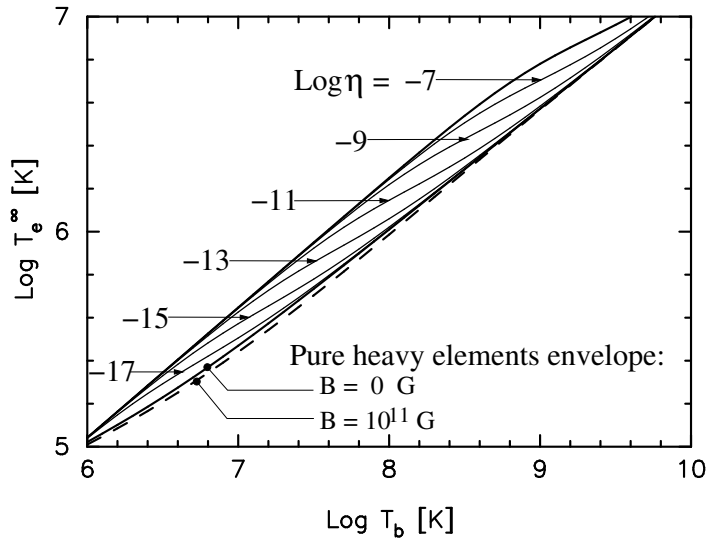
Figure 5.4: Relationship between the red-shifted effective temperature T_e^∞ and the interior temperature T_b at the bottom of the envelope assuming various amounts of light elements parameterized by $\eta \equiv g_{s\,14}^2 \Delta M_L / M$ (ΔM_L is the mass in light elements in the envelope, $g_{s\,14}$ the surface gravity in units of 10^{14} cm s^{-2}, and M is the star's mass), in the absence of a magnetic field . Also shown are the $T_b - T_e^\infty$ relationships for an envelope of heavy elements with and without the presence of a dipolar field of strength of 10^{11} G following. Notice that the smaller is ΔM_L the lower is the temperature at which its effect is felt.

5.2.2   Effective Masses

The connection between two-body and three-body forces within the meson-nucleon theory of the nuclear interaction is extensively discussed and developed in references [53]. At present the theoretical status of microscopically derived TBF is still quite rudimentary, however a tentative approach has been proposed using the same meson-exchange parameters as the underlying NN potential. Results have been obtained with the Argonne V_{18}, the Bonn B, and the Nijmegen 93 potentials [11].

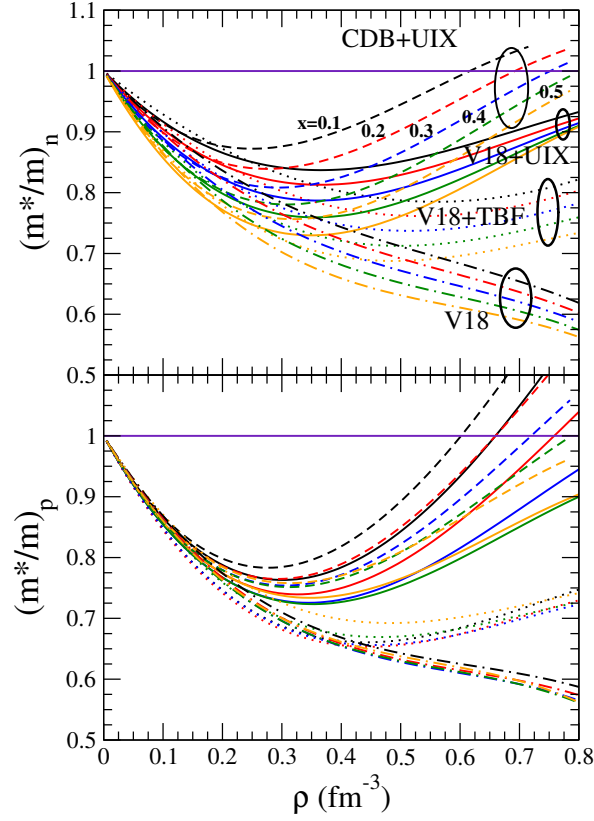The nucleon effective mass m^* describes the nonlocality of the single

Figure 5.5: The neutron/proton (top/bottom panel) effective mass is displayed vs. the nucleon density for several values of the proton fraction $x = 0.1, 0.2, 0.3, 0.4, 0.5$. Results are plotted for different choices of two- and three-body forces, as discussed in the text.

particle potential felt by a nucleon propagating in the nuclear medium. It is of great interest since it is closely related to many nuclear phenomena such as the dynamics of heavy-ion collisions at intermediate and high energies, the damping of nuclear excitations and giant resonances, and the adiabatic temperature of collapsing stellar matter. The momentum-dependent effective mass is defined in terms of the s.p. energy,

$$\frac{m^*(k)}{m} = \frac{k}{m} \left[\frac{de(k)}{dk} \right]^{-1}, \tag{5.8}$$

and clearly arises from both the momentum and energy dependence of the microscopic s.p. potential [54]. For the applications we consider the effective mass taken at the Fermi surface $k_{F_{n,p}}$. In this Section, I analyzed the effective mass obtained in the lowest-order BHF approximation discussed above. It is well know that including second-order "rearrangement" contributions to the s.p. potential increases the theoretical m^* values. However, the inclusion of the rearrangement term would require also the re-examination of the EOS, since the three hole-line contribution is altered by the modification of the s.p. potential, and it could be not any more negligible. I defer the analysis of this point to later work and concentrate here rather on the dependence of the results with respect to the choice of the two-body and three-body forces. NS matter is composed of asymmetric nuclear matter, where the effective mass depends both on the nucleon density and on the proton fraction $x = \rho_p/\rho$. The BHF neutron and proton effective masses in asymmetric matter are displayed in Fig. 5.5 as a function of the nucleon density for several values of the proton fraction. Different choices of the NN potential and TBF are compared, namely, I will display results for the Argonne V_{18} potential without TBF (V18, dash-dotted lines), with microscopic TBF (V18+TBF, dotted lines), with phenomenological Urbana TBF (V18+UIX, solid lines), and for the CD Bonn potential plus Urbana TBF (CDB+UIX, dashed lines). We see that without TBF the values of the effective masses decrease with increasing nucleon density, whereas the inclusion of TBF causes an increase of the values at densities above 0.3–0.4 fm^{-3} for both protons and neutrons and all considered models. This is due to the repulsive character of the TBF at high density. There is evidently a strong dependence on the chosen set of interactions, which reflects in particular the current theoretical uncertainty regarding nuclear TBF at high density. For easy implementation in astrophysical applications, polynomial fits of the effective

		a_1	b_1	c_1	a_2	b_2	c_2	a_3	b_3	c_3
V18	p	1.45	0.85	−0.92	2.10	1.26	−0.44	1.13	0.65	0.42
	n	0.96	0.92	0.59	1.20	1.38	1.64	0.71	0.65	0.98
V18+TBF	p	1.67	0.99	−2.47	2.7	1.18	−3.75	1.14	0.88	−2.4
	n	0.61	1.55	0.91	0.42	2.01	4.77	−0.17	0.58	4.44
V18+UIX	p	1.56	1.31	−1.89	3.17	1.26	−1.56	0.79	3.78	−3.81
	n	0.88	1.21	1.07	1.64	2.06	2.87	0.78	0.98	1.62
CDB+UIX	p	1.53	0.80	−1.04	3.05	1.06	−1.44	0.43	4.04	−4.42
	n	0.95	1.17	0.42	2.44	1.27	−0.05	1.30	0.55	−1.63

Table 5.2: Parameters of the polynomial fits, Eq. (5.10), for the neutron and proton effective masses, obtained with different interactions.

masses (valid for $\rho \leq 0.8 \text{ fm}^{-3}$) are provided,

$$
\begin{aligned}
\frac{m^*}{m}(\rho, x) \ &= 1 - (a_1 + b_1 x + c_1 x^2)\rho \\
&+ (a_2 + b_2 x + c_2 x^2)\rho^2 \\
&- (a_3 + b_3 x + c_3 x^2)\rho^3
\end{aligned}
\tag{5.9}
$$

whose parameters are reported in Table 5.2.

5.3   Neutrino emissivities

In this section I briefly recall the main neutrino emission mechanisms in NS and the relevance of the nucleon effective masses. Only the rates for the non-superfluid scenarios will be given, for which the dependence on the effective masses is via the general factor

$$
M_{ij} \equiv \left(\frac{\rho_p}{\rho_0}\right)^{1/3} \widetilde{M}_{ij} \ , \quad \widetilde{M}_{ij} \equiv \left(\frac{m_n^*}{m_n}\right)^i \left(\frac{m_p^*}{m_p}\right)^j .
\tag{5.10}
$$

In the presence of superfluidity the dependence is highly nontrivial and requires detailed calculations. In the following all emissivities Q are given in units of erg cm^{-3} s^{-1}.

In the absence of pairing, as already discussed, three main mechanisms are usually taken into account, which are the direct Urca (DU), the modified Urca (MU), and the NN bremsstrahlung (BNN) processes. By far the most efficient mechanism of NS cooling is the DU process, for which the derivation of the emissivity under the condition of β equilibrium is based on the β-decay theory. The result for npe NS matter is given by

$$Q^{(DU)} \approx 4.0 \times 10^{27} M_{11} T_9^6 \, \Theta(k_{F_p} + k_{F_e} - k_{F_n}) \, , \qquad (5.11)$$

where T_9 is the temperature in units of 10^9K. If muons are present, then the equivalent DU process may also become possible, in which case the neutrino emissivity is increased by a factor of 2.

The emissivities of the MU processes in the neutron and proton branches [55, 56] are given respectively by

$$Q^{(Mn)} \approx 8.1 \times 10^{21} M_{31} T_9^8 \alpha_n \beta_n \, ,$$
$$Q^{(Mp)} \approx 8.1 \times 10^{21} M_{13} T_9^8 \alpha_p \beta_p \left(1 - k_{F_e}/4k_{F_p}\right) \Theta_{Mp} \, , \qquad (5.12)$$

where the factor α_n (α_p) takes into account the momentum transfer dependence of the squared reaction matrix element of the neutron (proton) branch under the Born approximation, and β_n (β_p) includes the non-Born corrections due to the NN interaction effects, which are not described by the one-pion exchange. The currently adopted values are $\alpha_p = \alpha_n = 1.13$ and $\beta_p = \beta_n = 0.68$. The main difference between the proton branch and the neutron branch is the threshold character, since the proton branch is allowed only if $k_{F_n} < 3k_{F_p} + k_{F_e}$, in which case $\Theta_{Mp} = 1$. If muons are present in the dense NS matter, the equivalent MU processes become also possible.

Following the discussion above, the neutrino emissivity jumps directly from the value of the MU process to that of the DU process. Thus, the DU process appears in a step-like manner. In the absence of the DU process, the standard neutrino luminosity of the *npe* matter is determined not only by the MU processes but also by the BNN processes in NN collisions:

$$N + N \rightarrow N + N + \nu + \overline{\nu} \,. \tag{5.13}$$

These reactions proceed via weak neutral currents and produce neutrino pairs of any flavor. In analogy with the MU process, the emissivities depend on the employed model of NN interactions. Contrary to the MU, an elementary act of the NN bremsstrahlung does not change the composition of matter. The BNN has evidently no thresholds associated with momentum conservation and operates at any density in the uniform matter. The neutrino emissivity of the BNN processes in *npe* NS matter is

$$Q^{(Bnn)} \approx 2.3 \times 10^{20} M_{40} T_9^8 \alpha_{nn} \beta_{nn} (\rho_n/\rho_p)^{1/3} \,, \tag{5.14}$$

$$Q^{(Bnp)} \approx 4.5 \times 10^{20} M_{22} T_9^8 \alpha_{np} \beta_{np} \,, \tag{5.15}$$

$$Q^{(Bpp)} \approx 2.3 \times 10^{20} M_{04} T_9^8 \alpha_{pp} \beta_{pp} \,. \tag{5.16}$$

The dimensionless factors α_{NN} come from the estimates of the squared matrix elements at $\rho = \rho_0$: $\alpha_{nn} = 0.59$, $\alpha_{np} = 1.06$, $\alpha_{pp} = 0.11$. The correction factors β_{NN} are taken as $\beta_{nn} = 0.56$, $\beta_{np} = 0.66$, $\beta_{pp} = 0.70$. All three processes are of comparable intensity, with $Q^{(Bpp)} < Q^{(Bpn)} < Q^{(Bnn)}$.

5.4   Results for β-stable matter

For the treatment of NS matter we assume as usual charge neutral, $\rho_p = \rho_e + \rho_\mu$, and β-stable, $\mu_n - \mu_p = \mu_e = \mu_\mu$, nuclear matter. In Fig. 5.6 I
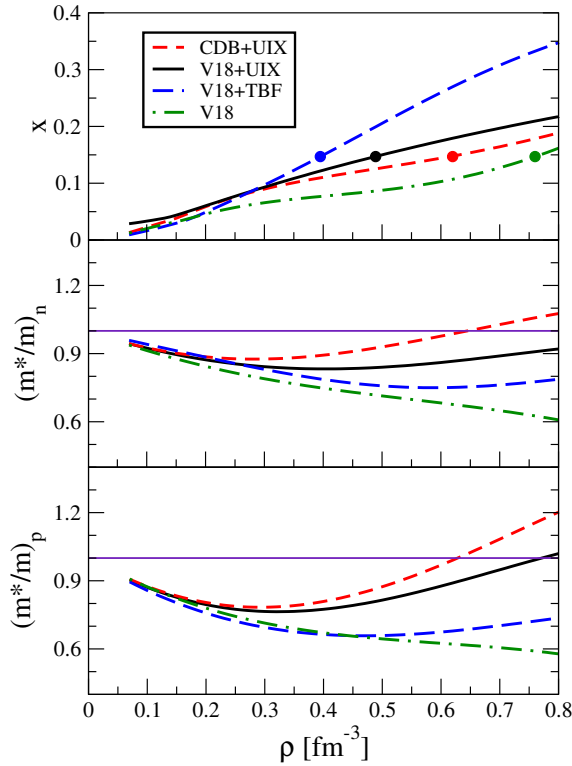
Figure 5.6: Proton fraction (upper panel; the dots indicate the onset of the DU process) and neutron/proton effective masses (central/lower panel) in β-stable matter obtained with different interactions.

show results for this case, obtained with the different combinations of two- and three-body potentials introduced before. In the upper panel the proton fraction is displayed as a function of the nucleon density, whereas the middle and lower panels show the neutron and proton effective masses, respectively.

We observe that the inclusion of TBF increases the proton fraction [57] due to the increased repulsion at large density, leading to the onset of the DU process in all cases (at different threshold densities indicated by markers). The effective masses also start to increase at high density due to the action of TBF, but depend strongly on the interactions: the
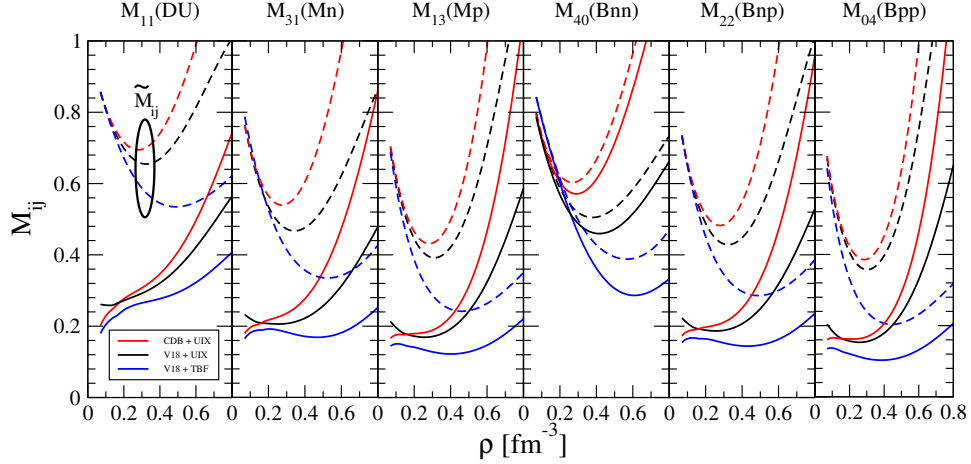
Figure 5.7: Reduction factors M_{ij} (solid lines) and $\widetilde{M}_{ij}$ (dashed lines) for the various cooling processes in β-stable matter obtained with different interactions. See text for details.

$V18 + TBF$ model predicts the strongest and the $CDB + UIX$ the weakest medium effects. Note that the value of the effective mass in β-stable matter obtained with different interactions is a consequence, apart from the differences shown in Fig. 5.5, also of the different proton fractions, as shown in the upper panel of Fig. 5.6.

Finally I combine the results shown in the various panels of Fig. 5.6 in order to obtain the reduction factors M_{ij}, $\widetilde{M}_{ij}$, Eq. (5.10), for the different cooling processes. Fig. 5.7 displays the different factors M_{11} (for DU), M_{31}, M_{31} (for MU), and M_{40}, M_{22}, M_{04} (for BNN) [solid curves] and the corresponding $\widetilde{M}_{ij}$ factors [dashed curves]. In line with the previous discussion, one notes again the strong interaction dependence of both the complete factors M_{ij} and the in-medium modification factors $\widetilde{M}_{ij}$. The latter show generally (apart from the CDB+UIX at high density) a reduction of the emissivities due to the general in-medium reduction of the effective masses.

5.5 The Study of Cooling

With the commissioning of increasingly sophisticated instruments, more and more details of the very faint signals emitted by neutron stars (NS) can be quantitatively monitored. This will allow in the near future an ever increasing accuracy to constrain the theoretical ideas for the ultra-dense matter that composes these objects.

One important tool of analysis is the temperature-vs-age cooling diagram, in which currently a few (~ 20) observed NS are located. NS cooling is over a vast domain of time ($10^{-10} - 10^5$ yrs) dominated by neutrino emission due to several microscopic processes [55, 58]. The theoretical analysis of these reactions requires the knowledge of the elementary matrix elements, the relevant beta-stable nuclear equation of state (EOS), and, most important, the superfluid properties of the stellar matter, i.e., the gaps and critical temperatures in the different pairing channels.

Even assuming (without proper justification) the absence of exotic components like hyperons and/or quark matter, the great variety of required input information under extreme conditions, that is theoretically not well under or out of control, renders the task of providing reliable and quantitative predictions currently extremely difficult.

Recently this activity has been spurred by the observation of very rapid cooling of the supernova remnant Cas A. Unfortunately we do not have a precise date for this event because probably the explosion was of magnitude + 6 being covered by galactic clouds. In any case we agree that the current age is 335 years and the surface temperature $T \approx 2 \times 10^6$ K. For this kind of compact object different analyses deduce a temperature decline of about 2 to 5 percent during the last ten years. [59, 60, 13]. Mass and radius of this object are not directly observed, but in recent works optimal values of $M = 1.62 \, \mathrm{M}_\odot$, $R \approx 10.2 \, km$ [13]

or a range of $M = (1.1 - 1.7)\,\mathrm{M}_\odot$, $R \approx (11.4 - 12.6)\,\mathrm{km}$ are reported, dependent on the assumed EOS.

Two major theoretical scenarios have been proposed to explain this observation: one is to assume a fine-tuned small neutron 3PF2 (n3P2) gap, $T_c \approx (5 - 9) \times 10^8\,\mathrm{K} \sim \mathcal{O}(0.1\,\mathrm{MeV})$ [61], that generates strong cooling at the right moment due to the superfluid neutron pair breaking and formation (PBF) mechanism; the other one is based on a strongly reduced thermal conductivity of the stellar matter that delays the heat propagation from the core to the crust to a time compatible with the age of Cas A. Both explanations have in common that they exclude the possibility of large ($\geq 0.1\,\mathrm{MeV}$) n3P2 gaps; in the first case because the corresponding critical temperature of the PBF process has to match the current internal temperature of Cas A; in the second case because such a gap would block too strongly the modified Urca (MU) cooling of the star and therefore lead to a too high temperature of Cas A.

Some alternative scenarios have also been brought forward. Amongst them, it was suggested that the fast cooling regime observed in Cas A can be explained if the Joule heating produced by dissipation of the small-scale magnetic field in the crust is taken into account. Another scenario suggested that the enhancement of the neutrino emission is triggered by a transition from a fully gapped two-flavor color-superconducting phase to a gapless/crystalline phase, although such a scenario requires a very massive $\sim 2\mathrm{M}_\odot$ star.

A common feature of all these cooling scenarios is that they exclude from the beginning the possibility of very fast direct Urca (DU) cooling, although many microscopic nuclear EOS do reach easily the required proton fractions for this process; and we will employ in this work an EOS that does so. However, the Akmal-Pandharipande-Ravenhall (APR) variational EOS [22], in spite of the fact that it does not reproduce the empirical saturation point of nuclear matter without an

ad-hoc correction, features a rather low proton fraction and DU cool-
ing only sets in for very heavy neutron stars, $M \geq 2\,\mathrm{M}_\odot$. Since in any
case neither this nor any other EOS can currently be experimentally
verified or falsified at high density, the frequent use of one particular
EOS represents an important bias that should not be underestimated.

Another critical point of most current cooling simulations is the
fact that EOS and pairing gaps are treated in disjoint and inconsistent
manner, i.e., a given EOS is combined with pairing gaps obtained within
a different theoretical approach and using different input interactions.

I tried to improve on both aspects, i.e., I included the DU cooling
process predicted by mine microscopic nuclear EOS, and I used com-
patible nuclear pairing gaps obtained with exactly the same nuclear
(in-medium) interaction. Furthermore, I also employed recent results
for nucleon effective masses obtained in the same approach with the
same interactions [11], which affect the microscopic cooling reactions.

5.6   Equation of state

The EOS labeled as "BHF" is the EOS studied until now (including
effective masses) while the "APR" is the well known EoS by Akmal,
Pandaripande and Ravenhall and discussed previously [22]. I use here
the original APR "$A18 + \delta v + \mathrm{UIX}^*$ corrected" results and not one of the
parametrized versions, where the high-density behavior is arbitrarily
modified.

I compare in Fig. 5.8 the NS EOS's obtained with the APR and BHF
models [19], i.e., panels (a) and (b) show pressure, energy density, and
proton and muon fractions of beta-stable and charge-neutral matter as
functions of the baryon density. It is obvious that the crucial difference
between both models is the much higher proton fraction in the BHF
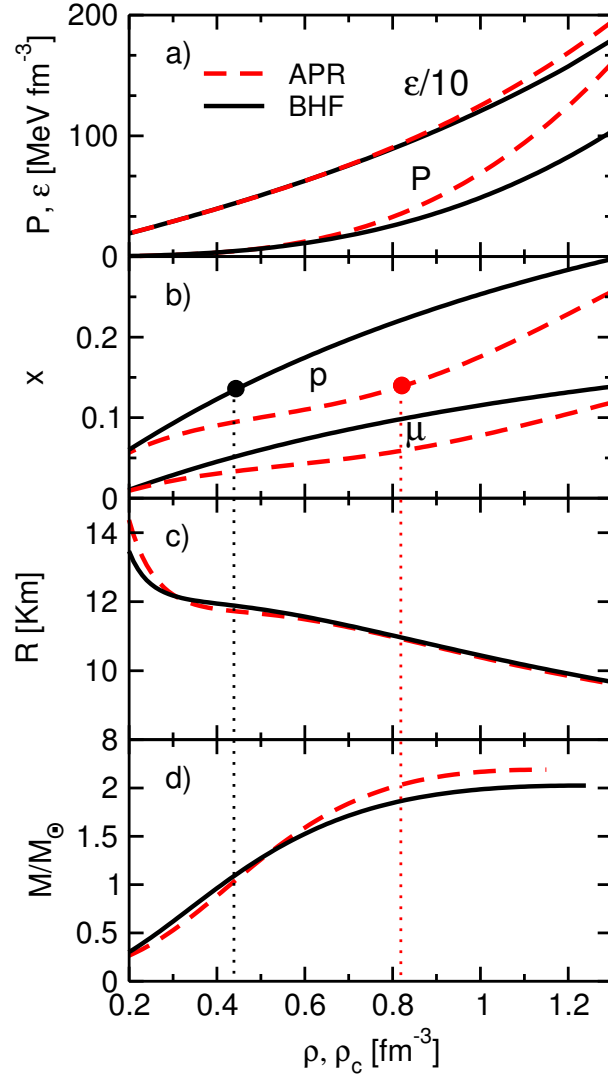approach. In this case the DU threshold is already reached at $\rho =$

Figure 5.8: Pressure and energy density (a), and proton and muon fractions (b) as functions of baryon number density ρ in beta-stable matter for the APR and BHF EOS. The lower panels show neutron star mass (d) and radius (c) as functions of the central density ρ_c. The DU onset is indicated by vertical dotted lines.
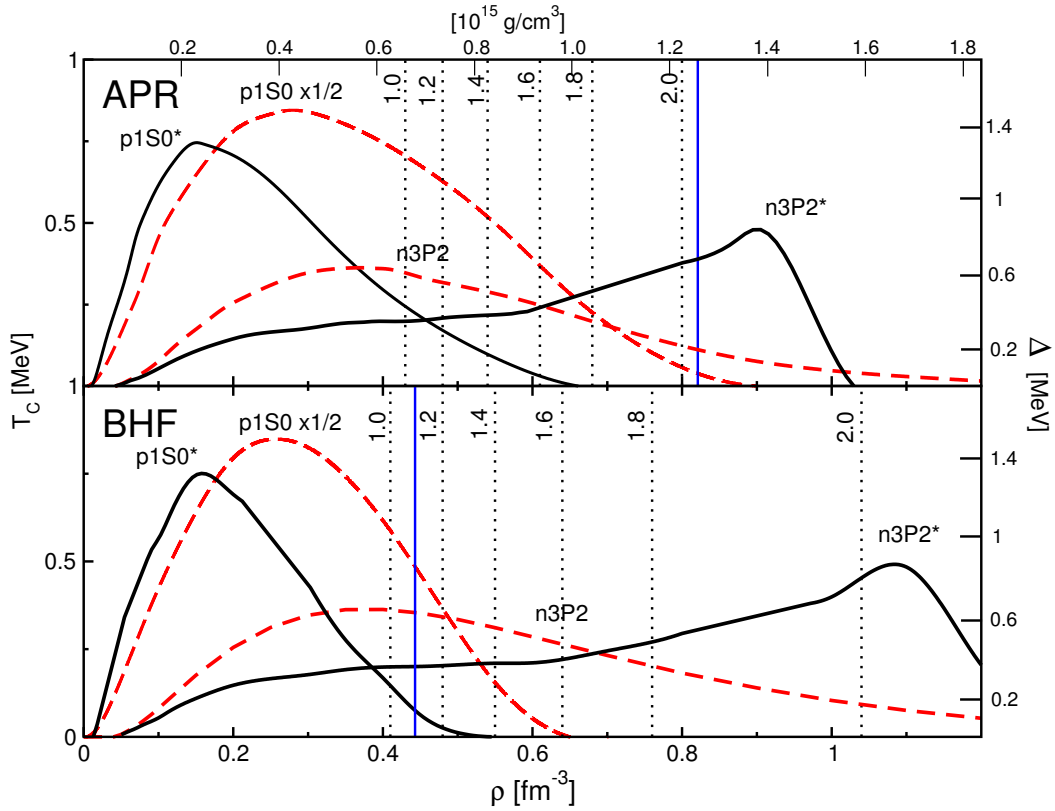
Figure 5.9: Pairing gaps in NS matter for the APR and BHF models in the p1S0 and n3P2 channels, including (*) or not effective mass effects. Vertical dotted lines indicate the central density of NS with different masses $M/M_\odot = 1.0, ..., 2.0$. DU onset occurs at the vertical solid (blue) lines. Note the scaling factor 1/2 for the p1S0 curves.

$0.44\,\text{fm}^{-3}$ ($x_p = 0.136$), whereas with the APR it is delayed to $\rho = 0.82\,\text{fm}^{-3}$ ($x_p = 0.140$).

On the contrary, the APR EOS is somewhat stiffer, i.e., features a larger pressure and energy density. I also mention that the APR EOS becomes superluminal at $\rho = 0.85\,\text{fm}^{-3}$, whereas BHF remains always below the critical threshold.

By solving the standard Tolman-Oppenheimer-Volkov equations for the NS structure, this input yields the NS (mass , radius) – central density relations shown in panels (c) and (d) of Fig. 5.8. I remark that both models reach maximum masses (slightly) above two solar masses and predict very similar radii in spite of their different matter composition. With BHF the DU process is active in nearly all stars, $M/M_\odot > 1.10$, while with APR only in the most heavy ones, $M/M_\odot > 2.03$. This has profound consequences for the cooling behavior.

5.7   Pairing gaps and critical temperatures

Of vital importance for any cooling simulation is the knowledge of the 1S0 and 3PF2 pairing gaps for neutrons and protons in beta-stable matter, which on one hand block the DU and MU reactions, and on the other hand open new cooling channels by the PBF mechanism for stellar matter in the vicinity of the critical temperature. As usual, I focus on the most important proton 1S0 (p1S0) and neutron 3PF2 (n3P2) pairing channels and neglect the less important remaining combinations.

As stressed before, the gaps should be computed in a framework that is consistent with the determination of the EOS, i.e., be based on the same NN interaction and using the same medium effects (TBF and effective masses), and indeed we follow this procedure here, which employed the same $V_{18} + UIX$ nuclear interaction and BHF s.p. spectra

for the calculation of the gaps. To be more precise, and focusing on the more general case of pairing in the coupled 3PF2 channel, the pairing gaps were computed on the BCS level by solving the (angle-averaged) gap equation [62, 63] for the two-component $L = 1, 3$ gap function,

$$\begin{pmatrix} \Delta_1 \\ \Delta_3 \end{pmatrix}(k) = -\frac{1}{\pi} \int_0^\infty dk' k'^2 \frac{1}{E(k')} \begin{pmatrix} V_{11} & V_{13} \\ V_{31} & V_{33} \end{pmatrix}(k, k') \begin{pmatrix} \Delta_1 \\ \Delta_3 \end{pmatrix}(k') \quad (5.17)$$

with

$$E(k)^2 = [e(k) - \mu]^2 + \Delta_1(k)^2 + \Delta_3(k)^2 , \quad (5.18)$$

while fixing the (neutron or proton) density,

$$\rho = \frac{k_F^3}{3\pi^2} = 2 \sum_k \frac{1}{2} \left[1 - \frac{e(k) - \mu}{E(k)} \right] . \quad (5.19)$$

Here $e(k)$ are the BHF s.p. energies containing contributions due to two-body and three-body forces, $\mu \approx e(k_F)$ is the (neutron) chemical potential determined self-consistently from Eqs. (5.17–5.19), and

$$V_{LL'}(k, k') = \int_0^\infty dr\, r^2\, j_{L'}(k'r)\, V_{LL'}^{TS}(r)\, j_L(kr) \quad (5.20)$$

are the relevant potential matrix elements ($T = 1$ and $S = 1$; $L, L' = 1, 3$ for the 3PF2 channel, $S = 0$; $L, L' = 0$ for the 1S0 channel) with

$$V = V_{18} + \bar{V}_{UIX} , \quad (5.21)$$

composed of two-body force and averaged TBF. The relation between (angle-averaged) pairing gap at zero temperature is

$$\Delta \equiv \sqrt{\Delta_1^2(k_F) + \Delta_3^2(k_F)} \quad (5.22)$$

obtained in this way and the critical temperature of superfluidity is then $T_c \approx 0.567\,\Delta$. Fig. 5.9 displays the p1S0 and n3P2 pairing gaps as a function of baryonic density of beta-stable matter for the APR (upper panel) and BHF (lower panel) models. Also indicated are the

central densities of NS with different masses, in order to easily identify which range of gaps is active in different stars. Note that the in-medium modification of the pairing interaction is treated consistently (via the compatible s.p. energies and TBF) only in the BHF model.

Different levels of approximation for the calculation of gaps were discussed, in particular one including only the two-body force V_{18} in Eq. (5.21) together with the kinetic s.p. energies, and another one (curves denoted by p1S0* and n3P2* in Fig. 5.9) using the BHF s.p. spectra. Note that polarization corrections [64] were not considered in that work, which for the case of the 1S0 channel are known to be repulsive, but for the 3PF2 are still essentially unknown, and might change the value of the gaps even by orders of magnitude. In order to represent this uncertainty, we use in the cooling simulations the density dependence of the pairing gaps shown in Fig. 5.9, but employ global scaling factors s_p and s_n, respectively.

Qualitatively one observes in Fig. 5.9 the natural scaling effect of the different proton fractions for the BHF and APR EOS, such that the p1S0 gaps extend to larger (central) densities for the APR model, due to the lower proton fraction in that case. Therefore the blocking effect on the cooling extends up to higher densities and NS masses for the APR model. The crucial difference is again the onset of the DU process, which is active for nearly all NS in the BHF case. However, the n3P2$^{(*)}$ gaps extend up to very large density and can thus provide an efficient means to block this cooling process, in particular for the n3P2* model comprising medium effects. The price to pay is an enhanced PBF cooling rate close to the critical temperature in that case. Note that the 3P2 gaps shown in the figure are larger than those currently employed in cooling simulations, which will be discussed in the next section, and that at the moment there exists no satisfactory theoretical calculation of p-wave pairing that includes consistently all medium effects.

5.8 Neutron star cooling and Cas A

Having quantitatively specified EOS and pairing gaps, the NS cooling simulations are carried out using the widely used code `NSCool` [65], which comprises all relevant cooling reactions: DU, MU, PBF, and Bremsstrahlung.

A further important ingredient of the simulations is the (leptonic and baryonic) thermal conductivity. Recently it has been conjectured that the conductivities could be substantially (by one order of magnitude) suppressed by in-medium effects, and this has been put forward as an alternative explanation of the rapid Cas A cooling. We follow this idea by introducing a further global scale factor s_κ multiplying the total thermal conductivity. Therefore our calculations are controlled by the three global parameters s_p, s_n, s_κ, and we present now some selected results for certain parameter choices.

5.8.1 Scenario 1: Original model, no scaling

For the sake of illustration and better understanding, I begin by showing the results obtained with the original pairing gaps shown in Fig. 5.9, and without any modification of the conductivities, i.e., setting $s_p = s_n = s_k = 1$. Moreover we use the neutron $^1S_0$ BCS gap without any rescaling, although the beta-stable matter in the relevant subnuclear density domain of the crust is inhomogeneous and therefore more elaborate considerations should be done.

The upper panel of Fig. 5.10 shows the temperature vs age results (11 curves for NS with masses $1.0, 1.1, ..., 2.0$) obtained with the BCS gaps without any medium modification (dashed red curves in the lower panel of Fig. 5.9), while the lower panel employs the gaps with BHF effective masses (black curves in Fig. 5.9), which is indicated by the notation $s_p^* = s_n^* = 1$ here and in the following. In all cases a heavy (Fe)
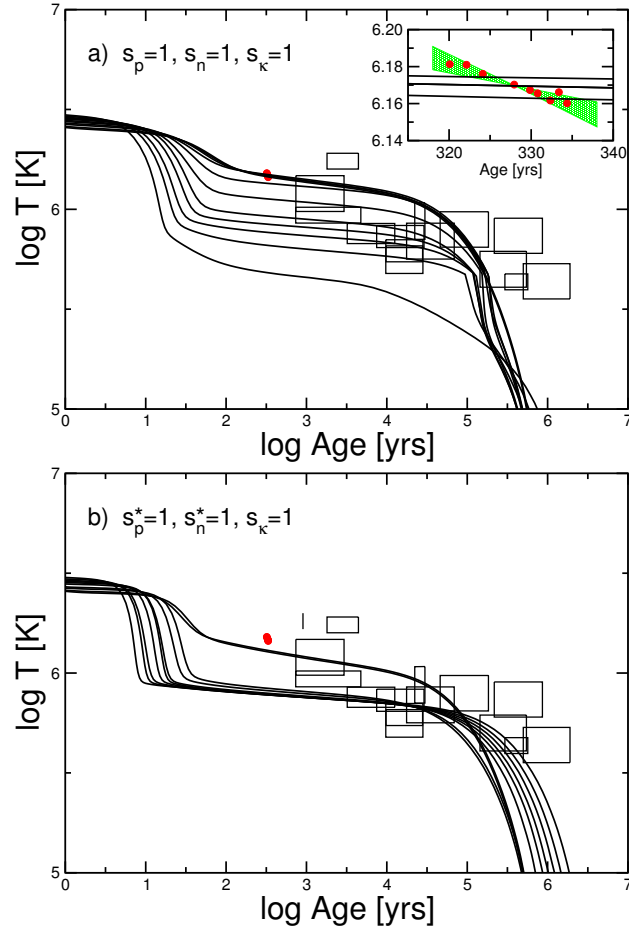
Figure 5.10: Cooling curves with the BHF EOS and no scaling factors, for different NS masses $M/M_\odot = 1.0, 1.1, ..., 2.0$ (decreasing curves). The upper panel employs BCS gaps with free s.p. spectra, whereas in the lower panel the BHF s.p. spectra are used. Red dots show the Cas A cooling data (enlarged in the inset of the upper panel; the $M/M_\odot$ =1.1 and 1.2 curves overlap).

elements atmosphere ($\eta = 0$) has been assumed. One observes results in line with the features of the pairing gaps , namely in the upper panel light ($M \leq 1.4\,\mathrm{M_\odot}$) NS cool slower and heavy ($M \geq 1.7\,\mathrm{M_\odot}$) NS cool faster than in the lower panel. This is due to the larger overall values of the corresponding BCS gaps in the low-density ($n \leq 0.6\,\mathrm{fm}^{-3}$) region and the smaller n3P2 value in the high-density ($n \geq 0.7\,\mathrm{fm}^{-3}$) domain, see Fig. 5.9, which cause, respectively, a stronger or weaker blocking of the dominant DU process in light or heavy stars.

Very old and warm stars (PSR B1055-52, RX J0720.4-3125) are not covered by any cooling curve, just as in the equivalent investigation within the APR model. Altogether the cooling curves for warm stars appear quite similar to those in that reference, while there is no difficulty at all to explain cold stars due to the DU mechanism in the BHF model.

The major shortcoming of both scenarios in Fig. 5.10 is that they cannot reproduce the particular cooling properties of Cas A; while the first one can fit its current age and temperature as a M= $1.2\,\mathrm{M_\odot}$ NS, neither reproduces the very fast current cooldown, shown in the inset of the upper panel. Precisely for this reason special scenarios with fine-tuned parameters have been developed, which I analyze now.

5.8.2 Scenario 2: Neutron pair breaking cooling

A frequent explanation of the rapid cooling of Cas A is the one based on an appropriately chosen n3P2 gap, which causes strong cooling due to the opening of the neutron PBF process at the current age/temperature of the star. The BHF EOS including strong DU reactions also allows this interpretation by choosing the scaling factors $s_p = 2.0$, $s_n = 0.132$, $s_\kappa = 1$ for a $1.4\,\mathrm{M_\odot}$ star, corresponding to maximum values of the gaps $\Delta_p \approx 6\,\mathrm{MeV}$ and $\Delta_n \approx 0.1\,\mathrm{MeV}$, i.e., Δ_p is larger than usually chosen (in order to block the fast DU reaction; the domain of the p1S0 gap
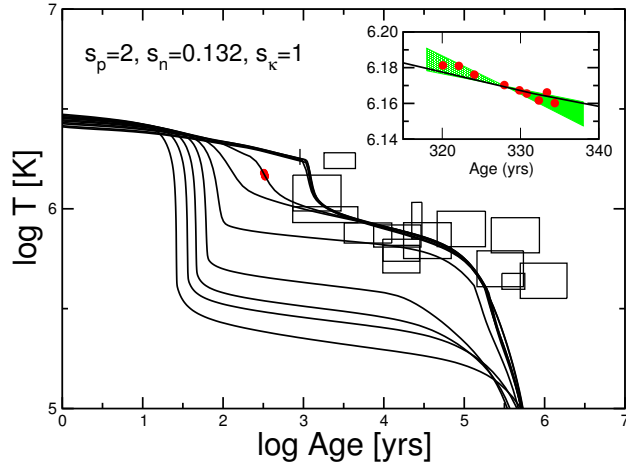
Figure 5.11: Same as Fig. 5.10, for the PBF cooling scenario. The M= 1.4 M$_\odot$ cooling curve passes through Cas A by construction.

fully covers NS up to about 1.6 M$_\odot$, see Fig. 5.10).

The results are shown in Fig. 5.11, which displays the sequence of cooling curves for NS masses M/M$_\odot$ = 1.0, 1.1, ..., 2.0, the 1.4 case corresponding to Cas A by construction; (this might be changed within reasonable limits by choosing different scaling factors). In this case the neutron $^1S_0$ gap has been rescaled by a factor 0.04 for finetuning. As in similar investigations, one notes that the rapid cooldown caused by the n3P2 PBF renders even more difficult the reproduction of old hot stars. Also for this reason alternative scenarios have been developed, and I analyze one of them now.

5.8.3   Scenario 3: Suppressed thermal conductivity

This approach features strongly suppressed lepton and baryon thermal conductivities, which we roughly simulate by the scaling parameter s_κ. This serves to delay the temperature decline up to the current age of Cas A without need to introduce fine-tuned nPBF cooling. A further peculiarity of this model is the fact that the standard MU cooling is
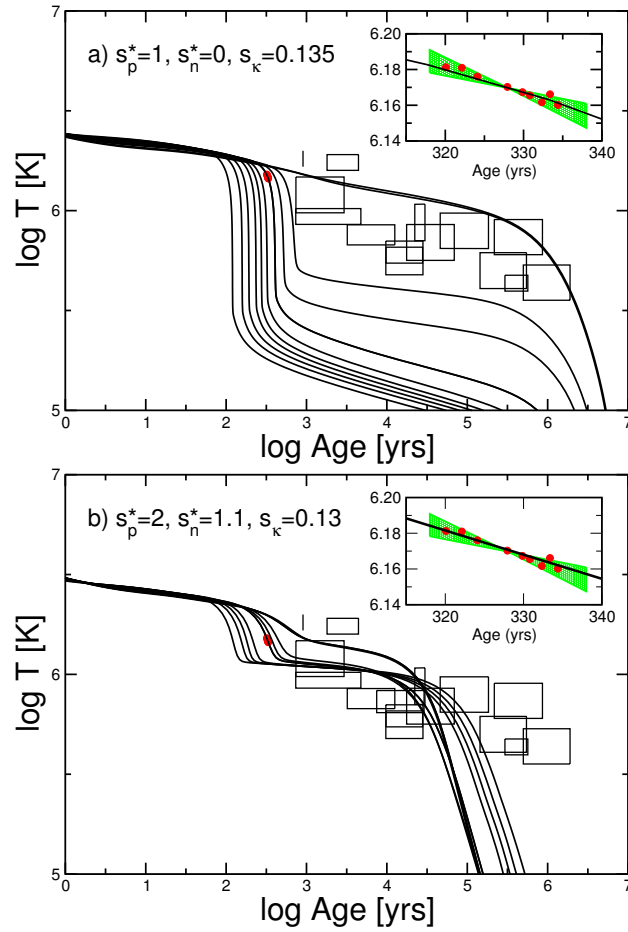
Figure 5.12: Same as Fig. 5.11, for two delayed cooling scenarios.

strongly enhanced by assumed in-medium effects (MMU), which provides fast cooling for heavy NS, without need of DU cooling [66]. Our EOS also accommodates this possibility, as demonstrated in Fig. 5.12. The upper panel shows a rather satisfactory fit of all cooling data including Cas A, employing the parameter set $s_p^* = 1$, $s_n^* = 0$, $s_\kappa = 0.135$, where the size of s_κ is comparable to the values of about 0.2 deduced in [67, 68].

In this scenario a rather small value of the n3P2 gap seems to be required, as otherwise old hot (and also young cold) NS cannot be obtained, even if Cas A is reproduced. This is demonstrated by a typical result ($s_n^* = 2.0$, $s_n^* = 1.1$, $s_\kappa = 0.13$, the n1S0 gap has been reduced by 0.09, and $\eta = 0.03$ here), shown in the lower panel of the figure, where large values for both gaps are used. The finite large n3P2 gap causes an early rapid cooldown incompatible with the temperature of most old NS, but at the same time together with the large p1S0 gap reduces too strongly the DU and MU cooling in order to fit young cold stars.

5.8.4   Scenario 4: No Cas A constraint

The previous results have shown that it is difficult to satisfy simultaneously the rapid cooling of Cas A and the slow cooling of old NS. However, recently doubts have been expressed about the validity of the Cas A data analysis, such that a future revision is not excluded. In any case I study finally a scenario without the Cas A constraint (apart from reproducing its current age and temperature with a reasonable mass) in mine strong DU model, trying to cover the full range of current cooling data. Starting from the observation that the use of the unscaled BCS gaps in Fig. 5.10 yields already a resonable reproduction of most young NS, and considering the fact that a finite n3P2 gap produces too strong PBF cooling, simply switching off this channel yields a nearly perfect
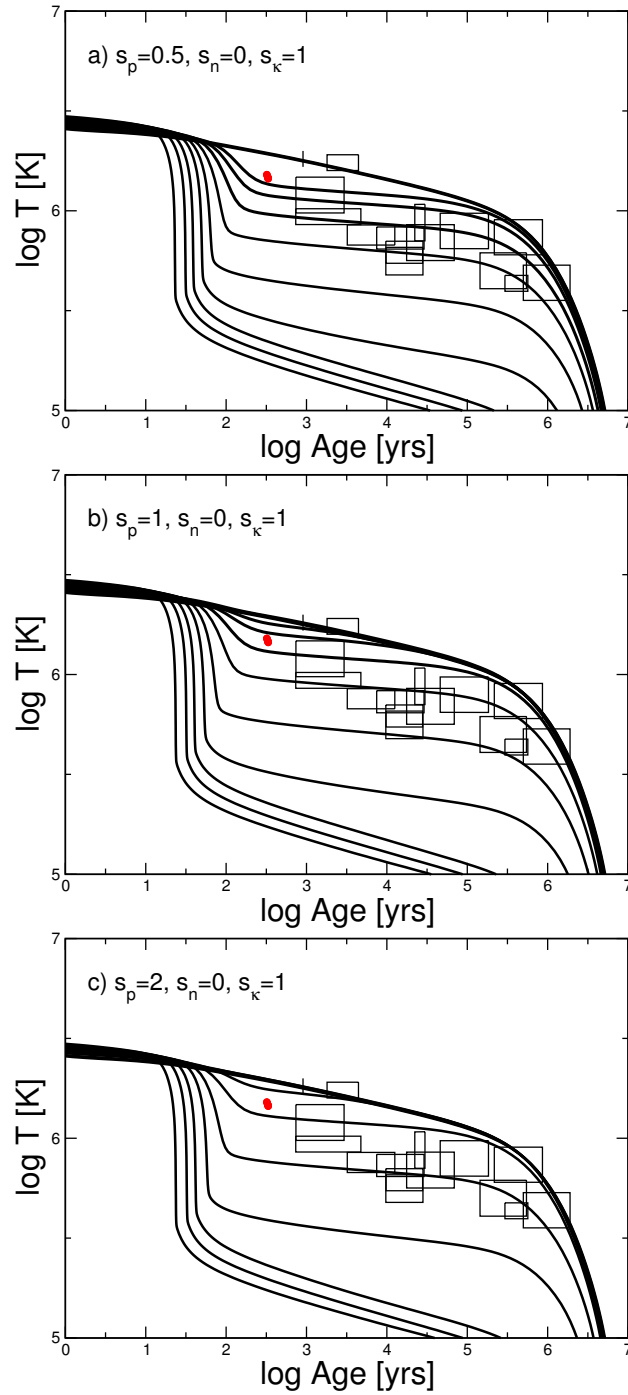
Figure 5.13: Same as Fig. 5.10, using $s_n = 0$, $s_\kappa = 1$, and different choices of $s_p = 0.5, 1.0, 2.0$ (from top to bottom).

coverage of all current cooling data, as shown in Fig. 5.13(b). In this scenario Cas A turns out a $1.31M_\odot$ NS.

Thus the BCS p1S0 gap alone is able to suppress sufficiently the DU cooling, provided that it extends over a large enough density range. Since in this case the p1S0 gap is perhaps somewhat large (although this might be compensated by a different density shape), I finally investigate the effect of rescaling it with factors $s_p = 0.5$ and $s_p = 2$, shown in panels (a) and (c). It turns out that in both cases the quality of the cooling simulation remains excellent, just the predicted mass of Cas A is varying between $1.18M_\odot$ and $1.46M_\odot$. This illustrates the dire necessity of precise information on the masses of the NS in the cooling diagram, without which no theoretical cooling model can be verified.

Chapter 6

Quark Matter

Contents

Physicists have long thought that once crossed the short-range re-
pulsion of the strong interaction, can be found a new state of matter.
Nowadays the theoretical idea provides a more accurate picture of this
new state of matter: it should be the quark-gluon plasma (QGP), in
which quarks and gluons, the fundamental constituents of matter, are
no longer confined within the dimensions of nucleons, but are free to
move around an area in which high temperature or high density pre-
vail. It is expected that collisions of heavy ions at high energies at a
sufficiently high density can get to form this new state of matter [3].
Quarks and gluons may wander freely inside the fireball created by the
collisions. The energies of individual quarks and gluons are typically
those of a very high temperature (about 200 MeV) although the sys-
tem would not have the time to fully thermalize. The identification of
the QGP state in collisions of relativistic heavy ions is, however, ex-
tremely difficult. If created, the state of the QGP would have a very
short existence. From a theoretical point of view, there is a rigorous
theory of dense nuclear matter. In the Fig.6.1 it is shown a possible
phase diagram of QCD, which shows the temperature as a function of
the baryon density. The region of low temperature and density is the
normal phase of nuclear matter. At high temperature and low density
we expect to find the quark-gluon plasma. For the transition temper-
ature to this new state, the calculations of QCD give values between
140 and 180 MeV, corresponding to a density of about 1 GeV/fm^3, or
seven times the saturation density. Temperatures and densities higher
than these values were existed in the young universe a few microsec-
onds after the Big Bang. At sufficiently high density and temperatures
close to zero we find neutron stars. In fact, the conditions in the core
of neutron stars may be such that the ordinary hadronic matter, in
which quarks are confined in hadrons, is converted by high pressure in
relation to quarks, forming a hybrid star, a star with a quark matter
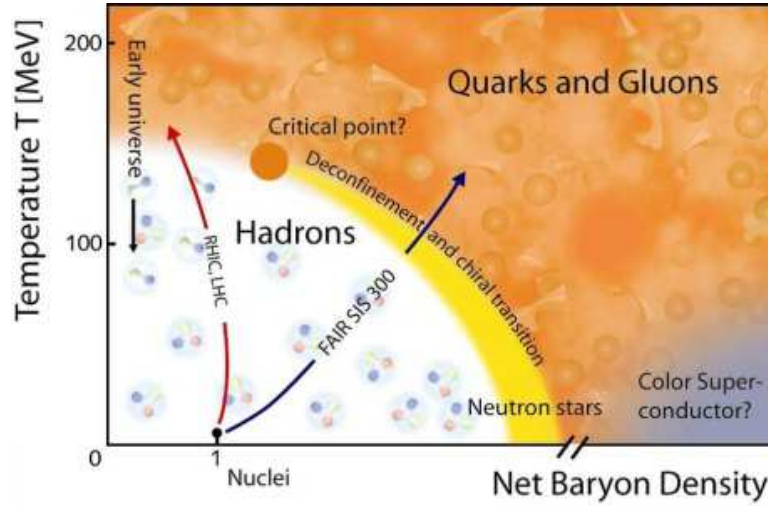
region in the core and an hadronic envelope.

Figure 6.1: Phase diagram for matter.

Therefore the knowledge of EoS both for hadronic and quark matter is necessary to estimate the possible effects of this transition in neutron stars.

6.1 The CSS parametrization

During my PhD course, in collaboration with Prof. M. Alford (University of Saint Louis, Missouri, USA), I also focused on the study of the "constant speed of sound" (CSS) parametrization of the EoS of high-density matter and its application to the field correlator method (FCM) model of quark matter. I show how mass and radius observations can be expressed as constraints on the CSS parameters. Here I analyze a specific example [16], where the high-density matter is quark matter described by a model based on the field correlator method showing how its parameters can be mapped on to the CSS parameter space, and how it is constrained by currently available observations of neutron stars.

The CSS parametrization is applicable to high-density equations of state for which (a) there is a sharp interface between nuclear matter and a high-density phase which we will call quark matter, even when we do not make any assumptions about its physical nature; and (b) the speed of sound in the high-density matter is pressure-independent for pressures ranging from the first-order transition pressure up to the maximum central pressure of neutron stars. One can then write the high-density EoS in terms of three parameters: the pressure p_{trans} of the transition, the discontinuity in energy density $\Delta\epsilon$ at the transition, and the speed of sound c_{QM} in the high-density phase. For a given nuclear matter EoS $\epsilon_{NM}(p)$, the full CSS EoS is then

$$\epsilon(p) = \begin{cases} \epsilon_{NM}(p) & p < p_{trans} \\ \epsilon_{NM}(p_{trans}) + \Delta\epsilon + c_{QM}^{-2}(p - p_{trans}) & p > p_{trans} \end{cases} \qquad (6.1)$$

The CSS form can be viewed as the lowest-order terms of a Taylor expansion of the high-density EoS about the transition pressure. We express the three parameters in dimensionless form, as $p_{trans}/\epsilon_{trans}$, $\Delta\epsilon/\epsilon_{trans}$ and c_{QM}^2, where $e_{trans} \equiv \epsilon_{NM}(p_{trans})$.

The assumption of a sharp interface will be valid if, for example, there is a first-order phase transition between nuclear and quark matter, and the surface tension of the interface is high enough to ensure that the transition occurs at a sharp interface (Maxwell construction) not via a mixed phase (Gibbs construction). Given the uncertainties in the value of the surface tension, this is a possible scenario. One can also formulate generic equations of state that model interfaces that are smeared out by mixing or percolation.

The assumption of a density-independent speed of sound is valid for a large class of models of quark matter. The CSS parametrization is an almost exact fit to some Nambu–Jona-Lasinio models. The perturbative quark matter EoS also has roughly density-independent c_{QM}^2, with a value around 0.2 to 0.3 (in this Chapter I use units where $\hbar = c = 1$),

above the transition from nuclear matter. In the quartic polynomial parametrization, varying the coefficient a_2 between $\pm(150MeV)^2$, and the coefficient a_4 between 0.6 and 1, and keeping n_{trans}/n_0 above 1.5, one finds that c^2_{QM} is always between 0.3 and 0.36. It is noticeable that models based on relativistic quarks tend to have $c^2_{QM} \approx 1/3$, which is the value for systems with conformal symmetry, and it has been conjectured that there is a fundamental bound $c^2_{QM} < 1/3$, although some models violate that bound. The CSS parametrization is constrained by observables such as the maximum mass M_{max}, the radius of a maximum-mass star, and the radius $R_{1.4}$ of a star of mass $1.4 M_{solar}$.

6.2 Constraining the CSS parameters

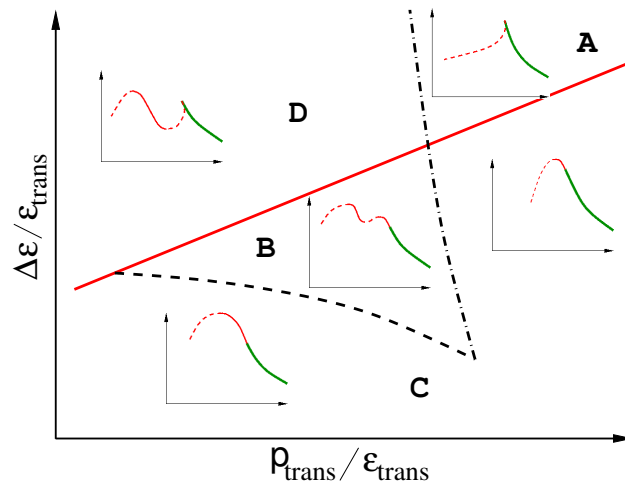### 6.2.1 Topology of the mass-radius relation

Figure 6.2: Schematic phase diagram for hybrid star branches in the mass-radius relation of compact stars. We fix c^2_{QM} and vary $p_{trans}/\epsilon_{trans}$ and $\Delta\epsilon/\epsilon_{trans}$. The four regions are (A) no hybrid branch ("absent"); (B) both connected and disconnected hybrid branches; (C) connected hybrid branch only; and (D) disconnected hybrid branch only.

We use the term "hybrid star" to refer to stars whose central pressure is above p_{trans}, and so they contain a core of the high-density phase. The part of the mass-radius relation that arises from such stars is the hybrid branch. In all models of nuclear/quark matter I find the same four topologies of the mass-radius curve for compact stars: the hybrid branch may be connected to the nuclear branch (C), or disconnected (D), or both may be present (B) or neither (A). The occurrence of these as a function of the CSS parameters $p_{trans}/\epsilon_{trans}$ and $\Delta\epsilon/\epsilon_{trans}$ at fixed c_{QM}^2 is shown schematically in Fig. 6.2. The mass-radius curve in each region is depicted in inset plots, in which the thick green line is the hadronic branch, the thin solid red lines are stable hybrid stars, and the thin dashed red lines are unstable hybrid stars.

In the phase diagram the solid red line shows the threshold value Δ_{crit} below which there is always a stable hybrid star branch connected to the neutron star branch. This critical value is given by [69]

$$\frac{\Delta_{crit}}{\epsilon_{trans}} = \frac{1}{2} + \frac{3}{2}\frac{p_{trans}}{\epsilon_{trans}} \tag{6.2}$$

and was obtained by performing an expansion in powers of the size of the core of high-density phase. Eq. 6.2 is an analytic result, independent of c_{QM}^2 and the nuclear matter EoS. The dashed and dot-dashed black lines mark the border of regions where the disconnected hybrid star branch exists. The position of these lines depends on the value of c_{QM}^2 and (weakly) on the accompanying nuclear matter EoS. Once a nuclear matter EoS has been chosen, any high-density EoS that is well approximated by the CSS parametrization can be summarized by giving the values of the three CSS parameters, corresponding to a point in the phase diagram. We then know what sort of hybrid branches will be present.

6.2.2 Maximum mass of hybrid stars

In Fig. 6.3 I show how mass measurements of neutron stars can be expressed as constraints on the CSS parameters. Each panel shows dependence on $p_{trans}/\epsilon_{trans}$ and $\Delta\epsilon/\epsilon_{trans}$ for fixed c_{QM}^2, as in Fig. 6.2.
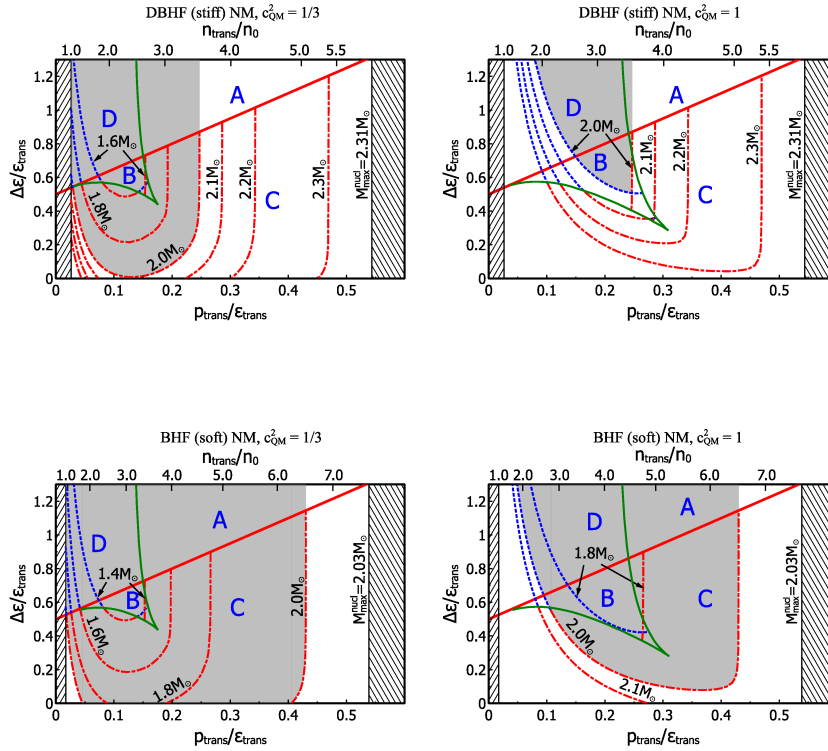

Figure 6.3: Contour plots showing the maximum hybrid star mass as a function of the CSS parameters of the high-density EoS. See the text for details.

The region in which the transition to quark matter would occur below nuclear saturation density ($n_{trans} < n_0$) is excluded (hatched band at the left end) because in that region bulk nuclear matter would be metastable. There is also an upper limit on the transition pressure, which is the central pressure of the heaviest stable nuclear matter star.

This depends on the hadronic EoS that had been assumed.

Property	BHF, Av_{18} + UVIX TBF	DBHF, Bonn A
Saturation baryon density $n_0(\text{fm}^{-3})$	0.16	0.18
Binding energy/baryon E/A (MeV)	-15.98	-16.15
Compressibility K_0 (MeV)	212.4	230
Symmetry energy S_0 (MeV)	31.9	34.4
$L = 3n_0\,[dS_0/dn]_{n_0}$ (MeV)	52.9	69.4
Maximum mass of star (M_{solar})	2.03	2.31
Radius of the heaviest star (km)	9.92	11.26
Radius of $M = 1.4\,M_{solar}$ star (km)	11.77	13.41

Table 6.1: Calculated properties of symmetric nuclear matter for the BHF and Dirac-Brueckner-Hatree-Fock (DBHF) nuclear equations of state used here. BHF is softer, and DBHF is stiffer.

The contours show the maximum mass of a hybrid star as a function of the EoS parameters. The region inside the $M = 2M_{solar}$ contour corresponds to EoS's for which the maximum mass is less than $2M_{solar}$ so it is shaded to signify that this region of parameter space for the high-density EoS is excluded by the observation of a star with mass $2M_{solar}$ [6]. For high-density EoSs with $c_{QM}^2 = 1$ (right-hand plots), this region is not too large, and leaves a good range of transition pressures and energy density discontinuities that are compatible with the observation. However, for high-density matter with $c_{QM}^2 = 1/3$ (left-hand plots), which is the typical value in many models, the $M_{max} > 2M_{solar}$ constraint eliminates a large region of the CSS parameter space.

The upper plots in Fig. 6.3 are for a stiffer nuclear matter EoS, DBHF [70], and the lower plots are for a softer nuclear matter EoS, BHF. [9]. As one would expect, the stiffer EoS gives rise to heavier (and larger) stars, and therefore allows a wider range of CSS parameters to be compatible with the $2M_{solar}$ measurement.

In Fig. 6.3 the dot-dashed (red) contours are for hybrid stars on a connected branch, while the dashed (blue) contours are for disconnected branches. When crossing the near-horizontal boundary from region C to B the connected hybrid branch splits into a smaller connected branch and a disconnected branch, so the maximum mass of the connected branch smoothly becomes the maximum mass of the disconnected branch. Therefore the red contour in the C region smoothly becomes a blue contour in the B and D regions. When crossing the near-vertical boundary from region C to B a new disconnected branch forms, so the connected branch (red dot-dashed) contour crosses this boundary smoothly.

In each panel of Fig. 6.3, the physically relevant allowed region is the white unshaded region. The grey shaded region is excluded by the existence of a $2M_{solar}$ star. We see that increasing the stiffness of the hadronic EoS or of the quark matter EoS (by increasing c_{QM}^2) shrinks the excluded region.

For both the hadronic EoSs that I study, the CSS parameters are significantly constrained. From the two left panels of Fig. 6.3 one can see that if, as predicted by many models, $c_{QM}^2 \leq 1/3$, then I are limited to two regions of parameter space, corresponding to a low pressure transition or a high pressure transition. In the low-transition-pressure region the transition occurs at a fairly low density $n_{trans} \leq 2n_0$, and a connected hybrid branch is possible. In the high-transition-pressure region the connected branch (red dot-dashed) contours are, except at very low $\Delta\epsilon$, almost vertical, corresponding to EoSs that give rise to a very small connected hybrid branch which exists in a very small range of central pressures p_{cent} just above p_{trans}. The maximum mass on this branch is therefore very close to the mass of the purely hadronic matter star with $p_{cent} = p_{trans}$. The mass of such a purely hadronic star is naturally independent of parameters that only affect the quark

matter EoS, such as $\Delta\epsilon$ and c_{QM}^2, so the contour is vertical. These hybrid stars have a tiny core of the high-density phase and cover a tiny range of masses, of order $10^{-3}M_{solar}$ or less, and so would be very rare.

Disconnected hybrid branches are of special interest, because they give a characteristic signature in mass-radius measurements. For both the hadronic EoSs that I study, the region B and D, where disconnected hybrid star branches can occur, are excluded for $c_{QM}^2 \leq 1/3$. Even for larger c_{QM}^2 disconnected branches only arise if the nuclear matter EoS is sufficiently stiff. It is interesting to note that using an extremely stiff hadronic matter EoS such as DD2-EV can further shrink the region that is excluded by the $M_{max} > 2M_{solar}$ constraint, allowing disconnected branches of hybrid stars to occur.

6.2.3   Minimum radius of hybrid stars

In Fig. 6.4 are shown contour plots of the radius of the maximum-mass star (on either a connected or disconnected hybrid branch) as a function of the CSS quark matter EoS parameters. Since the smallest hybrid star is typically the heaviest one, this allows us to infer the smallest radius that arises from a given EoS. The layout is as in Fig. 6.3: each panel shows dependence on $p_{trans}/\epsilon_{trans}$ and $\Delta\epsilon/\epsilon_{trans}$ for fixed c_{QM}^2; the plots on the left are for $c_{QM}^2 = 1/3$ and the plots on the right are for $c_{QM}^2 = 1$; the plots on the top are for the stiffer DBHF nuclear matter EoS, while the lower plots are for the softer BHF nuclear matter EoS. As in Fig. 6.3, the region that is eliminated by the observation of a $2M_{solar}$ star is shaded in grey.

The smallest stars, with radii as small as $9\,\text{km}$, occur when the high-density phase has the largest possible speed of sound $c_{QM}^2 = 1$. They are disconnected branch stars arising from EoSs having a low transition pressure ($n_{trans} \leq 2n_0$) with a fairly large energy density discontinuity ($\Delta\epsilon/\epsilon_{trans} \geq 1$).
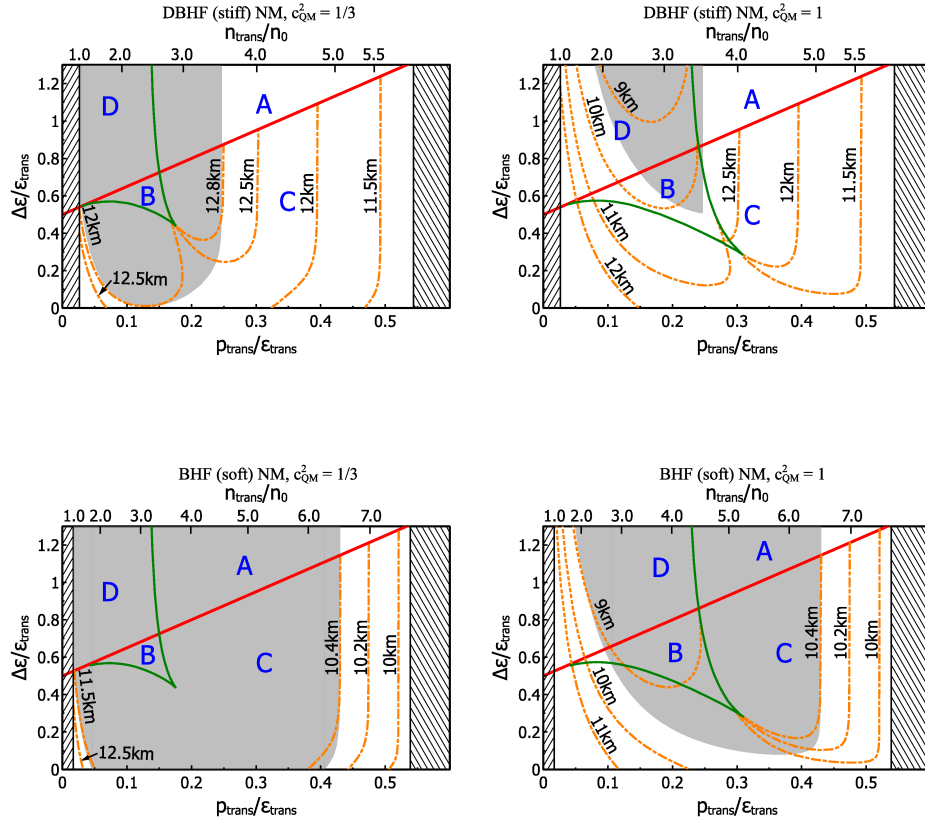
Figure 6.4: Contour plots showing the radius of the maximum-mass star as a function of the CSS parameters. See the text for details.

As in Fig. 6.3, the contours in the high-transition-pressure region are almost vertical because the hybrid branch is then a very short extension to the nuclear mass-radius relation, and its radius is close to that of the heaviest purely hadronic star, which is independent of $\Delta\epsilon/\epsilon_{trans}$ and c_{QM}^2. The radius of the hybrid stars decreases with p_{trans} in this region, because the radius of hadronic stars decreases with central pressure.

For $c_{QM}^2 = 1/3$, the allowed low-transition-pressure region is disconnected from the high-transition-pressure region and is so small that it
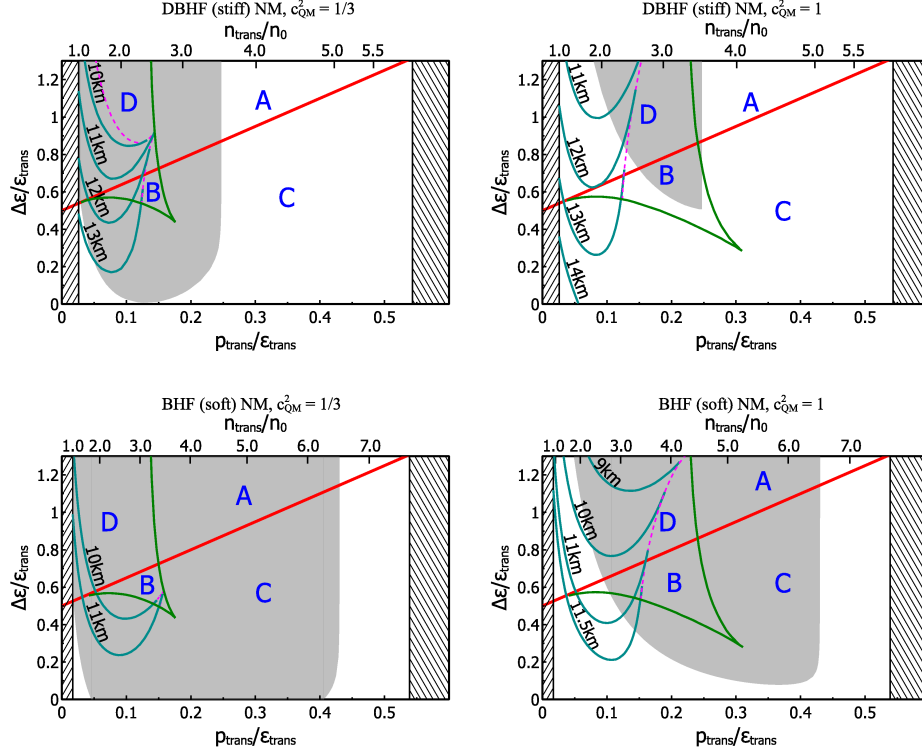
Figure 6.5: Contour plots similar to Fig. 6.4 showing the radius of a hybrid star of mass $M = 1.4\,M_{solar}$ as a function of the CSS parameters. Such stars only exist in a limited region of the space of EoSs [delimited by dashed (magenta) lines]. The grey shaded region is excluded by the observational constraint $M_{max} > 2\,M_{solar}$. For a magnified version of the low-transition-pressure region for $c_{QM}^2 = 1/3$, see Fig. 6.6.

is hard to see on this plot. By magnifying it (left-hand plots of Fig. 6.6) we see that in this region the radius contours closely track the border of the allowed region (the $M_{max} = 2\,M_{solar}$ line) so we can say that the radius must be greater than 11.5 km almost independent of the transition pressure and hadronic EoS. For a stiff hadronic EoS this minimum is raised to 11.7 km. If a star with radius smaller than this minimum value were to be observed, we would have to conclude that either the transition occurs outside the low-density region or that c_{QM}^2 is greater

than 1/3. In the magnified figure I show how the excluded region would grow if a 2.1 M_{solar} star were to be observed (long-dashed line for connected branch stars and short-dashed line for disconnected branch stars). This would increase the minimum radius to about 12.1 km for the soft hadronic EoS and 12.2 km for the stiff hadronic EoS.

6.2.4 Typical radius of hybrid stars

In Fig. 6.5 I show contours (the U-shaped lines) of typical radius of a hybrid star, defined as $R_{1.4}$, the radius of a star of mass 1.4 M_{solar}, as a function of the CSS quark matter EoS parameters. The contours only fill the part of the CSS parameter space where there are hybrid stars with that mass. The dashed (magenta) lines delimit that region which extends only up to moderate transition pressure.

The overall behavior is that, at fixed $\Delta\epsilon/\epsilon_{trans}$, the typical radius is large when the transition density is at its lowest. As the transition density rises the radius of a 1.4 M_{solar} star decreases at first, but then increases again. This is related to the previously noted fact that when one fixes the speed of sound of quark matter and increases the bag constant (which increases $p_{trans}/\epsilon_{trans}$ and also varies $\Delta\epsilon/\epsilon_{trans}$ in a correlated way) the resultant family of mass-radius curves all pass through the same small region in the M-R plane: the $M(R)$ curves "rotate" counterclockwise around this hub. In our case I am varying $p_{trans}/\epsilon_{trans}$ at fixed $\Delta\epsilon/\epsilon_{trans}$, so the hub itself also moves. At low transition density the hub is below 1.4 M_{solar}, so $R_{1.4}$ decreases with $p_{trans}/\epsilon_{trans}$. At high transition density the hub is at a mass above 1.4 M_{solar} so $R_{1.4}$ will increase with $p_{trans}/\epsilon_{trans}$.

The smallest stars occur for $c_{QM}^2 = 1$ (right-hand plots), where $R_{1.4} \geq 9.5 km$ at large values of the energy density discontinuity, and the radius rises as the discontinuity is decreased. This is consistent with the absolute lower bound of about 8.5 km [71] for the maximally

compact $c_{QM}^2 = 1$ star obeying $M_{max} > 2\,M_{solar}$.

For $c_{QM}^2 = 1/3$ the allowed region at low transition pressure is small, so in the right panels of Fig. 6.6 is shown a magnification of this region. I see that in the allowed ($M_{max} > 2\,M_{solar}$ and $n_{trans} > n_0$) region there is a minimum radius $12.2\,km$ for the BHF (soft) hadronic EoS, and about $12.5\,km$ for the DBHF (stiff) hadronic EoS. This minimum is attained at the lowest possible transition density, $n_{trans} \approx n_0$. As the transition density rises to values around $2\,n_0$, the minimum radius rises to 12.5 (BHF) or 13.3 km (DBHF). This is comparable to the minimum radius of about 13 km found in [72], which explored a wider range of hadronic EoSs but assumed $n_{trans} = 2\,n_0$. These results are consistent with the lower bound on $R_{1.4}$ for $c_{QM}^2 = 1/3$ of about 11 km established in [71] using the EoS that yields maximally compact stars (corresponding to CSS with $p_{trans} = 0$ and $c_{QM}^2 = 1/3$) obeying $M_{max} > 2\,M_{solar}$. If a $1.4\,M_{solar}$ star were observed to have radius below the minimum value, one would have to conclude that either it is not a hybrid star or that $c_{QM}^2 > 1/3$.

The dashed line shows how the excluded region would grow if a star of mass $2.1\,M_{solar}$ were to be observed. This would increase the minimum radius to about 12.7 (BHF) or 13 km (DBHF).

6.3 The Field Correlator Method (FCM) EoS

The approach based on the FCM provides a natural treatment of the dynamics of confinement in terms of the color electric (D^E and D_1^E) and color magnetic (D^H and D_1^H) Gaussian correlators, the former being directly related to confinement, so that its vanishing above the critical temperature implies deconfinement. The EoSs used in this Section are the microscopic BHF with phenomenological three body forces and the
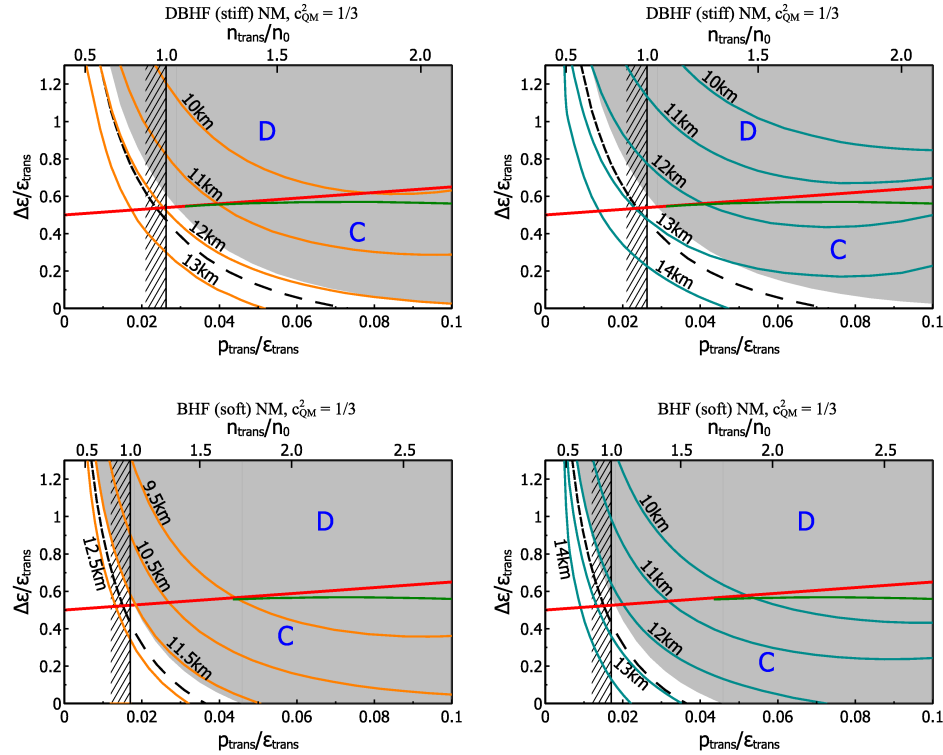
Figure 6.6: Magnified version of the $c_{QM}^2 = 1/3$ plots in Figs. 6.4 –6.5. See the text for details.

DBHF [73]. The extension of the FCM to finite temperature T at chemical potential $\mu_q = 0$ gives analytical results in reasonable agreement with lattice data, giving us some confidence that it correctly describes the deconfinement phase transition [74, 75]. In order to derive an EoS of the quark-gluon matter in the range of baryon density typical of the neutron star interiors, we have to extend the FCM to nonzero chemical potential [74, 75]. In this case, the quark pressure for a single flavor is simply given by

$$P_q/T^4 = \frac{1}{\pi^2}\left[\phi_\nu\left(\frac{\mu_q - V_1/2}{T}\right) + \phi_\nu\left(-\frac{\mu_q + V_1/2}{T}\right)\right] \qquad (6.3)$$

where

$$\phi_\nu(a) = \int_0^\infty du \left(u^4/\sqrt{u^2+\nu^2} \right) \left(\exp\left[\sqrt{u^2+\nu^2} - a \right] + 1 \right)^{-1} \quad (6.4)$$

with $\nu = m_q/T$, and V_1 is the large distance static $\bar{q}q$ potential whose value at zero chemical potential and temperature is $V_1(T=\mu_B=0) = 0.8$ to $0.9\,\text{GeV}$ [76]. The gluon contribution to the pressure is

$$P_g/T^4 = \frac{8}{3\pi^2} \int_0^\infty d\chi \chi^3 \frac{1}{\exp\left(\chi + \frac{9V_1}{8T}\right) - 1} \quad (6.5)$$

and the total pressure is

$$P_{qg} = \sum_{j=u,d,s} P_q^j + P_g - \frac{(11 - \frac{2}{3}N_f)}{32} \frac{G_2}{2} \quad (6.6)$$

where P_q^j and P_g are given in Eqs. (6.3) and (6.5), and N_f is the number of flavors. The last term in Eq. (6.6) corresponds to the difference of the vacuum energy density in the two phases, G_2 being the gluon condensate whose numerical value, determined by the QCD sum rules at zero temperature and chemical potential, is known with large uncertainty, $G_2 = 0.012 \pm 0.006\,GeV^4$. At finite temperature and vanishing baryon density, a comparison with the recent available lattice calculations provides clear indications about the specific values of these two parameters, and in particular their values at the critical temperature T_c. Some lattice simulations suggest no dependence of V_1 on μ_B, at least for very small μ_B, while different analyses suggest a linear decreasing of G_2 with the baryon density ρ_B [77], in nuclear matter. However, for simplicity, in the following I treat both V_1 and G_2 as numerical parameters with no dependence on μ_B.

6.3.1 The FCM EoS and the CSS parametrization

The CSS parametrization will be applicable to the FCM EoS if the speed of sound in the FCM EoS depends only weakly on the density

or pressure. In Fig. 6.7 I show that this is indeed the case. The upper panel shows the speed of sound vs. pressure in the FCM quark matter EoS for different values of the FCM parameters, displayed in the lower panel. I see that the speed of sound varies by less than 5% over the considered range of pressures along each curve, and lies in the interval $0.28 < c_{QM}^2 < 1/3$. The value of c_{QM}^2 shows a weak dependence on V_1 and extremely weak dependence on G_2, which appears as an additive constant in the quark matter EoS according to Eq. (6.6). The transition pressure is more sensitive to the FCM parameters, increasing rapidly with V_1 and with G_2. The energy density at a given pressure increases slightly with an increase in V_1 or G_2.
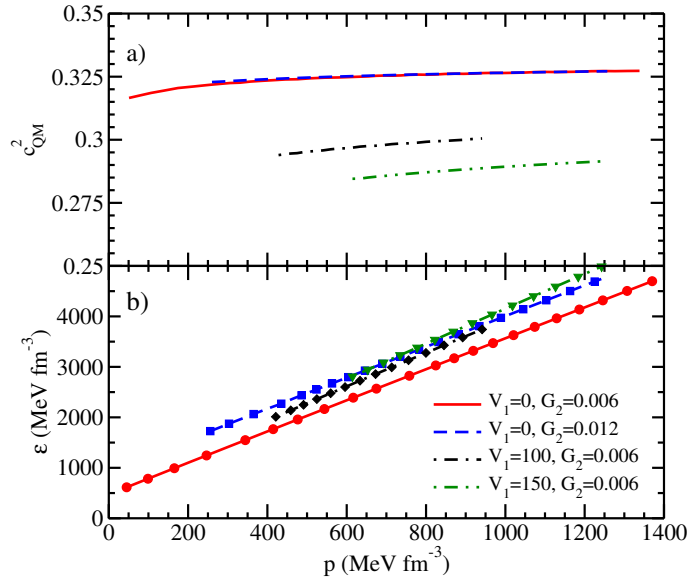

Figure 6.7: The squared speed of sound c_{QM}^2 [panel (a)] is displayed vs quark matter pressure for several values of V_1 (in MeV) and G_2 (in GeV^4). In panel (b), the FCM energy density is represented by full symbols, whereas the full lines denote the CSS parametrization given by Eq. (6.1).

To illustrate how well the CSS parametrization fits the FCM EoS, I show in the lower panel of Fig. 6.7 that, for the same FCM parameter
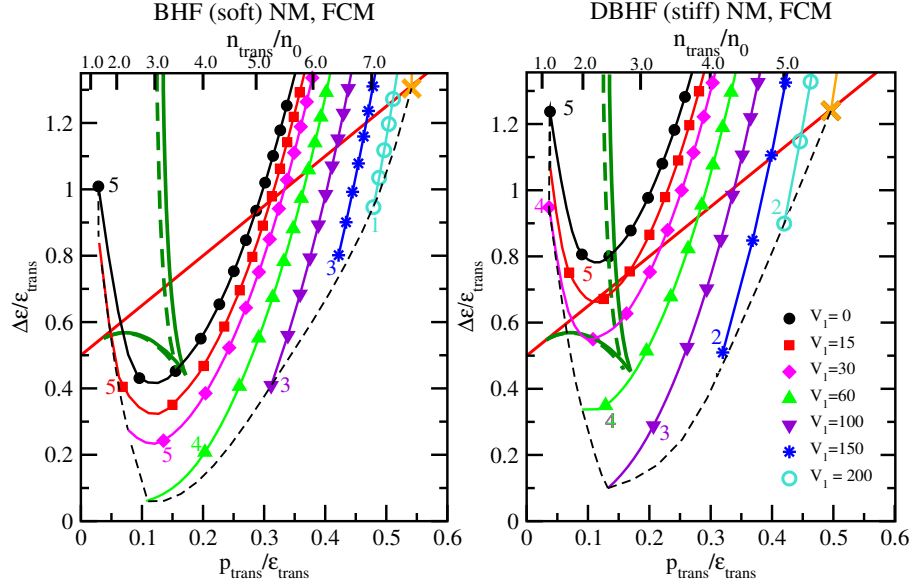
Figure 6.8: The mapping of the FCM quark matter model onto the CSS parametrization. Results are obtained using the BHF (left panel) and DBHF (right panel) nuclear matter EoS. See the text for details.

choices, we can always find suitable values of the CSS parameters which fit the FCM calculation extremely well. This means that there exists a well-defined mapping between the FCM parameters (V_1, G_2) and the CSS parameters ($p_{trans}/\epsilon_{trans}$, $\Delta\epsilon/\epsilon_{trans}$, c_{QM}^2). Note that the mapping depends on the EoS of the hadronic matter.

The mapping is displayed in Fig. 6.8, which shows the region of the CSS parameter space where FCM equations of state are found. It is shown in this figure the plane whose coordinates are the CSS parameters $\Delta\epsilon/\epsilon_{trans}$ and $p_{trans}/\epsilon_{trans}$. For the hadronic EoS I use BHF (left panel)
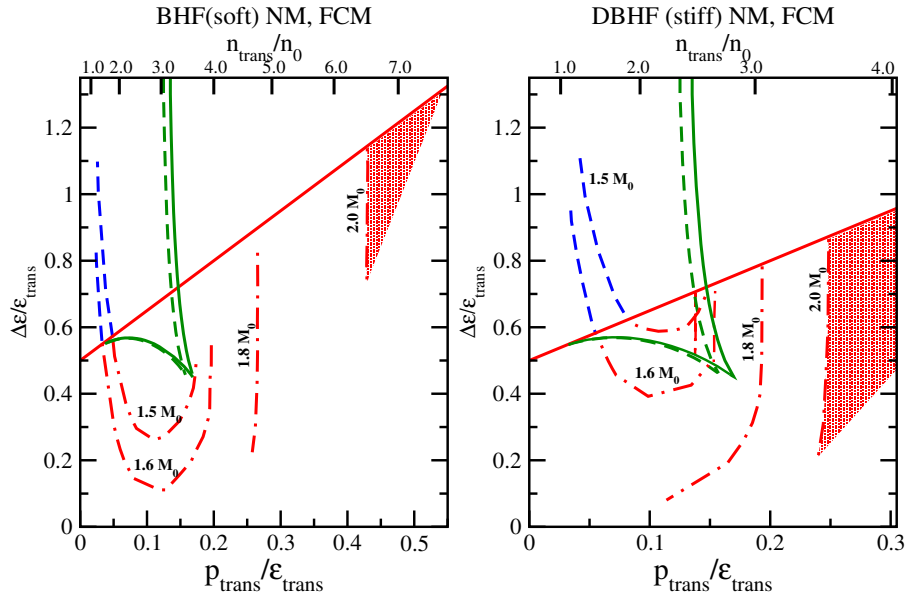
Figure 6.9: Contour plots, analogous to Fig. 6.3, showing the maximum mass of hybrid stars with FCM quark matter cores, given in terms of the corresponding CSS parameter values rather than the original FCM parameter values. See the text for details.

and DBHF (right panel). The lines without points represent the phase boundaries, as for the figures in Sec. 6.2, for connected and disconnected branches. Whether a given FCM EoS yields stable hybrid stars depends on which of those phase regions (see Fig. 6.2) it is in. The solid (green) phase boundary with a cusp at $p_{trans}/\epsilon_{trans} \approx 0.17$ delimits the region with a disconnected branch for $c_{QM}^2 = 1/3$, while the nearby dashed (green) line is for $c_{QM}^2 = 0.28$, so these span the range of c_{QM}^2 relevant for the FCM, as discussed in Fig. 6.7. It is evident that the dependence
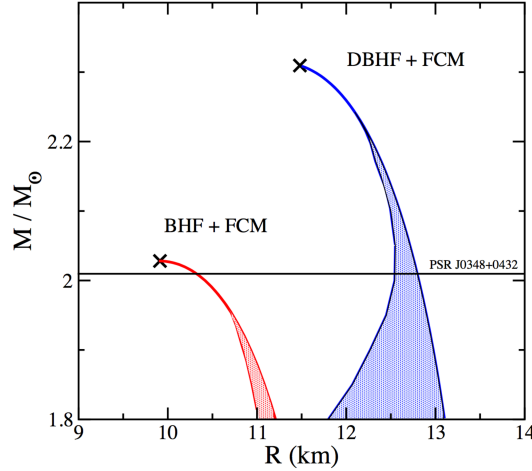
Figure 6.10: Shaded areas show range of radii of stars with a given maximum mass when varying FCM parameters. The thick dashed lines indicate the purely hadronic mass-radius configurations. The crosses at the top of the shaded regions correspond to the maximal configuration indicated by the same symbol in Fig. 6.8. The observational constraint [6] on the star mass is indicated by a horizontal line.

on c_{QM}^2 is tiny and negligible for practical purposes.

The thin dashed (black) line and the solid (black) line studded with circles delimit the equations of state yielded by the FCM calculation. Within that region, the lines studded with points show the CSS parametrization of the FCM quark matter EoS, where along each line I keep V_1 constant and vary G_2. Above that region, which corresponds to negative values of V_1, the EoS cannot reproduce the $2\,M_{solar}$ limit, and in this sense is unphysical (Fig. 6.9). Below that region, there would be no transition from hadronic to quark matter, as explained below.

In Fig. 6.8, V_1 varies from 0 up to the maximum value at which hybrid star configurations occur, which is indicated by an (orange) cross. For the BHF case that value is $V_1 = 240\;MeV$, $G_2 = 0.0024\;GeV^4$

and for the DBHF case it is $V_1 = 255\ MeV$, $G_2 = 0.0019\ GeV^4$. Along each FCM curve in Fig. 6.8 the parameter G_2 starts at the minimum value at which there is a phase transition from hadronic to FCM quark matter; at lower G_2 the quark and the hadronic pressures $p(\mu)$ do not cross at any μ. On each curve one point is labeled with its value of $G_2/(10^{-3}\,\mathrm{GeV^4})$, and subsequent points are at intervals where G_2 increases in increments of 1 in the same units. I observe that along each line of constant V_1, $p_{trans}/\epsilon_{trans}$ grows with G_2. This can be explained by recalling the linear dependence of the quark pressure on G_2 in Eq. (6.6), so that, at fixed chemical potential, an increase of G_2 lowers the quark pressure, making quark matter less favorable, and shifting the transition point to higher chemical potential or pressure. This is equally applicable to DBHF nuclear matter. Obviously if G_2 becomes too small, the phase transition takes place in a region of low densities where finite nuclei are present, and the homogeneous nuclear matter approach becomes invalid. The qualitative behaviour of the curves of constant V_1 can be understood in terms of the Maxwell construction between the purely hadronic phase and the quark phase. The fact that $\Delta\epsilon/\epsilon_{trans}$ goes through a minimum (which is always at $p_{trans}/\epsilon_{trans} \approx 0.1$) as G_2 is increased at constant V_1 can be understood from Fig. 2 of [78], which shows pressure p as a function of baryon density n and the location of the hadron (BHF EoS) to quark (FCM EoS) transition when G_2 is varied. The hadronic EoS is strongly curved, especially at low pressure, while the FCM EoS is closer to a straight line. Consequently, the baryon density difference between the two phases at a given pressure has a minimum at densities around $2\,n_0$, which corresponds to $p_{trans}/\epsilon_{trans} \approx 0.1$. As G_2 increases, the transition pressure rises, scanning through this minimum. It follows that the energy density difference also goes through a minimum, because $\epsilon = \mu n - p$, and p and μ are continuous at the transition, so $\Delta\epsilon = \mu\Delta n$. The DBHF

hadronic EoS is very similar to BHF at low pressure, so the curves have their minima at the same value of $p_{trans}/\epsilon_{trans}$ in both panels of Fig. 6.8. We can also see in Fig. 6.8 that an increase of V_1 moves the curves slightly downward and to the right. This is expected since V_1 is a measure of the interparticle strength, and is inversely proportional to the pressure of the system, so that the pressure decreases as V_1 is increased at fixed μ, and, as already discussed for the parameter G_2, a decrease of the quark pressure raises p_{trans}. The role of V_1 and G_2 in the quark EoS discussed so far, provides in the same way a qualitative understanding of c_{QM}^2 in panel (a) of Fig. 6.7, although, as already noticed, the effect in Fig. 6.8 of the change in c_{QM}^2 is negligible.

6.3.2   Expected properties of mass-radius curves

By comparing Fig. 6.8 with Fig. 6.2 we can see that when combining FCM quark matter with BHF (soft) nuclear matter, the physically allowed range of FCM parameter values yields EoSs that are mostly in regions C and A, where there is no disconnected hybrid branch. At the lowest transition densities the FCM EoS can achieve a large enough energy density discontinuity to yield a disconnected branch (region D). For the DBHF (stiff) nuclear EoS there is a wider range of values of V_1 and G_2 that give disconnected branches, and some of them give simultaneous connected and disconnected branches. This difference can be understood in terms of the stiffness of the EoSs. A change from a soft hadronic EoS (BHF) to a stiff one (DBHF) produces a steeper growth of the hadronic pressure as a function of the baryon density. Referring again to Fig. 2 of [78], this pulls the DBHF [79] $p(n)$ curve further away from the FCM curve, giving a larger difference in baryon density at a given pressure, and hence, as noted above, a larger $\Delta\epsilon$. This is why the curves for DBHF+FCM (right panel of Fig 6.8) are shifted upwards along the $\Delta\epsilon/\epsilon_{trans}$ axis compared to the BHF+FCM curves (left panel

of Fig. 6.8). We can calculate the maximum mass of a hybrid star containing a FCM core as a function of the FCM parameters, and then use the mapping described above to obtain the CSS parameter values for each FCM EoS, producing a contour plot of maximum mass (Fig. 6.9) for BHF (left panel) and DBHF (right panel) hadronic EoS. Given that the CSS parametrization is a fairly accurate representation of the FCM EoS, one would expect this to be very similar to the corresponding plot for CSS itself with $c_{QM}^2 = 1/3$ (Fig. 6.3), and this is indeed the case. The contours in Fig. 6.9 are restricted to the region corresponding to physically allowed FCM parameter values, so they end at the edges of that region.

The triangular shaded area at the edge of each panel shows the region of the parameter space that is accessible by the FCM and is consistent with the measurement of a $2 M_{solar}$, by having hybrid stars of maximum mass greater than $2 M_{solar}$. The (orange) cross in each panel of Fig. 6.8 is at the high-transition-pressure corner of that triangular area. The heaviest BHF+FCM hybrid star has a mass of $2.03 M_{solar}$, and the heaviest DBHF+FCM hybrid star has a mass of $2.31 M_{solar}$.

As noted in Sec. 6.2.2, the hybrid stars in this physically allowed and FCM-compatible region of the phase diagram lie on a very tiny connected branch, covering a very small range of central pressures and masses and radii, and would therefore occur only rarely in nature. These stars have very small quark matter cores [15], and their mass and radius are very similar to those of the heaviest purely hadronic star, but there could be other clear signatures of the presence of the quark matter core, such as different cooling behavior.

The CSS parametrization has another region where heavy hybrid stars occur, at low transition pressure (see Fig. 6.3), but the FCM does not predict that the quark matter EoS could be in that region.

To characterize the radius of FCM hybrid stars we cannot construct

contour plots like Fig. 6.5 because, as we have just seen, the FCM predicts that only hybrid stars with mass very close to the maximum mass are allowed. There are no FCM hybrid stars with mass around $1.4\,M_{solar}$. Instead, in Fig. 6.10 I show the range of radii of stars with a given maximum mass when varying FCM parameters, for our two different hadronic EoSs. The right-hand edge of each shaded region traces out the mass-radius relation for hadronic stars with the corresponding hadronic EoS. The FCM hybrid stars form very small connected branches which connect to the nuclear matter where the central pressure reaches the transition pressure (see Sec. 6.2.2), so the hybrid stars do not deviate very far from the hadronic mass-radius curve. Hence the shaded regions in Fig. 6.10 are narrow, especially in the observationally allowed ($M_{max} > 2\,M_{solar}$) region, which perfectly matches the prediction of CSS parametrization on the maximum-mass star radius in the high-transition-pressure region (see the left panels of Fig. 6.4). For BHF (soft) nuclear matter, the hadronic stars, and hence the hybrid stars, are smaller because the nuclear mantle is more compressed by the self gravitation of the star.

Chapter 7

Summary and Outlook

I have presented a systematic confrontation of the nuclear Equation of State, obtained within different microscopic many-body methods, with the available constraints coming from phenomenology. The latter are extracted from laboratory experiments as well as from astrophysical observations. Both nuclear structure and heavy ion collisions data were considered, along the same lines of the analysis on the Skyrme forces reported in [50]. Astrophysical observational data included the measures of NS masses, some hints on the radius-mass relation from [45, 46] and the constraints on the EoS presented in [47], obtained from the analysis of transient phenomena in six NS's. Some theoretical constraints, as the requirement of a sub-luminal speed of sound, were also considered. If one takes literally all the constraints, among the considered microscopic EoS only one passes all the tests, namely the one with phenomenological three body forces. However, these phenomenological constraints are affected by uncertainties, which are difficult to estimate quantitatively on a firm basis. The conclusion that one can draw from this analysis is twofold. Firstly, despite the differences between the considered microscopic EoS, their overall predictions do not show major discrepancies with one another as well as with the phenomenological constraints. In other words, the calculated microscopic nuclear EoS, based on different many-body methods, are not in contradiction with the phenomenological constraints. This is not at all an obvious result. Secondly, from the analysis it appears that one can explain reasonably well all the data with a microscopic EoS that includes only nucleonic degrees of freedom, in particular no exotic components in NS are needed.

I have also computed nucleon effective masses in the BHF formalism for dense nuclear matter, employing different combinations of two-nucleon and three-nucleon forces. Useful parametrizations of the numerical results were provided. The relevant in-medium correction fac-

tors for several neutrino emission processes in β-stable non-superfluid neutron star matter have then been evaluated in a consistent manner. I find in general in-medium suppression of the emissivities, which however depends strongly on the employed interactions, and reflect mainly the current lack of knowledge regarding nuclear TBF at high density. This emphasizes the need of performing and comparing consistent calculations with given sets of two-body and three-body interactions. This is important for the study of cooling. Infact I have studied NS cooling using a microscopic BHF EOS featuring strong direct Urca reactions setting in at $\rho = 0.44\ fm^{-3}$, M/M$_\odot$ > 1.10, and using compatible p1S0 and n3P2 pairing gaps as well as nucleon effective masses. The current substantial theoretical uncertainty regarding gaps and thermal conductivity was modelled in a rather simple way by introducing three global scale factors.

I found that it is possible to reproduce the apparent fast cooling of Cas A by either finetuning the n3P2 pairing gap or reducing the thermal conductivity. In general it is difficult to then simultaneously fit old hot NS, although I did find a suitable parameter set for that purpose.

Relaxing the Cas A constraint, it is astonishing to see how well all current cooling data can be fit by just assuming the p1S0 BCS gap (with some freedom of scaling) and a vanishing n3P2 gap.

My results affirm the extreme difficulty to draw quantitative conclusions from the current NS cooling data containing no information on the masses of the cooling objects, due to the large variety of required microphysics input that is hardly known or constrained otherwise.

I have shown that not even the combination of very strong DU cooling in combination with sufficiently large and extended p1S0 gaps and small n3P2 pairing gaps can be excluded. There is still ample freedom to choose the magnitude and shape of the p1S0 gap, as long as the cov-

ered density domain is sufficiently large. One can only hope to resolve this problem once precise information on the NS masses in the cooling diagram becomes available. Even more exotic possibilities of blocking the DU process by strong p3P2 pairing are not excluded either, but were not analyzed in this thesis; as neither the effect of exotic components of matter (hyperons, quarks) that should appear at high density and completely change the theoretical picture. In any case there are strong indications from theoretical many-body calculations and supported by the current analysis, that the DU process becomes active at moderately high baryon density; it should thus never be excluded without justification in cooling simulations.

Finally, as an application to a specific model, I performed calculations for the FCM quark matter EoS. I showed that the FCM equation of state can be accurately represented by the CSS parametrization, and I displayed the mapping between the FCM and CSS parameters. I found that FCM quark matter has a speed of sound in a narrow range around $c_{QM}^2 = 0.3$, and the FCM family of EoSs covers a limited region of the space of all possible EoSs. Once the observational constraint $M_{\max} > 2\mathrm{M}_\odot$ is taken into account, the allowed region in the parameter space is drastically reduced. This corresponds to the high-transition-pressure scenario, with a small connected branch of hybrid stars with tiny quark matter cores. Such stars would be hard to distinguish from hadronic stars via mass and radius measurements, but the quark matter core could be detectable via other signatures, such as cooling behavior. These hybrid stars have central densities larger than $6.5\,n_0$ in the BHF case, and $3.5\,n_0$ in the DBHF case which means that hyperons could play an important role in the BHF case, and they cannot be ruled out even in the relativistic DBHF case. However, as discussed previously, in this thesis I ignored hyperons because I am already using two different hadronic EoSs, one stiff and one soft, to estimate the sen-

sitivity of my results to the hadronic EoS, and the effect of hyperons remains unknown. Moreover, as far as we know, the introduction of hyperons softens dramatically the EoS which is therefore excluded by the observational data [80]. In the future one can expect that the interplay between theory and observations will continue to play a major role in the worldwide effort of determining the nuclear EoS, including the hyperonic contribution.

From the end of January 2016 I will carry on my project at the Nicolaus Copernicus Institute in Warsaw in collaboration with Prof. P. Haensel and his group focusing my research on the cooling of binary systems.

Acknowledgments

Foremost, I would like to express my deepest gratitude to my advisor, Professor Fiorella Burgio, for her guidance and support throughout my PhD studies at the University of Catania. Her patience, enthusiasm and immense knowledge have helped me enormously in improving my research skills as a scientist. Whenever I needed a discussion or an advice, she was always ready to hear me with thoughtful insights in an articulate manner. I feel very fortunate to have had the opportunity to work with such a wonderful, supportive advisor. A special thanks goes to my official advisor Vincenzo Greco. Next, my thanks go to the other members of my research group namely Hans Joseph Schulze who supported me during these years and Marcello Baldo. Their wisdom and their precious advices are been very important for me. I am also grateful to Dario Zappalà for his collaboration and for the numerous discussions we have had on my research. I would like to aknowledge the "NewCompStar" (COST Action MP1304) and INFN (Section of Catania) for supporting my research . I would like to extend my appreciation to my friend and colleague Armando Puglisi for providing technical advices and comments on parts of my life as a PhD student. I am thankful to all of my other friends especially to Nicolò Demarco, Vittorio Verdi, Riccardo Scuto, Mario Buscemi, Gianluca Santagati, Gianluca Messina, Corrado Ratto, Giuliano Mazzoccante, for their friendship and support. Last, and most importantly, I would like to thank

Bibliography

[1] D. G. Yakovlev, P. Haensel, G. Baym, and C. J. Pethick. Lev Landau and the concept of neutron stars. *Phys. Usp.*, 56:289–295, 2013. [Usp. Fiz. Nauk183,307(2013)].

[2] Lev D. Landau. On the theory of stars. *Phys. Z. Sowjetunion*, 1:285, 1932.

[3] F. Burgio. Private notes. 2011.

[4] Notes from the International School in Seattle. Nuclear physics of neutron stars and supernovae. 2015.

[5] P. Demorest, T. Pennucci, S. Ransom, M. Roberts, and J. Hessels. Shapiro Delay Measurement of A Two Solar Mass Neutron Star. *Nature*, 467:1081–1083, 2010.

[6] J. Antoniadis, P.C. Freire, N. Wex, T.M. Tauris, R.S. Lynch, and et al. A Massive Pulsar in a Compact Relativistic Binary. *Science*, 340:1233232, 2013.

[7] S. Guillot, M. Servillat, N. A. Webb, and R. E. Rutledge. Measurement of the Radius of Neutron Stars with High S/N Quiescent Low-mass X-ray Binaries in Globular Clusters. *Astrophys. J.*, 772:7, 2013.

[8] http://heasarc.gsfc.nasa.gov/docs/nicer/.

[9] G. Taranto, M. Baldo, and G.F. Burgio. Selecting microscopic Equations of State. *Phys.Rev.*, C87:045803, 2013.

[10] T. Klahn et al. Constraints on the high-density nuclear equation of state from the phenomenology of compact stars and heavy-ion collisions. *Phys. Rev.*, C74:035802, 2006.

[11] M. Baldo, G. F. Burgio, H. J. Schulze, and G. Taranto. Nucleon effective masses within the Brueckner-Hartree-Fock theory: Impact on stellar neutrino emission. *Phys. Rev.*, C89(4):048801, 2014.

[12] G. Taranto, G. F. Burgio, and H. J. Schulze. Cassiopeia A and direct URCA cooling. 2015. ARXIV:1511.04243.

[13] K. G. Elshamouty, C. O. Heinke, G. R. Sivakoff, W. C. G. Ho, P. S. Shternin, D. G. Yakovlev, D. J. Patnaude, and L. David. Measuring the Cooling of the Neutron Star in Cassiopeia A with all Chandra X-Ray Observatory Detectors. *Astrophys. J.*, 777:22, 2013.

[14] Wynn C. G. Ho, Khaled G. Elshamouty, Craig O. Heinke, and Alexander Y. Potekhin. Tests of the nuclear equation of state and superfluid and superconducting gaps using the Cassiopeia A neutron star. *Phys. Rev.*, C91(1):015806, 2015.

[15] M. G. Alford, S. Han, and M. Prakash. Generic conditions for stable hybrid stars. *Phys.Rev.*, D88(8):083013, 2013.

[16] M. G. Alford, G. F. Burgio, S. Han, G. Taranto, and D. Zappalà. Constraining and applying a generic high-density equation of state. *Phys. Rev.*, D92(8):083002, 2015.

[17] https://en.wikipedia.org/wiki/Francesco_Maurolico.

[18] T. Papenbrock and H. Weidenmueller. Effective Field Theory for Finite Systems with Spontaneously Broken Symmetry. *Phys. Rev. C, 89:014334*, 2014.

[19] M. Baldo and G. F. Burgio. Properties of the nuclear medium. *Rep. Prog. Phys. 75 026301*, 2012.

[20] V. R. Pandharipande and R. B. Wiringa. Variations on a theme of nuclear matter. *Rev. Mod. Phys.*, 51:821–859, 1979.

[21] J. Navarro, R. Guardiola, and I. Moliner. Introduction to Modern Methods of Quantum Many-Body Theory and their Applications. World Scientific, Singapore, 2002.

[22] A. Akmal, V. R. Pandharipande, and D. G. Ravenhall. The Equation of state of nucleon matter and neutron star structure. *Phys. Rev.*, C58:1804–1828, 1998.

[23] R. B. Wiringa, V. G. J. Stoks, and R. Schiavilla. An Accurate nucleon-nucleon potential with charge independence breaking. *Phys. Rev.*, C51:38–51, 1995.

[24] R. B. Wiringa, R. A. Smith, and T. L. Ainsworth. Nucleon Nucleon Potentials with and without Delta (1232) degrees of freedom. *Phys. Rev.*, C29:1207–1221, 1984.

[25] M. Naghdi. Nucleon-nucleon interaction: A typical concise review. *Phys. Part. Nucl. 45, 924-971*, 2014.

[26] M. Baldo. Nuclear methods and the nuclear equation of state. *International Review of Nuclear Physics - Vol 8*, 1999.

[27] M. Baldo, I. Bombaci, and G. F. Burgio. Microscopic nuclear equation of state with three-body forces and neutron star structure. *Astron. Astrophys.*, 328:274–282, 1997.

[28] S. L. Shapiro and S. A. Teukolsky. *Black holes, white dwarfs, and neutron stars: The physics of compact objects.* 1983.

[29] P. Danielewicz, R. Lacey, and William G. Lynch. Determination of the equation of state of dense matter. *Science*, 298:1592–1596, 2002.

[30] C. Fuchs. Kaon production in heavy ion reactions at intermediate energies. *Prog. Part. Nucl. Phys. 56, 1*, 2006.

[31] M. B. Tsang et al. Constraints on the symmetry energy and neutron skins from experiments and theory. *Phys. Rev.*, C86:015803, 2012.

[32] Danielewicz and Lee. private communication.

[33] M. A. Famiano, T. Liu, W. G. Lynch, A. M. Rogers, M. B. Tsang, M. S. Wallace, R. J. Charity, S. Komarov, D. G. Sarantites, and L. G. Sobotka. Neutron and Proton Transverse Emission Ratio Measurements and the Density Dependence of the Asymmetry Term of the Nuclear Equation of State. *Phys. Rev. Lett.*, 97:052701, 2006.

[34] M. B. Tsang et al. Isoscaling in statistical models. *Phys. Rev.*, C64:054615, 2001.

[35] T. X. Liu et al. Isospin Diffusion Observables in heavy ion reactions. *Phys. Rev.*, C76:034603, 2007.

[36] Z. Y. Sun et al. Isospin Diffusion and Equilibration for Sn+Sn collisions at E/A=35 MeV. *Phys. Rev.*, C82:051603, 2010.

[37] Z. Kohley et al. Transverse collective flow and midrapidity emission of isotopically identified light charged particles. *Phys. Rev.*, C83:044601, 2011.

[38] P. Møller, W. D. Myers, H Sagawa, and S Yoshida. *Phys. Rev. Lett.*, 108:052501, 2012.

[39] C. J. Horowitz, S. J. Pollock, P. A. Souder, and R. Michaels. Parity violating measurements of neutron densities. *Phys. Rev.*, C63:025501, 2001.

[40] C. J. Horowitz. Parity violating elastic electron scattering and Coulomb distortions. *Phys. Rev.*, C57:3430–3436, 1998.

[41] P. A. Souder, R. J. Holmes, et al. PREX II experimental proposal to Jefferson Laboratory, PAC38. *http://hallaweb.jlab.org/parity/prex/prexII.pdf*.

[42] J. Zenihiro et al. Neutron density distributions of Pb-204, Pb-206, Pb-208 deduced via proton elastic scattering at Ep=295 MeV. *Phys. Rev.*, C82:044611, 2010.

[43] A. Klimkiewicz et al. Nuclear symmetry energy and neutron skins derived from pygmy dipole resonances. *Phys. Rev.*, C76:051603, 2007.

[44] A. Carbone, G. Colo, A. Bracco, L.G. Cao, P.F. Bortignon, F. Camera, and O. Wieland. Constraints on the symmetry energy and on neutron skins from the pygmy resonances in 68Ni and 132Sn. *Phys. Rev.*, C81:041301, 2010.

[45] F. Özel. Surface Emission from Neutron Stars and Implications for the Physics of their Interiors. *Rept. Prog. Phys.*, 76:016901, 2013.

[46] T. Guver and F. Özel. The mass and the radius of the neutron star in the transient low mass X-ray binary SAX J1748.9-2021. *Astrophys. J.*, 765:L1, 2013.

[47] A. W. Steiner, J. M. Lattimer, and E. F. Brown. The Equation of State from Observed Masses and Radii of Neutron Stars. *Astrophys. J.*, 722:33–54, 2010.

[48] P. Podsiadlowski, J. D. M. Dewi, P. Lesaffre, J. C. Miller, W. G. Newton, and J. R. Stone. The Double pulsar J0737-3039: Testing the neutron star equation of state. *Mon. Not. Roy. Astron. Soc.*, 361:1243–1249, 2005.

[49] F. S. Kitaura, H.T. Janka, and W. Hillebrandt. Explosions of O-Ne-Mg cores, the Crab supernova, and subluminous type II-P supernovae. *Astron. Astrophys.*, 450:345–350, 2006.

[50] M. Dutra, O. Laurenço, et al. *Phys. Rev. C 85, 035201*, 2012.

[51] F. Weber D. Page, U Geppert. The cooling of compact stars. *Nucl.Phys.A777:497-530*, 2006.

[52] D. Darling. Urca process. *The Internet Encyclopedia of Science. Retrieved 2010-03-02.*

[53] P. Grangè, A. Lejeune, M. Martzolff, and J. F. Mathiot. Consistent Three Nucleon Forces in the Nuclear Many Body Problem. *Phys. Rev.*, C40:1040–1060, 1989.

[54] W. Zuo, U. Lombardo, H. J. Schulze, and Z. H. Li. Three-body force rearrangement effect on single particle properties in neutron-rich nuclear matter. *Phys. Rev.*, C74:014317, 2006.

[55] D. G. Yakovlev, A. D. Kaminker, Ø. Y. Gnedin, and P. Haensel. Neutrino emission from neutron stars. *Phys. Rept.*, 354:1, 2001.

[56] B. L. Friman and O. V. Maxwell. Neutron Star Neutrino Emissivities. *Astrophys. J.*, 232:541–557, 1979.

[57] P. Yin and W. Zuo. Three-body force effect on neutrino emissivities of neutron stars within the framework of the Brueckner-Hartree-Fock approach. *Phys. Rev.*, C88(1):015804, 2013.

[58] D. Page and S. Reddy. Dense Matter in Compact Stars: Theoretical Developments and Observational Constraints. *Annual Review of Nuclear and Particle Science*, 56:327–374, 2006.

[59] Wynn C. G. Ho and Craig O. Heinke. A Neutron Star with a Carbon Atmosphere in the Cassiopeia A Supernova Remnant. *Nature*, 462:71–73, 2009.

[60] Craig O. Heinke and Wynn C. G. Ho. Direct Observation of the Cooling of the Cassiopeia A Neutron Star. *Astrophys. J.*, 719:L167–L171, 2010.

[61] P. S. Shternin and D. G. Yakovlev. A young cooling neutron star in the remnant of Supernova 1987A. *Astronomicheskii Zhurnal*, 34:675–685, 2008.

[62] M. Baldo, J. Cugnon, A. Lejeune, and U. Lombardo. Proton and neutron superfluidity in neutron star matter. *Nuclear Physics A*, 536:349–365, 1992.

[63] Ø. Elgarøy, L. Engvik, M. Hjorth-Jensen, and E. Osnes. Triplet pairing of neutrons in β-stable neutron star matter. *Nuclear Physic A*, 607:425–441, 1996.

[64] M. Baldo and H.-J. Schulze. Proton pairing in neutron stars. *Physical Review C*, 75(2):025802, 2007.

[65] D. Page. http://www.astroscu.unam.mx/neutrones/dany.html. 2010.

[66] H. Grigorian and D. N. Voskresensky. Medium effects in cooling of neutron stars and 3P(2) neutron gap. *Astron. Astrophys.*, 444:913, 2005.

[67] D. Blaschke, H. Grigorian, D. N. Voskresensky, and F. Weber. On the Cooling of the Neutron Star in Cassiopeia A. *Phys. Rev.*, C85:022802, 2012.

[68] D. Blaschke, H. Grigorian, and D. N. Voskresensky. Nuclear medium cooling scenario in the light of new Cas A cooling data and the $2M_{\odot}$ pulsar mass measurements. *Phys. Rev.*, C88(6):065805, 2013.

[69] L. Lindblom. Phase transitions and the mass radius curves of relativistic stars. *Phys.Rev.*, D58:024008, 1998.

[70] T. Gross-Boelting, C. Fuchs, and A. Faessler. Covariant representations of the relativistic Bruckner T matrix and the nuclear matter problem. *Nucl. Phys. A*, 648:105–137, 1999.

[71] J. M. Lattimer. The nuclear equation of state and neutron star masses. *Ann.Rev.Nucl.Part.Sci.*, 62:485–515, 2012.

[72] P. Bedaque and A. W. Steiner. Sound velocity bound and neutron stars. *Phys. Rev. Lett. 114 031103*, 2015.

[73] A. Di Giacomo, H. G. Dosch, V.I. Shevchenko, and Yu.A. Simonov. Field correlators in QCD: Theory and applications. *Phys.Rept.*, 372:319–368, 2002.

[74] Yu.A. Simonov and M.A. Trusov. Deconfinement transition for nonzero baryon density in the field correlator method. *JETP Lett.*, 85:598–601, 2007.

[75] Yu.A. Simonov and M.A. Trusov. Vacuum phase transition at nonzero baryon density. *Phys.Lett.*, B650:36–40, 2007.

[76] S. Plumari, G.F. Burgio, V. Greco, and D. Zappalà. Quark matter in Neutron Stars within the Field Correlator Method. *Phys.Rev.*, D88(8):083005, 2013.

[77] M. Baldo, P. Castorina, and D. Zappalà. Gluon condensation and deconfinement critical density in nuclear matter. *Nucl. Phys. A*, 743:3–12, 2004.

[78] M. Baldo, G.F. Burgio, et al. Astrophysical constraints on the confining models: The field correlator method. *Phys. Rev. D 78 063009*, 2008.

[79] M. Baldo, G.F. Burgio, P. Castorina, S. Plumari, and D. Zappala. Astrophysical constraints on the confining models: The Field Correlator Method. *Phys.Rev.*, D78:063009, 2008.

[80] Isaac Vidana. Hyperons in Neutron Stars. 2015.